

GAUSSIAN BEAM PROPAGATION IN TURBULENT SUPERSONIC FLOWS

Donald R. Emmons Jr.
B.S., Indiana State University, 1972
M.A., Indiana State University, 1975

A dissertation submitted to the faculty
of the Oregon Graduate Center
in partial fulfillment of the
requirements for the degree
Doctor of Philosophy
in
Applied Physics

September 1986

The dissertation "Gaussian Beam Propagation in Turbulent Supersonic Flows" by Donald R. Emmons Jr. has been examined and approved by the following examination committee:

Richard A. Elliott, Thesis Advisor
and Examination Committee Chairman
Professor

J. Fred Holmes
Professor

Rao Gudimetla
Assistant Research Professor

M. A. K. Khalil
Professor

ACKNOWLEDGMENTS

For Vilgae, Claudia, Richard and Gertrude.

My thanks go to Prof. Richard Elliott of the Oregon Graduate Center and Dr. Robert McKenzie of NASA Ames Research Center for their help and support.

The work described in this dissertation was made possible by a three-year grant funded by the National Aeronautics and Space Administration.

I would like to express my deep gratitude to Mr. Richard Exberger, Dr. Kenneth Gross, Mr. Steve Robinson, Mr. Daryl Monson, Capt. David Dimiduk, and Dr. Rao Gudimetla for the considerable contributions that they made to this work. Thank you also for helping to make a very difficult situation tolerable.

TABLE OF CONTENTS

ACKNOWLEDGMENTS	iii
LIST OF FIGURES	vii
ABSTRACT	x
I. AN INTRODUCTION TO THE PROJECT	1
A. Introduction	1
B. Active Methods	2
C. Passive Methods	4
D. Atmospheric Techniques	6
E. OGC/NASA Joint Research Project.	7
II. WIND TUNNEL CONSIDERATIONS	10
III. THE THEORY OF GAUSSIAN BEAM PROPAGATION IN A TURBULENT SUPERSONIC FLOW	16
A. Introduction	16
B. The Extended Huygens-Fresnel Theory	18
C. Calculation of the Mean Output Irradiance	22
D. Mean Output Irradiance with Center Turbulence ..	36
E. Intensity Covariance Function	38
F. Equal Path Length Interferometer	43
G. Conclusions	47
IV. PITOT TUBE/HOT WIRE ANEMOMETRY OF THE LUDWIEG TUBE FLOW	50
A. Introduction	50

	B. Analysis and Results of the Measurement of the Ludwig Tube Flow Using a Pitot Tube Anemometer	55
	C. Analysis and Results of the Measurement of the Ludwig Tube Flow Using a Hot Wire Anemometer	66
V.	THE DESIGN OF A SINGLE BEAM EXPERIMENT TO TEST THE APPLICABILITY OF THE EXTENDED HUYGENS-FRESNEL THEORY TO THE CASE OF SUPERSONIC FLOW	82
	A. Introduction	82
	B. The Calculation of the Refractive Index Spectrum and the Structure "Constant" from the Hot Wire/ Pitot Tube Measurements	85
	C. A Theoretical Model of the Single Beam Experiment using the Extended Huygens-Fresnel Theory	101
VI.	THE RESULTS OF THE SINGLE BEAM EXPERIMENT	115
	A. Introduction	115
	B. Vibrational Noise Evaluation	119
	C. Correction of the Data for the Effects Introduced by the Windows in the Flow Nozzle ...	123
	D. Experimental Results	136
VII.	THE DESIGN OF A TWO BEAM EXPERIMENT	139
	A. Introduction	139

B.	The Application Of Yura's Formalism to the Case of Crossed Beam Correlation	144
C.	The Application of Log Amplitude Techniques to the Problem of Remote Sensing in a Wind Tunnel	155
D.	Conclusions	160
VIII.	THE RESULTS OF THE CROSSED BEAM EXPERIMENT	162
A.	A Detailed Description of the Experiment	162
B.	The Experimental Results	168
IX.	CONCLUSIONS AND SUGGESTIONS FOR FURTHER WORK	172
A.	Conclusions	172
B.	Suggestions for Further Work	174
	REFERENCES	176
	VITAE	183

LIST OF FIGURES

FIGURE

1. The NASA Ludwig Tube Flow Facility	12
2. The Step Response of the Wind Tunnel	15
3. Pitot Tube Assembly	52
4. Hot Wire Probe Assembly	54
5. Block Diagram of the Pitot Tube/Hot Wire Measurements .	56
6. Access Port Detail	57
7. Shadowgraphs of the Flow Around the Mounting Hardware .	58
8. Parameters of Interest in the Pitot Tube Experiment ...	61
9. Mach Number vs. y/H	64
10. Normalized Velocity vs. y/H	65
11. Normalized Temperature vs. y/H	67
12. Normalized Density vs. y/H	68
13. Comparison of Hot Wire and Pitot Tube Signals	74
14. Typical Hot Wire Data	75
15. Hot Wire Calibration Curve	77
16. RMS Mass Flow Fluctuations vs. y/δ	79
17. RMS Density Fluctuations vs. y/δ	80
18. Comparison of Hot Wire Data with LIF Data	81
19. The Effect of Beam Size on the Far Field Laser Spot ...	84
20. Hot Wire Data Reduction	87

21. Typical Power Spectrum of the Hot Wire Data	89
22. Comparison of Experimental and Theoretical Spectra	92
23. C_n^2 vs. y/δ	95
24. Power Spectra at $y/\delta = 0.42, 1.00$ and C.L.	96
25. Mean Velocity vs. y/δ	97
26. Quantitative Spectral Plots	100
27. Block Diagram of the Single Beam Experiment	102
28. Second Term Approximation	106
29. Analytical Fit to $C_n^2(y/\delta)$	108
30. C_n^2 as a Function of Position	109
31. $\langle P \rangle / P$ as a Function of Z	113
32. Engineering Details of the Single Beam Experiment	116
33. Typical Transient Digitizer Output	120
34. Beam Path for the Vibration Test	121
35. Results of the Vibration Test	122
36. Window/Beam Geometry	125
37. Window/Beam Refractive Geometry	129
38. A Deflected Beam on the Aperture	131
39. The Results of the Single Beam Experiment	137
40. Crossed Beam Correlation Geometry	140
41. Multiple Eddy Interaction	142
42. Proposed Crossed Beam Experiment	146
43. Exponential Approximation to $B_n(r)$	152
44. Beam Crossing Geometry	153

45. Beam Crossing Geometry used by Wang et al	158
46. The Layout of the Crossed Beam Experiment	163
47. Detector Analysis Logic	165
48. X Axis Cross Correlation Coefficient vs. y/δ	169

ABSTRACT

Gaussian Beam Propagation in Turbulent Supersonic Flow

Donald R. Emmons Jr., Ph.D.
Oregon Graduate Center, 1986

Supervising Professor: Richard A. Elliott

Due to advances in experimental techniques and numerical air flow modeling, there has been a need for improved instruments capable of measuring turbulence parameters in compressible (supersonic) gas flows. A great deal of work has been done in recent years in applying various optical methods as the basis for remote sensing instruments capable of measuring these parameters to a high degree of accuracy. While both active and passive techniques have been proposed and developed, passive techniques tend to require only low power light sources with resultant advantages in expense, complexity and ease of operation.

The work described in this dissertation involves the application of theoretical and experimental methods first developed in the field of atmospheric optics to the problem of passive remote sensing of fluid density in the supersonic turbulent field produced in a Mach 1.8 wind tunnel. A supersonic wind tunnel at NASA Ames Research Center was first characterized using standard intrusive measurement techniques and then used to test the validity of a theory based on the extended Huygens-Fresnel (EHF) principle which has been useful in long path atmospheric propagation. Experimental results demonstrated that the

extended Huygens-Fresnel-based theory may be used to model the effects of supersonic turbulence on laser radiation to a high level of accuracy. This result suggested two optical schemes for remote turbulence measurement which were explored in the wind tunnel environment with the basic instrumentation consisting of a low power (1 mW) He-Ne laser capable of providing a diffraction limited, TEM_{00} beam and a simple optical system capable of focusing the beam to several waist sizes.

CHAPTER I

AN INTRODUCTION TO THE PROJECT

A. Introduction

The past few years have seen a rapid expansion in the field of supersonic fluid dynamics.^{1,2} As researchers in this area have refined their craft, an important need for improved laboratory instrumentation has become apparent.² This need has spawned a wide variety of work which includes the activities described in this dissertation.

Measurement of turbulence parameters in a compressible (supersonic) gas flow presents a difficult problem for the experimentalist. When a physical transducer is placed in such a flow, the compressible nature of the gas, evident at flow rates in excess of Mach 1, causes a shock wave to form around the up wind portion of a probe exposed to the flow. Since the traditional methods of flow measurement have been intrusive in nature, requiring transducers protruding into the flow, their disadvantages have severely limited the collection of data on the nature of transonic and supersonic air flows in either laboratory (wind tunnel) or real-world environments.³

A very attractive alternative to these intrusive methods would be to use electromagnetic radiation (usually but not always in the form of

light) to remotely probe the flow parameters of interest without the need to place any physical transducer in the flow. Much attention has been given to the development of this nonintrusive alternative in recent years with the resulting implementation of several optical techniques for the measurement of relevant flow parameters.²

These optical methods typically fall into one of two overall categories depending on the basis of the technique.

B. Active Methods

These methods involve the absorption or scattering of radiation by either the constituent molecules of the flow or by seed molecules or particles added to the flow. These seed quantities are needed to modify the spectroscopic properties of the gas (working fluid) or to provide specific scattering sites in the flow.

Several active techniques have been proposed and are either implemented or in an interim stage of development. Laser Doppler Velocimetry (LDV) is probably the most widely used of the active methods to date.^{1,4,5} LDV requires the seeding of the working fluid with small particles which serve as scattering sites in the flow. Two laser beams are crossed in the flow at the point of interest forming an interference pattern which is then scattered out of the flow by the seed particles. The fringes in the scattered interference pattern will

appear to shift in space at a rate proportional to the velocity of the particles doing the scattering thus providing a measure of the local flow velocity (assuming the scattering particles to be small enough to respond to localized changes in the flow velocity in a manner similar to that of the molecules in the working fluid).^{4,5} The major disadvantage of LDV stems from the need to seed the flow with particulate material. This material has a sandblasting effect on the walls of a wind tunnel and on any intrusive transducer that is placed in the flow. It also makes it impossible to measure the flow velocity around any discontinuities in the flow due to the fact that the particles will not track a sharp change in contour. LDV, in addition, will provide no information regarding density or temperature, both parameters of interest.^{4,5}

Another active technique of recent development is that of Laser Induced Fluorescence (LIF).^{6,7} This method may also involve the seeding of the working fluid, but, in this case, a seed gas is used having appropriate spectral characteristics for the absorption of laser light of a convenient wavelength. The seed gas, or working fluid directly, is bombarded with laser radiation tuned to an appropriate absorption band and the broad band fluorescence radiation, emitted as the stimulated molecules relax, is then collected. The total fluorescence power will be proportional to the density of the working fluid (indirectly through the seed gas) allowing a localized measurement to be made. Researchers at NASA's Ames Research Center have recently used two stimulating beams slightly detuned to probe the upper energy level electron population of

the seed gas, thus measuring density and temperature simultaneously. These measurements will allow the calculation of a local pressure quantity and represents a major breakthrough in the remote sensing of supersonic flows.⁸ The major drawback to LIF at present is again the need for a seed gas. This makes the process difficult to apply to a large scale wind tunnel or real world environment. Work is presently underway to correct this problem.

Several other techniques of actively sensing flow parameters are also under present consideration. They include Coherent Anti-Stokes Raman Scattering (CARS), a nonlinear scattering effect of particular usefulness in flame measurements, and other nonlinear scattering and wavelength shifting effects.^{9,10}

C. Passive Methods

The term "passive methods" describes those remote sensing techniques which do not involve the absorption and re-emission of radiation by either the working fluid or a seed material. Most passive methods involve the sensing of the phase perturbations of the radiation propagating in a supersonic turbulent field. As a result, these techniques, including those described in this dissertation, are typically much less complicated in both implementation and design than the active techniques. Since the optical beam is usually viewed directly, a high signal-to-noise ratio (SNR) is relatively easy to realize. The two major

limitations of passive remote sensing are the requirement for density perturbations to be present in the flow to distort the phase of the optical wave and the fact that most passive methods are sensitive only to the statistical moments of the density perturbations. Other drawbacks, such as lack of spatial resolution, appear to be tractable to at least some extent.

Probably the two most common passive techniques are shadowgraph and schlieren photography.¹¹⁻¹³ Both methods record the far field interference pattern produced by the turbulence induced phase perturbations of a plane wave (collimated beam).¹¹ While rarely used in a quantitative manner, these methods provide two very easy and convenient ways in which to visualize the path integrated density perturbations in a compressible flow.¹⁴ In the case of a two-dimensional flow, these methods are quite sensitive to shock wave effects and are quite useful for displaying the presence of these effects. Recent work has demonstrated a quantitative schlieren technique very similar in philosophy to the project described here but limited, at present, to two-dimensional flows.¹⁵ Crossed beam correlated schlieren measurements have also proved useful in flame measurements for providing limited spatial resolution. These techniques are limited, however, by a very simple theoretical approach to beam turbulence interaction.^{16,17} Multiple beam and wavelength holography have also been applied with good results in several two-dimensional flow

applications. As with most passive methods, holography suffers from a lack of spatial resolution which limits its application in the case of three-dimensional flow.¹⁸

Lastly, under the heading of passive methods are those coming from techniques and theory first developed in the field of atmospheric optics, which includes the work described in this dissertation.

D. Atmospheric Techniques.

The past decade has seen a great deal of research carried out in the field of laser beam propagation through the turbulent atmosphere in the context of communications and military applications.^{19,20} These endeavors have included methods for remote wind sensing, measurements of atmospheric density as well as particulate detection.²¹⁻²³ Statistical models have been developed which have been demonstrated to be capable of describing the effect of random refractive index fluctuations on laser radiation to a high level of accuracy.^{19,20} The overall nature of the atmospheric problem is very similar to that of describing the effects of turbulence in a compressible wind tunnel air flow and it is therefore very tempting to apply atmospheric techniques (particularly the theory) to the case of supersonic flow.

The theoretical treatment of the effects of random density (index of refraction) fluctuations on propagating E.M. radiation involves a perturbational solution of the wave equation and requires some rather complicated calculations which can be accomplished only by restricting

the degrees of freedom of both the turbulent field and the radiation (see chapter IV).²⁰ These restrictions can be quite severe in nature and are capable of limiting the range of validity of a resulting model. Since a few of these atmospheric restrictions are not strictly valid in the case of compressible flow, there is no reason to suspect, a priori, that a model based on such a theory would be capable of describing the effects of a flow in, for example, a Mach 2 wind tunnel. However, the absolute limits on the validity of the atmospheric theory have yet to be explored in a complete and systematic fashion and it has not been clear in the past that an application, such as the one described here, would be without merit.

E. OGC/NASA Joint Reasearch Project

With this in mind, it was proposed in 1980 that a study be undertaken to determine the feasibility of applying the theoretical approach and experimental techniques of optical propagation in the atmosphere to attempt to model the effects of the turbulent field in a supersonic gas flow on Gaussian laser radiation. Any techniques capable of providing sufficient spatial resolution for local measurements and which could be inverted and thus form the basis of a remote sensing scheme for density or temperature fluctuations would be of particular interest. This would be a joint study undertaken by the Oregon Graduate Center and NASA Ames Research Center in Mountain View, California, allowing access to a laboratory scale supersonic wind tunnel with

appropriate flow characteristics and provisions for beam optical measurements.

Such a three-year study was funded in 1981 having the following goals:

1. Using established intrusive measurement techniques (hot wire/pitot tube anemometry), completely characterize the flow in a laboratory scale, supersonic wind tunnel. The ultimate goal of this characterization will be a time resolved measurement of the fluctuating density perturbations so that correlation relationships and frequency spectra may be obtained.
2. Using the results of 1. above, model the effect of the turbulence in the compressible flow on a propagating, TEM_{00} laser beam using the theoretical techniques of optical propagation in the atmosphere (extended Huygens-Fresnel theory).
3. Design and carry out a series of experiments capable of measuring the perturbation of the beam parameters due to the turbulence and compare these measured effects to those predicted by the atmospheric theory based model. Such a comparison will test the validity of the atmospheric theory in describing the case of compressible flow.

4. If possible, model the case of two laser beams simultaneously propagating through the turbulent field and crossing in various geometries. From this, determine the feasibility of using multiple beams to remotely sense local density fluctuations.
5. Design and carry out a series of experiments which will determine the validity of the model described in 4. above.
6. Draw general conclusions based on the results of the preceding activities regarding the feasibility and desirability of using these techniques to remotely measure turbulence parameters in a compressible gas flow.

The undertakings described above were completed in a four-year time frame extending from 1981 through 1985 and form the basis of this Ph.D. dissertation. Of this time, approximately 2.5 years were spent in residence at NASA Ames Research Center. The project was funded by NASA under the auspices of its Graduate Student Research Program.

CHAPTER II

WIND TUNNEL CONSIDERATIONS

As noted in the previous chapter, fluid flowing at velocities in excess of Mach 1 exhibits compressibility effects. The fact that the fluid may be compressed allows the formation of local perturbations in the density, which greatly complicates the description of interactions between the working fluid and any physical constraints placed on the flow (such as wind tunnel walls, measurement transducers, models, etc.). Of particular interest to researchers in the field of experimental fluid dynamics is the behavior of the flow at path discontinuities since the compressible nature of the working fluid can give rise to very strong localized density gradients known as shock waves. The average citizen in the 1950's and early 1960's became quite familiar with the "sonic boom" produced by supersonic aircraft of the era due to the shock waves induced by relative discontinuities in the shape of the airframe.

In general, any time a discontinuity is placed in the flow a shock wave of some type will be produced. This state of affairs presents the experimentalist with the classic problem of the measuring device so perturbing the system that the measurement may be rendered meaningless. It also presents problems in designing laboratory scale experiments involving the use of flow nozzles and wind tunnels. While many areas of

compressible flow phenomena are of current interest, an area of particular concern for the experimentalist is turbulence in supersonic flow produced by both viscous drag (wall type effects) and shock wave production (flow separation). It is necessary, therefore, to develop wind tunnels and flow nozzles capable of reproducing these effects on a laboratory scale without the introduction of additional artifacts as a result of the reduced scale of the flow. While this dramatically complicates the design process and significantly increases the cost of such a facility, attention to such details is an absolute necessity in order to assure a sufficiently simple flow pattern capable of tractable analysis.

The author was fortunate to be allowed almost unlimited access to a well-designed tunnel at NASA Ames Research Center, Moffett Field, Ca. A block diagram of the entire facility is given in Figure 1. The heart of the facility is a rectangular cross section flow nozzle capable of producing nitrogen flow rates in excess of Mach 1.7 at a load pressure of 100 psi. The nozzle is operated in a Ludwig tube (shock tube) configuration and the overall wind tunnel consists of four major components (see figure 1). The working fluid reservoir consists of a thick-walled pipe approximately 15 ft. in length with a cross sectional diameter of approximately 6 in. The working fluid undergoes an adiabatic expansion into a large volume (4 ft. diameter by 10 ft. in length) holding tank which is evacuated by a vacuum pump to a pre-fire pressure of about 10 mTorr. The low pressure holding tank is separated from the flow nozzle by a high speed, helium actuated valve capable of opening so

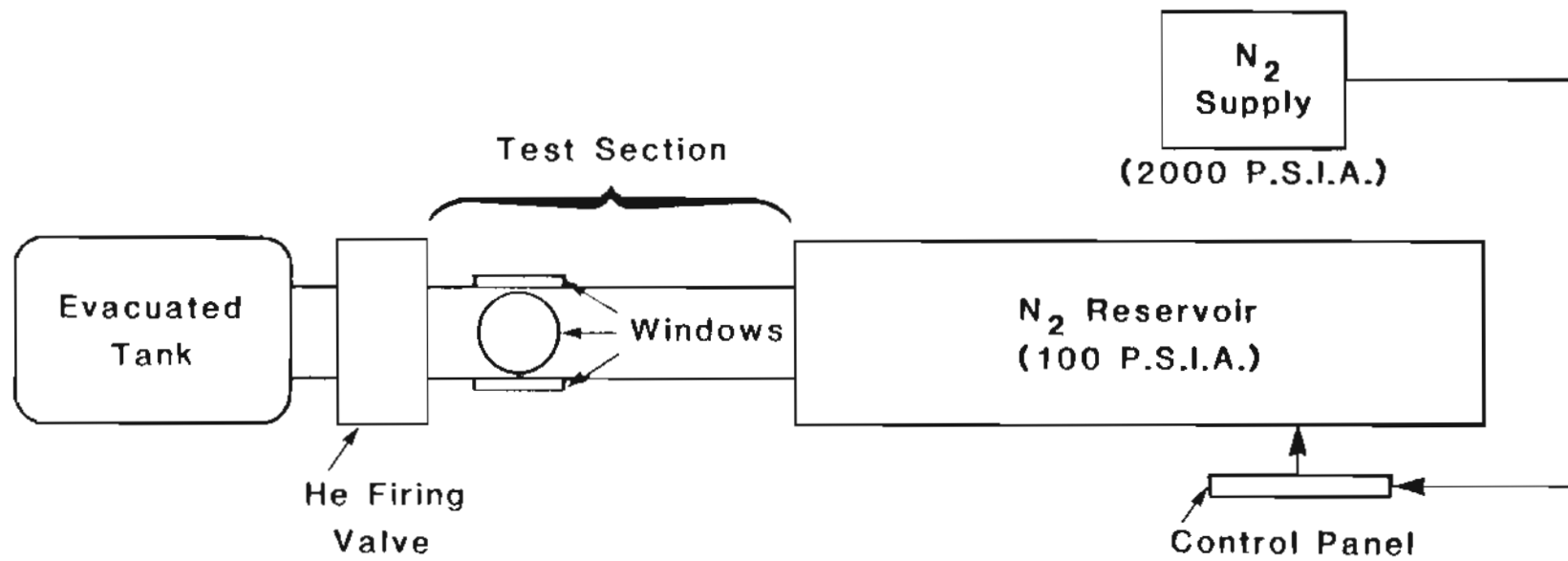


FIGURE 1. The NASA Ludwig Tube Flow Facility

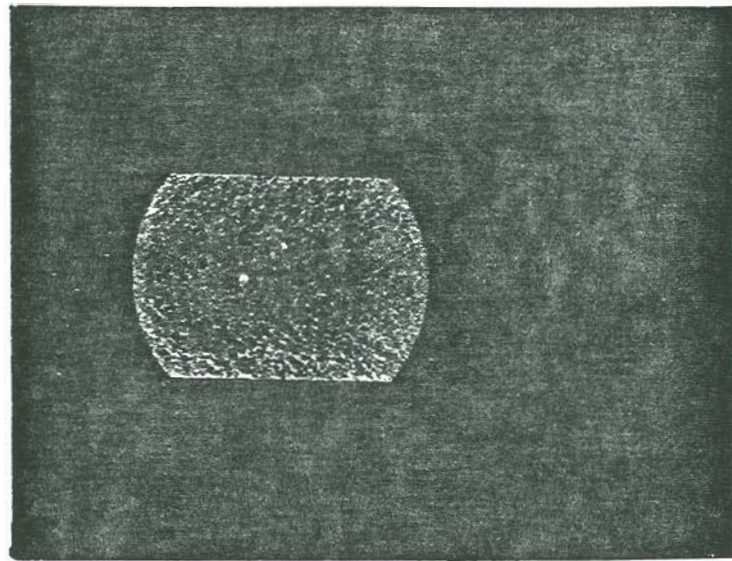
rapidly that the removal of the valve constraint may be considered to be instantaneous and thus the change in the boundary condition may be approximated by a step function.

Three 2 in. diameter fused silica windows capable of withstanding high pressure have been mounted in the flow nozzle to form an optically accessible test section (see figure 1). The material of these windows transmits radiation into the near ultra-violet and is thus quite adequate for this work which was done in the visible spectrum. Several pressure cells have been mounted in the test section and at various upstream locations to allow the monitoring of at least the low frequency flow parameters. It is possible to introduce intrusive measurement probes through any window port and, as part of this work, the author modified the tube to allow access to the flow downstream of the test section and thus reduce flow perturbation due to the shock waves produced around probe mounting hardware. As previously noted, the reservoir tube is loaded with nitrogen gas to an initial fill pressure of 100 psi (with the tube at approximate thermal equilibrium) from external high pressure tanks. One complete operational cycle consisting of two runs (N_2 fill, firing, N_2 fill, firing and pump down of the holding tank) requires 25-35 minutes.

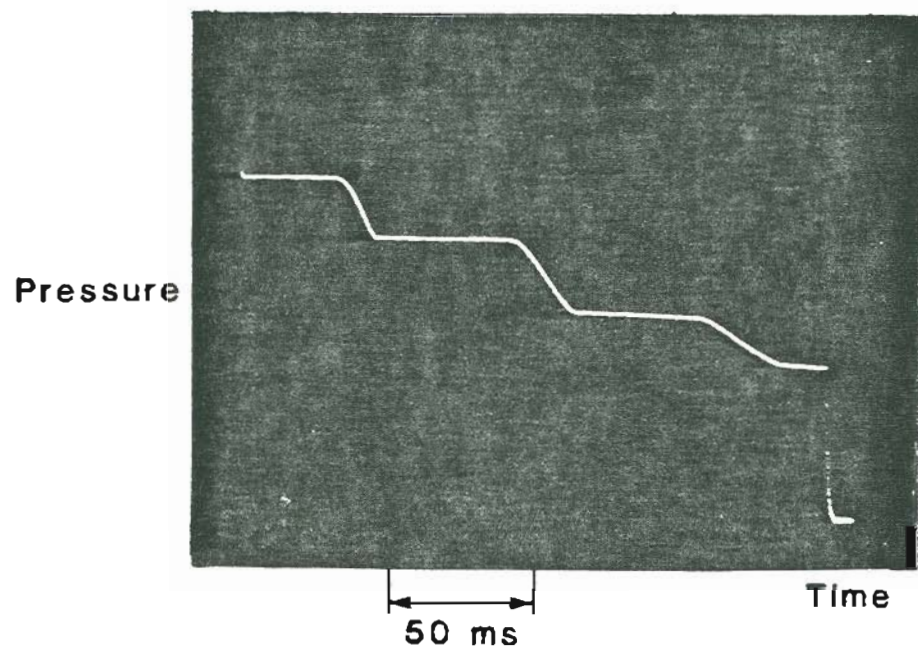
When the firing valve is suddenly opened, the pressurized nitrogen working fluid undergoes a free expansion into the evacuated tank. The opening of the firing valve also causes an expansion wave to propagate upstream at the local speed of sound. Since the gas ahead of the expansion wave in the reservoir does not know the firing valve has been

opened (acoustic information cannot be transmitted in a medium at a rate in excess of the speed of sound), conditions in the test section remain fairly constant until the wave has traversed the entire length of the reservoir and returned. The facility thus has a pressure-versus-time response which takes the form of a staircase function.

Figure 2 is a composite showing the stepwise nature of P vs. t and a shadowgraph visualization of the turbulent field in the test section as viewed across the flow through the optical access windows.



A. Shadowgraph of Turbulent Flow



B. Step Response of the Facility

FIGURE 2. The Step Response of the Wind Tunnel

CHAPTER III

THE THEORY OF GAUSSIAN BEAM PROPAGATION IN A TURBULENT SUPERSONIC FLOW

A. Introduction

Over the past two decades, a statistical theory has been developed to describe the effects of a turbulent medium on propagating electromagnetic radiation.^{24,25} The practical statement of this theory, known as the extended Huygens-Fresnel formulation, has provided the basis for the experimental use of laser beams as remote sensing devices.²⁶⁻²⁸ By measurement of the statistical perturbations induced on a Gaussian beam it is possible to determine various scale sizes characterizing the turbulent flow, flow rate and the strength of the turbulent field, thus characterizing the medium.

Several remote sensing applications have been modeled in detail for values of turbulence parameters typical of the atmosphere.^{21-23,29,30} Atmospheric turbulence is, in general, of weak to moderate strength (for short path lengths) with turbulent field scale sizes in the range of 0.1 to 100 cm.³¹ These applications have assumed the optical propagation distance to be on the order of 10 to 1000 m with uniform or slowly varying turbulence strength along the path and that the source and receiver are both immersed in the turbulent field.³¹

The author now describes the application of the extended Huygens-Fresnel (EHF) theory to the problem of remotely sensing turbulence parameters in a supersonic bounded (physically enclosed) flow. This particular application is specifically concerned with modeling the effects of the turbulent field produced in the NASA Ludwig tube facility described in chapter II but will also be examined to determine the usefulness of the EHF theory in measuring other common flow situations of general interest. The wind tunnel environment is different from the problem of atmospheric propagation in several important ways.

As noted in chapter II, the Ludwig tube is rectangular in cross section with the approximate dimensions of 6 x 4 cm. Nitrogen flowing through this nozzle will form turbulent boundary layers along the nozzle walls due to viscous drag and will, in general, be quite strong compared to atmospheric turbulence even over relatively short optical path lengths. The turbulence parameters will decrease fairly quickly in magnitude as the distance from the wall increases leaving a near laminar flow region near the center of the test section and thus the level of turbulence varies rapidly over path length unlike the atmosphere. Since the beam source and receiver must be outside the turbulent field, beam egress effects (due primarily to the windows) must be considered. Also the physical dimensions of the Ludwig tube restricts the turbulent scale sizes and optical path lengths to fractions of a meter. All of these features represent significant departures from the work of previous authors.

This work will present first an overview of the extended Huygens-Fresnel formalism and then proceed to apply this model to the case of an empty Ludwig tube (turbulence only on the walls) and also the case of a "packet" of turbulence in the center of the nozzle as well as on the walls. Analytic expressions for the mean intensity (irradiance), intensity covariance and mean output intensity for an equal arm interferometer will be determined by employing suitable approximations. Numerical results will be presented in later chapters.

B. The Extended Huygens-Fresnel Theory

The Rayleigh-Sommerfeld formulation of the Huygens-Fresnel principle has long been a powerful tool in the field of Fourier optics.³² In physical terms, the principle states that the electric field at any point in a receiver plane will consist of the superposition of spherical wave fields originating at each point in a source plane. These spherical waves are weighted appropriately to form the spatial frequency spectrum of the source disturbance.

The field quantity (u) representing an optical wave must satisfy the scalar wave equation.

$$\nabla^2 u(\vec{\rho}, t) - (1/c^2) \cdot (\partial^2 / \partial t^2) [u(\vec{\rho}, t)] = 0 \quad (1)$$

The field strength u may be written in terms of a complex notation as:

$$u(\vec{\rho}, t) = \text{Re}[u(\vec{\rho})e^{i\omega t}] \quad (2)$$

where $u(\vec{\rho})$ represents the complex field amplitude. Substituting Eq. (2) into (1) yields an equation independent of time.

$$(\nabla^2 + k^2)u(\vec{\rho}) = 0 \quad (3)$$

where k is the magnitude of the wave vector and is given by $(2\pi/\lambda)$. Eq. (3) is the well-known Helmholtz equation which may be solved by means of Green's theorem and the application of the appropriate Green's function. The solution of Eq. (3) will be determined by the superposition integral:³²

$$\int_{\text{(input aperture)}} d^2\vec{r} u_A(\vec{r}) G_S(\vec{r}; \vec{\rho}) \cos\{\hat{n}, |\vec{r} - \vec{\rho}|\} \quad (4)$$

where:

$$G_S(\vec{r}; \vec{\rho}) = e^{ik|\vec{r} - \vec{\rho}|} \cdot |\vec{r} - \vec{\rho}|^{-1} \quad (5)$$

The quantity u_A is the field at the transverse distance r in the source plane and $\cos[n, |r - \rho|]$ is the so called "obliquity factor."

If u represents a finite beam which has only a small transverse extent and if u varies slowly over a wavelength distance, then the obliquity factor reduces to $-i/\lambda$ and :³²

$$u(\rho) = -(ik/2\pi) \int d^2\vec{r} G_S(\vec{r}:\vec{\rho}) u_A(\vec{r}) \quad (6)$$

Lutomirski and Yura have shown that Eq. (4) may be extended to include the case of radiation propagating in a turbulent medium by adding a random complex phase term to the spherical wave Green's function.^{26,33}

$$G_S(\vec{r}:\vec{\rho}) = \text{Exp}\{ik|\vec{r} - \vec{\rho}| + \Psi(\vec{r}, \vec{\rho})\} / |\vec{r} - \vec{\rho}| \quad (7)$$

$\Psi(r, \rho)$ describes the effects of small random fluctuations in the refractive index on the propagating spherical wave. If the index of refraction of the turbulent medium is written in the form:

$$n(\vec{r}) = 1 + n_1(\vec{r}) \quad (8)$$

(where $|n_1| \ll 1$ and is a random variable), then Ψ is the solution of:

$$\nabla^2 \Psi + (\nabla \Psi)^2 + k^2 [1 + n_1(\vec{r})^2] \Psi = 0 \quad (9)$$

Ψ may be expanded in a power series as a function of n_1 and, to second order, may be written in the form:

$$\Psi = \Psi_1 + \Psi_2 \quad (10)$$

where $\Psi_1 \sim n_1$ and $\Psi_2 \sim n_1^2$. Hence the field strength (and consequently, all statistical moments of the field) may be written in terms of Eq. (6).

Note, however, that in this development the determinism of the various quantities and mathematical functions has been lost due to the need to model the turbulence as a randomly occurring statistical phenomenon in order to pose a tractable problem. In the application of the Huygens-Fresnel principle in Fourier optics, the quantities $u(\rho)$ and $u(\rho)u^*(\rho)$ have rather straightforward deterministic interpretations but when the theory is extended to include a randomly turbulent medium, only the statistical moments (brackets $\langle \rangle$ denote ensemble averaging) of the field quantities $\langle u(\rho) \rangle$ or $\langle u(\rho)u^*(\rho) \rangle$ have meaning since they alone are observable.

C. Calculation of the Mean Output Irradiance (Intensity)

Since the output field quantities are specified by the extended Huygens-Fresnel theory, the mean irradiance of a Gaussian laser beam passing through the Ludwig tube and observed in a specific far field plane may be calculated from the second moment of the field strength: $u(\vec{\rho})$.

$$M_2(\vec{\rho}_1, \vec{\rho}_2) \equiv \langle u(\vec{\rho}_1) u^*(\vec{\rho}_2) \rangle \quad (11)$$

$$\langle I(\vec{\rho}) \rangle = \langle u(\vec{\rho}) u^*(\vec{\rho}) \rangle \quad (12)$$

Using equation (6):

$$\langle I(\vec{\rho}) \rangle = (k^2/4\pi^2) \int d^2\vec{r}_1 \int d^2\vec{r}_2 u_A(\vec{r}_1) u_A^*(\vec{r}_2) \langle G_S(\vec{r}_1; \vec{\rho}) G_S^*(\vec{r}_2, \vec{\rho}) \rangle \quad (13)$$

Using equation (7):

$$\begin{aligned} \langle G_S(\vec{r}_1, \vec{\rho}) G_S^*(\vec{r}_2, \vec{\rho}) \rangle &= \text{Exp}\{ik[|\vec{r}_1 - \vec{\rho}| - |\vec{r}_2 - \vec{\rho}|]\} \cdot |\vec{r}_1 - \vec{\rho}|^{-1} \\ &\quad \cdot |\vec{r}_2 - \vec{\rho}|^{-1} \cdot \langle \text{Exp}\{\psi(\vec{r}_1, \vec{\rho}) + \psi^*(\vec{r}_2, \vec{\rho})\} \rangle \end{aligned} \quad (14)$$

Employing the paraxial approximation appropriate for the case of a finite beam, Eq. (14) becomes:

$$\begin{aligned} \langle G_S(\vec{r}_1, \vec{\rho}) G_S^*(\vec{r}_2, \vec{\rho}) \rangle &= \text{Exp}\{(ik/2z)[\vec{r}_{12} - \vec{r}_{22} - 2\vec{\rho} \cdot (\vec{r}_1 - \vec{r}_2)]\} \\ &\cdot F(\vec{r}_1, \vec{r}_2; \vec{\rho})/z^2 \end{aligned} \quad (15)$$

where r_i and ρ are vectors transverse to the propagation axis and lie in the source ($z = 0$) and receiver (z) planes respectively. Also:

$$F(\vec{r}_1, \vec{r}_2; \vec{\rho}) \equiv \langle \text{Exp}\{\psi(\vec{r}_1, \vec{\rho}) + \psi^*(\vec{r}_2, \vec{\rho})\} \rangle \quad (16)$$

Yura has shown:³³

$$F(\vec{r}_1, \vec{r}_2; \vec{\rho}) = \text{Exp}\{\langle \psi_1(\vec{r}_1, \vec{\rho}) \psi_1^*(\vec{r}_2, \vec{\rho}) \rangle - \langle |\psi_1|^2 \rangle\} \quad (17)$$

where ψ_1 is the first order solution of Eq. (9) and is given by:

$$\begin{aligned} \psi_1(\vec{r}, \vec{\rho}) &= (k^2 z / 2\pi) \text{Exp}\{-[ikz + (ik/2z)(\vec{r} - \vec{\rho})^2]\} \cdot \int d^3x_1 n_1(\vec{x}_1) \\ &\cdot \text{Exp}\{ik(z - z_1) + (ik/2[z - z_1])(\vec{\rho}_1 - \vec{r})^2\} \\ &\cdot [\text{Exp}\{ikz + (ik/2z_1)(\vec{\rho}_1 - \vec{\rho})^2\}] / [z_1(z - z_1)] \end{aligned} \quad (18)$$

in the paraxial approximation. The vector \mathbf{x}_1 is specified by:

$$\vec{\mathbf{x}}_1 = (\vec{\rho}_1, z_1) \quad (19)$$

Therefore:

$$\begin{aligned} \langle \psi_1(\vec{\mathbf{r}}_1, \vec{\mathbf{p}}) \psi_1^*(\vec{\mathbf{r}}_2, \vec{\mathbf{p}}) \rangle &= (z^2 k^4 / 4\pi) \text{Exp}\{- (ik/2z) [(\vec{\mathbf{r}}_1 - \vec{\mathbf{p}})^2 - (\vec{\mathbf{r}}_2 - \vec{\mathbf{p}})^2]\} \\ &\cdot \int d^3\vec{\mathbf{x}}_1 \int d^3\vec{\mathbf{x}}_2 \langle n_1(\vec{\mathbf{x}}_1) n_1(\vec{\mathbf{x}}_2) \rangle / [z_1 z_2 (z - z_1)(z - z_2)] \\ &\cdot \text{Exp}\{ik[f_1 + f_2 + f_3 + f_4]\} \end{aligned} \quad (20a)$$

where:

$$\begin{aligned} f_1 &= (\vec{\rho}_1 - \vec{\mathbf{r}}_1)^2 / (2z_1) \\ f_2 &= (\vec{\rho}_1 - \vec{\mathbf{p}})^2 / [2(z - z_1)] \\ f_3 &= -(\vec{\rho}_2 - \vec{\mathbf{r}}_2)^2 / (2z_2) \\ f_4 &= -(\vec{\rho}_2 - \vec{\mathbf{p}})^2 / [2(z - z_1)] \end{aligned} \quad (20b)$$

By definition, the refractive index covariance function is given by:

$$B_n(\vec{x}_1, \vec{x}_2) = \langle n_1(\vec{x}_1) n_1(\vec{x}_2) \rangle \quad (21)$$

The strength of the turbulence will be a function of propagation distance (z) inside the nozzle. Since the thickness of the turbulent layer on each wall must be on the order of the outer scale size (L_0), the theory of a locally homogeneous field with a slowly varying mean, as developed by Tatarskii is not strictly valid.²⁵ Its use in this calculation, however, will serve a two-fold purpose the first of which will be to provide a "zero'th" order approximation of the complete model to allow various experimental methods to be compared and the second is to test the limits on the validity of the atmospheric theory in other situations. After Tatarskii, the refractive index covariance function may be written in terms of its two-dimensional Fourier transform:

$$B_n(\vec{x}_1, \vec{x}_2) = \int d^2\vec{k} F_n(\vec{k}, [z_1 - z_2], [z_1 + z_2]/2) \cdot \text{Exp} \{-i\vec{k} \cdot (\vec{\rho}_1 - \vec{\rho}_2)\} \quad (22)$$

Therefore:

$$\langle \psi_1(\vec{r}_1, \vec{\rho}) \psi_1^*(\vec{r}_2, \vec{\rho}) \rangle = (z^2 k^4 / 4\pi) \text{Exp}\{(-ik/2z)[(\vec{r}_1 - \vec{\rho})^2 - (\vec{r}_2 - \vec{\rho})^2]\} \cdot \int d^2\vec{k} Q(\vec{k}) \quad (23)$$

where:

$$\begin{aligned}
 Q(\vec{k}) = & \int d^3\vec{x}_1 \int d^3\vec{x}_2 F_n(\vec{k}, [z_1 - z_2], [z_1 + z_2]/2) / [z_1 z_2 (z - z_1)(z - z_2)] \\
 & \cdot \text{Exp}\{i(k/2z_1)(\vec{\rho}_1 - \vec{r}_1)^2 + [ik/(2[z - z_1])](\vec{\rho}_1 - \vec{p})^2 \\
 & - i(k/2z_2)(\vec{\rho}_2 - \vec{r}_2) - [ik/(2[z - z_2])](\vec{\rho}_2 - \vec{p})^2 \\
 & - ik \cdot (\vec{\rho}_1 - \vec{\rho}_2)\} \quad (24)
 \end{aligned}$$

Using the expression for the volume element in cylindrical coordinates:

$$|d^3\vec{x}| = \rho d\rho dz d\theta \quad (25)$$

Eq. (24) may be written as:

$$\begin{aligned}
Q(\kappa) = & 4\pi \text{Exp}\{(ik/2)[r_1^2/z_1 - r_2^2/z_2]\} \\
& \cdot \text{Exp}\{(ik/2)\{1/(z - z_1) - 1/(z - z_2)\}\} \\
& \cdot \int_0^z dz_1 \int_0^z dz_2 \int_0^\infty d\rho_1 \rho_1 \int_0^\infty d\rho_2 \rho_2 \cdot F_n(\vec{\kappa}, [z_1 - z_2], [z_1 + z_2]/2) \\
& \cdot [z_1 z_2 (z - z_1)(z - z_2)]^{-1} \cdot \text{Exp}\{(ik/2)[1/z_1 - 1/(z - z_1)]\vec{\rho}_1^2\} \\
& \cdot \text{Exp}\{-(ik/2)[1/z_2 - 1/(z - z_2)]\vec{\rho}_2^2\} \cdot \int_0^\pi d\theta_1 \text{Exp}\{-i\vec{\rho}_1 \cdot [k/z_1]\vec{r}_1\} \\
& \cdot \text{Exp}\{i\vec{\rho}_1 \cdot [k/(z - z_1)]\vec{p} - \vec{\kappa}\} \cdot \int_0^\pi d\theta_2 \text{Exp}\{i\vec{\rho}_2 \cdot (k/z_2)\vec{r}_2\} \\
& \cdot \text{Exp}\{i\vec{\rho}_2 \cdot [k/(z - z_2)]\vec{p} + \vec{\kappa}\} \tag{26}
\end{aligned}$$

Note that the limits on the ρ integrations may be extended to infinity because the finite transverse extent of the Gaussian beam will drive the integrand of Eq. (26) to zero for large ρ values.

If I_1 and I_2 are defined as the integrals over θ_1 and θ_2 from Eq. (26) above, then:

$$\begin{aligned}
I_1 = & \pi J_0 \{ \rho_1 | (k/z_1)\vec{r}_1 + [k/(z - z_1)]\vec{p} - \vec{\kappa} | \}, \\
I_2 = & \pi J_0 \{ \rho_2 | (k/z_2)\vec{r}_2 + [k/(z - z_2)]\vec{p} + \vec{\kappa} | \} \tag{27}
\end{aligned}$$

Since:

$$\int_0^\pi d\theta \text{Exp}\{\pm i\vec{\alpha} \cdot \vec{\beta}\} = \pi J_0(\alpha\beta) \tag{28}$$

is an integral representation of the zero'th order Bessel function.³⁴

Thus the evaluation of Eq. (26) will require taking integrals of the form:

$$I = \int_0^{\infty} d\rho \rho \text{Exp}\{\pm i\alpha\rho^2\} J_0(a\rho) \quad (29)$$

This integral form is well known and the result has been tabulated in closed form.³⁴

$$I = (1/2\alpha)\text{Exp}\{\pm i(\pi/2 - a^2/4\alpha)\} \quad (30)$$

After substituting Eqs. (28) and (30) in (26) and performing some simplifications:

$$\begin{aligned} Q(\vec{k}) = & (4\pi^2/k^2z^2)\text{Exp}\{(ik/2)[(\vec{r}_1 - \vec{p})^2 - (\vec{r}_2 - \vec{p})^2]\} \cdot \int_0^z dz_1 \int_0^z dz_2 \\ & \cdot F_n(\vec{k}, [z_1 - z_2], [z_1 + z_2]/2) \\ & \cdot \text{Exp}\{(ik^2/2kz)[z_2(z - z_2) - z_1(z - z_1)]\} \\ & \cdot \text{Exp}\{(ik/2z)[(z_2 - z_1)\vec{p} + (z - z_2)\vec{r}_2 - (z - z_1)\vec{r}_1] \cdot \vec{k}\} \quad (31) \end{aligned}$$

This expression may be evaluated by employing the Markov approximation:^{24,25}

$$F_n(\vec{k}, [z_1 - z_2], [z_1 + z_2]/2) \approx 2\pi\phi_n(\vec{k}, [z_1 + z_2]/2) \cdot \delta(z_1 - z_2) \quad (32)$$

where ϕ_n is the three-dimensional spectrum of the refractive index fluctuations as a function of turbulence strength along the path described by the $[z_1 + z_2]/2$ functional dependence. If $z_1 = z_2$ Eq. (31) simplifies to:

$$Q(\vec{k}) = (8\pi^3/k^2)\text{Exp}\{(ik/2)[(\vec{r}_1 - \vec{p})^2 - (\vec{r}_2 - \vec{p})^2]\} \cdot \int_0^1 dt \phi_n(\vec{k}, tz) \\ \cdot \text{Exp}\{i\vec{k} \cdot (\vec{r}_2 - \vec{r}_1)\} \quad (33)$$

where $z_1 = z_2 \equiv z'$ and $t \equiv (z'/z)$.

Substituting Eq. (33) in Eq. (23) yields:

$$\langle \psi_1(\vec{r}_1, \vec{p}) \psi_1^*(\vec{r}_2, \vec{p}) \rangle = 2\pi^2 k^2 z \int d^2\vec{k} \int_0^1 dt \phi_n(\vec{k}, tz) \text{Exp}\{i\vec{k} \\ \cdot (\vec{r}_1 - \vec{r}_2)\} \quad (34)$$

The turbulent field will be assumed to be isotropic in any plane normal

to the z axis, thus Φ_n may be written in the form:

$$\Phi_n(\vec{k}, tz) = \Phi_n(\kappa, tz) = C_n^2(tz)\Phi_n^0(\kappa) \quad (35)$$

where Φ_n^0 is the modified von Karman spectrum given below.

$$\Phi_n^0 = \text{Exp}\{-\kappa^2/\kappa_m^2\}/(\kappa^2 + \kappa_0^2)^{11/6} \quad (36)$$

$C_n^2(tz)$ models the change in turbulence strength as a function of position along the propagation path. κ_m and κ_0 are given by $2\pi/l_0$ and $2\pi/L_0$ respectively where l_0 is the inner scale of the turbulence and L_0 is the outer scale.^{24,25} Substituting Eq. (35) in Eq. (34) yields:

$$\langle \psi_1(\vec{r}_1, \vec{p}) \psi_1(\vec{r}_2, \vec{p}) \rangle = 2\pi^2 k^2 z \int_0^1 dt C_n^2(zt) \int d^2\vec{k} \Phi_n(\kappa) J_0(|a\kappa|) \quad (37)$$

where $r = |\vec{r}_1 - \vec{r}_2|$ and $a = (1 - t)r$.

In the following discussion, the term I will refer to the integration over d^2k in Eq. (37). Due to the complexity of this relationship it is not possible to evaluate I in closed form. Note however, that the integrand of I goes to zero for values of $\kappa \gg \kappa_m$ and thus appropriate approximations may be employed. Previous work done at NASA-Ames indicates that the inner and outer scale sizes of the turbulence are on the order of 0.2 mm and 1.0 cm respectively and thus

$\kappa_m \sim 10^4 \text{ m}^{-1}$ and since $r < 1.0 \text{ cm}$, $ak < 10^2$. This means that the Gaussian exponential in Φ_n varies slowly over the nonzero range of the integrand in I. The exponential term may be expanded and the resulting series expansion of I be evaluated term by term to yield:³⁵

$$\begin{aligned} I &= [1/\Gamma(11/6)](a/2\kappa_0)^{5/6} \kappa_{-5/6}(a\kappa_0) + O(|a\kappa_m|^{-2}) \\ &\approx (3/5)\kappa_0^{5/3} [1 - 1.86(a\kappa_0)^{5/3}] \end{aligned} \quad (38)$$

Therefore:

$$\begin{aligned} \langle \psi_1(\vec{r}_1, \vec{p}) \psi_1(\vec{r}_2, \vec{p}) \rangle &= (6/5)(\pi^2 k^2 a / \kappa_0^{5/3}) \int_0^1 dt C_n^2(zt) \\ &\cdot [1 - 1.86(\kappa_0 a)^{5/3}] \end{aligned} \quad (39)$$

Now consider the form of C_n^2 . Since the strength of the turbulence will be at a maximum near the walls of the wind tunnel and decrease rapidly with distance away from the walls, the strength function will be modeled using two Gaussian terms.

$$C_n^2(T) = C_n^2 \cdot [\text{Exp}\{-4T^2/L_0^2\} + \text{Exp}\{-4(T - D)^2/L_0^2\}] \quad (40)$$

where L_0 is the outer scale length, D is the width of the flow nozzle and C_n^2 is a proportionality constant yet to be evaluated that represents the maximum turbulence strength found at the walls.

By definition:^{24,25}

$$\langle n_1^2(\vec{x}) \rangle = B_n(0) \quad (41)$$

where B_n is the refractive index covariance function. For the region of maximum turbulence near the walls:^{24,25}

$$\langle n_1^2(\vec{x}) \rangle = \int d^3\kappa \Phi_n(\kappa) = C_n^2 \int d^3\kappa \Phi_n^0(\kappa) \quad (42)$$

Eq. (42) may be evaluated by elementary means yielding:

$$\begin{aligned} \langle n_1^2 \rangle &= 15.9 C_n^2 / \kappa_0^{2/3} \\ C_n^2 &= 0.063 \kappa_0^{2/3} \langle n_1^2 \rangle \end{aligned} \quad (43)$$

The evaluation of Eq. (39) will require integrals of the form:

$$\begin{aligned} I_1 &= \int_0^1 dt \{ \text{Exp}\{-4(z^2 t^2 / L_0^2 + [zt - D]^2 / L_0^2)\} \\ I_2 &= \int_0^1 dt (1 - t)^{5/3} \cdot \text{Exp}\{-4(z^2 t^2 / L_0^2 + [zt - D]^2 / L_0^2)\} \end{aligned} \quad (44)$$

Since $z \gg L_0$, I_1 may be evaluated using elementary methods:

$$I_1 = [(\pi)^{1/2} L_0 / 2z] C_n^2 \quad (45)$$

Noting that the integrand of I_2 will be nonzero only over the ranges $0 \leq t \leq L_0/z$ and $(D - L_0)/z \leq t \leq D/z$, the term $(1 - t)^{5/3}$ may be expanded D/z in powers of t (assuming $z > D$) and I_2 evaluated.

$$I_2 = [(\pi)^{1/2} L_0 / 4z] C_n^2 \alpha_T$$

$$\alpha_T \equiv 1 - (5L_0/6[\pi]^{1/2} z) + 2(1 - D/z)^{5/3} + (5D/3z)(1 - D/z)^{2/3} + (5L_0/3[\pi]^{1/2} z)(1 - D/z)^{2/3} \quad (46)$$

Using Eqs. (45) and (46):

$$\langle \psi_1(\vec{r}_1, \vec{p}) \psi_1^*(\vec{r}_2, \vec{p}) \rangle = (6\pi^{5/2} k^2 L_0 / \kappa_0^{5/3}) [1 - 0.93\alpha_T (r\kappa_0)^{5/3}] C_n^2 \quad (47)$$

$$F = \text{Exp}\{-\tilde{A}r^{5/3}\}$$

$$\tilde{A} = 1.12\pi^{5/2} k^2 L_0 C_n^2 \alpha_T \quad (48)$$

Substituting Eq. (48) into Eq. (13), employing the paraxial approximation ($\rho = [p, z]$) and changing integration variables to $r = r_1 - r_2$ and $R = (r_1 + r_2)/2$, yields:

$$\begin{aligned} \langle I(\vec{p}) \rangle = & (k^2/4\pi^2 z^2) \int d^2\vec{r} \text{Exp}\{-\tilde{A}r^{5/3}\} \int d^2\vec{R} U_A(\vec{R} + \vec{r}/2) U_A^*(\vec{R} - \vec{r}/2) \\ & \cdot \text{Exp}\{(ik/2)[\vec{r} \cdot (\vec{R} - \vec{p})]\} \end{aligned} \quad (49)$$

The exponential term $\text{Exp}\{-\tilde{A}r^{5/3}\}$ prevents a closed form evaluation of Eq. (49). In order to proceed from this point, the offending term will be approximated by a Gaussian exponential of the form $\text{Exp}\{-Ar^2\}$ as defined by:

$$\int dr (\text{Exp}\{-\tilde{A}r^{5/3}\} - \text{Exp}\{-Ar^2\}) = 0 \quad (50)$$

This type of approximation has been previously employed by Fante, who matched the $r^{5/3}$ exponential with a Gaussian at the $1/e$ point, and also by Leader.^{36,37} This substitution forces the structure function to have a quadratic dependence on r and, consequently, is incapable of modeling some turbulence effects. Wandzura has shown that a quadratic structure function is equivalent to a linear phase perturbation superimposed on the original spherical waveform.³⁸ A perturbation of this form is capable of modeling only random phase tilts and cannot provide information pertaining to such effects as short term beam spread, beam breakup in strong turbulence and scintillation.³⁸ It is quite useful, however, for modeling wander of a narrow beam induced by the turbulent field. It will be shown in Chapter V that such deflections can be used to test the validity of the extended Huygens-Fresnel theory to model the

effects of a supersonic turbulent field and also provide a flexible remote sensing technique. For the purpose of this work, no practical loss of generality will be incurred by using the quadratic structure function.

The quadratic fit of Eq. (50) provides a better match over the range where $\text{Exp}\{-\tilde{A}r^{5/3}\} \sim 1$ than the method employed by Fante and does not significantly alter the cutoff point of the integrand in Eq. (49).³⁶ The evaluation of Eq. (50) yields:

$$A = \pi / [\Gamma^2(8/5)] \tilde{A}^{-6/5} = 0.983 \tilde{A}^{-6/5} \quad (51)$$

Substituting this Gaussian approximation in Eq. (49) gives an expression which may be evaluated by elementary methods and the use of appropriate integral tables. U_A is the electric field across the input (or source) plane and has been taken to be in the form of a TEM_{00} laser beam. The average irradiance in the observation plane is thus given by:

$$\begin{aligned} \langle I(p) \rangle &= (k^2/z^2) [|U_A|^2 / (1 + 4f^2/b^2)] \cdot (1/4B\gamma) \\ &\quad \cdot \text{Exp}\{-(k^2/4Bz^2)[1 - N^2/4B\gamma]p^2\} \\ &= (k^2/z^2) [|U_A|^2 / (1 + 4f^2/b^2)] \cdot [1/(N^2 + 16BT)] \\ &\quad \cdot \text{Exp}\{-(k^2/4Bz^2)[1/(1 + N^2/16BT)]p^2\} \end{aligned} \quad (52)$$

where f is the distance from the source plane to the beam waist and:

$$\begin{aligned}
b &= kw_0^2 \text{ (beam confocal parameter)} \\
T &= kb/[2(b^2 + 4f^2)] \\
N &= k[(1/z) - (4f/(b^2 + 4f^2))] \\
B &= A + T \\
\gamma &= 4t + N^2/4B
\end{aligned} \tag{53}$$

D. Mean Output Irradiance with Centerline Turbulence

It is possible to generalize the above result to include a region of turbulent flow near the center of the Ludwig tube. For the purpose of this calculation, the strength of the turbulence in the center will be taken to be a Gaussian function of the following form:

$$\begin{aligned}
C_n^2(T) &= C_n^2 [\text{Exp}\{-4T^2/L_0^2\} \text{Exp}\{-16(T - D/2)^2/d^2\} \\
&\quad \text{Exp}\{4(T - D)^2/L_0^2\}]
\end{aligned} \tag{54}$$

where d will be called the width of the center turbulence packet. Note that this quantity is not a measure of half width at half maximum amplitude.

The methods of analysis required for this calculation are virtually identical to those used in the mean irradiance case with the exception of the expression for $\langle \psi_1(r_1, p) \psi_1^*(r_2, p) \rangle$. Eq. (39) may be employed. This definition provides a better match over the range where $\text{Exp}\{-\tilde{A}r^{5/3}\} \sim 1$, and does not significantly alter the cutoff point of

the integrand in Eq. (49).

If $C_n^2(zt)$ is now given by (54). Evaluation of this new expression will require integrals of the form:

$$I = \int_0^1 dt \text{Exp}\{[-4z^2 t^2/L_0^2] - [16(zt - D/2)^2/d^2] - [4(T - D)^2/L_0^2]\} \\ \cdot (1 - t)^{5/3} \quad (55)$$

Equation (55) may be evaluated term by term by expanding the function $(1 - t)^{5/3}$ about the points 0, $D/2z$, and D/z . Using the facts that z is much greater than L_0 , and d less than or on the order of $D/3$, F may be written in the form:

$$F = \text{Exp}\{-\langle |\psi_1|^2 \rangle - \langle \psi_1(\vec{r}_1, \vec{p}) \psi_1(\vec{r}_2, \vec{p}) \rangle\} \\ = \text{Exp}\{-\tilde{A}_1 r^{5/3}\} \quad (56)$$

where:

$$\tilde{A}_1 = 1.12 \pi^{5/2} k^2 L_0 C_n^2 \alpha_T' \quad (57)$$

$$\alpha_T' = 1 - \langle 5L_0/[\pi]^{1/2} z \rangle + (d/L_0) \{a_1 - (D/2z)a_2 + a_3(D^2/4z^2 + d^2/32z^2)\} \\ + \{2c_1 + c_2(D - L_0/[\pi]^{1/2})\} \quad (58a)$$

$$\begin{aligned}
a_1 &= (1 - D/2z)^{5/3} + (5D/6z)(1 - D/2z)^{2/3} + (5d^2/36z^2)(1 - D/2z)^{-1/3} \\
a_2 &= (5/3)[(1 - D/2z)^{2/3} + (D/3z)(1 - D/2z)^{-1/3}] \\
a_3 &= (5/9)(1 - D/2z)^{-1/3}
\end{aligned} \tag{58b}$$

$$\begin{aligned}
c_1 &= (1 - D/z)^{5/3} + (5D/3z)(1 - D/z)^{2/3} \\
c_2 &= (-5/3)(1 - D/z)^{2/3}
\end{aligned} \tag{58c}$$

If F is approximated by the Gaussian exponential $\text{Exp}\{-A_1 r^2\}$, where A_1 is defined by the relation given in Eq. (50), the result is a form identical to Eq. (52) with:

$$B = A_1 + T \tag{59}$$

$$\gamma = 4T + N^2/4B \tag{60}$$

E. Intensity Covariance Function

The formulation of the intensity covariance function requires an expression of the form:

$$\langle I(\vec{p}_1)I(\vec{p}_2) \rangle = \langle U(\vec{p}_1)U^*(\vec{p}_1)U(\vec{p}_2)U^*(\vec{p}_2) \rangle \tag{61}$$

which may be written in terms of the extended Huygens-Fresnel theory:

$$\begin{aligned}
\langle I(\vec{p}_1)I(\vec{p}_2) \rangle &= (k^4/2\pi^2) \int d^2\vec{r}_1 \int d^2\vec{r}_2 \int d^2\vec{r}_3 \int d^2\vec{r}_4 U_A(\vec{r}_1)U_A^*(\vec{r}_2) \\
&\quad \cdot U_A(\vec{r}_3)U_A^*(\vec{r}_4) \cdot \text{Exp}\{(ik/2z)[r_1^2 - r_2^2 + 2\vec{p}_1 \cdot (\vec{r}_2 - \vec{r}_1)]\} \\
&\quad \cdot \text{Exp}\{(ik/2z)[r_3^2 - r_4^2 + 2\vec{p}_2 \cdot (\vec{r}_4 - \vec{r}_3)]\} \cdot F' \quad (62)
\end{aligned}$$

where:

$$F' = \langle \text{Exp}\{\psi(\vec{r}_1, \vec{p}_1) + \psi^*(\vec{r}_2, \vec{p}_1) + \psi(\vec{r}_3, \vec{p}_2) + \psi^*(\vec{r}_4, \vec{p}_2)\} \rangle \quad (63)$$

After Yura:³²

$$\begin{aligned}
F' &= \text{Exp}\{-[2\langle |\psi_1|^2 \rangle - \langle \psi_1(\vec{r}_1, \vec{p}_1)\psi_1^*(\vec{r}_2, \vec{p}_1) \rangle - \langle \psi_1(\vec{r}_1, \vec{p}_1)\psi_1(\vec{r}_3, \vec{p}_2) \rangle \\
&\quad - \langle \psi_1(\vec{r}_1, \vec{p}_1)\psi_1^*(\vec{r}_4, \vec{p}_2) \rangle - \langle \psi_1^*(\vec{r}_2, \vec{p}_1)\psi_1(\vec{r}_3, \vec{p}_2) \rangle \\
&\quad - \langle \psi_1^*(\vec{r}_2, \vec{p}_1)\psi_1^*(\vec{r}_4, \vec{p}_2) \rangle - \langle \psi_1(\vec{r}_3, \vec{p}_2)\psi_1^*(\vec{r}_4, \vec{p}_2) \rangle]\} \quad (64)
\end{aligned}$$

Using the techniques of the preceding calculations along with the Markov and paraxial approximations, each term in Eq. (64) may be shown to be proportional to a function of the form:

$$f = \int d\vec{k} Q(\vec{k}) \quad (65)$$

where:

$$Q(\vec{k}) = \int_0^{z'} dz' \Phi_n(\vec{k}, z') J_0(\vec{k} \cdot [a + x\vec{k}]) \quad (66)$$

and:

$$a = |(z'/z)(\vec{p}_j - \vec{p}_h) + (1 - z'/z)(\vec{r}_i - \vec{r}_e)|$$

$$x = z'(1 - z'/z)/2k \quad (67)$$

the subscripts in Eq. (67) correspond to the subscripts on r and p in each term of Eq. (64). Φ_n is given by:

$$\Phi_n(\vec{k}, z') = c_n^2(z') \Phi_n^0(\vec{k}) \quad (68)$$

where c_n^2 and Φ_n^0 are given by Eqs. (40) and (36) respectively. c_n^2 will be nonzero only over small ranges centered on the points $z' = 0$ and $z' = D$. Over these ranges, $x \ll 1$ and $\vec{k} \cdot (a + x\vec{k}) \sim a\kappa$. Therefore:

$$Q(\kappa) \approx \int_0^{z'} dz' \Phi_n(\vec{\kappa}, zt) J_0(a\kappa) \quad (69)$$

If p_2 is taken to be on the propagation axis ($p_2 = 0$),

$$Q(\vec{\kappa}) \approx \int_0^1 dt \Phi_n(\vec{\kappa}, zt) J_0(|t\vec{p} + (1-t)\vec{r}_{i1}| \kappa) \quad (70a)$$

Since $a\kappa_m \gg 1$:

$$f \approx (3/5)\kappa_0^{5/3} [1 - 1.86\kappa_0^{5/3} |t\vec{p} + (1-t)\vec{r}_{i1}|^{5/3}] \quad (70b)$$

and each argument term in Eq. (64) will depend on an integral of the form:

$$I = \int_0^1 dt C_n^2(zt) |t\vec{p} + (1-t)\vec{r}_{i1}|^{5/3} \quad (71)$$

$$= r_{i1}^{5/3} \int_0^1 dt (1-t)^{5/3} \text{Exp}\{-4z^2 t^2 / L_0^2\} \\ + p^{5/3} \int_0^1 dt t^{5/3} \text{Exp}\{4(2t - D)^2 / L_0^2\} \quad (72)$$

Methods for the evaluation of Eq. (72) have been given in the previous calculations. F' may be written in closed form as:

$$F' = \text{Exp}\{-\tilde{A}[r_{12}^{5/3} - r_{13}^{5/3} + r_{14}^{5/3} + r_{23}^{5/3} - r_{24}^{5/3} + r_{34}^{5/3}]\} \quad (73)$$

where \tilde{A} is specified by Eq. (48). If each $5/3$ 'rds power term in the exponential is approximated by a Gaussian as done in the previous calculations, it is possible to arrive at a closed form expression for $\langle I(\vec{p})I(0) \rangle$. (See section C for a discussion of the limitations imposed on the theory by this approximation.)

$$\begin{aligned} \langle I(\vec{p})I(0) \rangle &= (k^4/z^4)[|U_0|^2/(1 + 4f^2/b^2)] \cdot [1/16B\beta\beta'\beta''] \\ &\cdot \text{Exp}\{-(k^2p^2/4Bz^2)[B/\beta - N^2A^2/4\beta'\beta^2B - N^2B/4\beta''\beta^2]\} \\ &\cdot \text{Exp}\{-(k^2p^2/4Bz^2)[N^4A^2/4\beta''\beta'\beta^3B - N^6A^4/64\beta''\beta'^2\beta^4B^2]\} \quad (74) \end{aligned}$$

where:

$$\begin{aligned} B &= A + T \\ \beta &= B - A^2/B \\ \beta' &= 4T + N^2/4B + n^2A^2/4\beta B^2 \\ \beta'' &= 4T + N^2/4\beta - N^4A^2/16\beta'\beta^2B^2 \quad (75) \end{aligned}$$

A necessary condition for the validity of Eq. (74) is that $\beta'' > 0$. By definition:

$$B_I(\vec{p}) = \langle I(\vec{p})I(0) \rangle - \langle I(\vec{p}) \rangle \langle I(0) \rangle \quad (76)$$

Thus the intensity covariance function may be formed using Eqs. (52) and (74) along with definition (76).

F. Equal Path Length Interferometer

The final case that will be considered consists of inserting the flow nozzle into one arm of an equal path length interferometer. The complex field amplitude at a point p in the receiver plane will be the superposition of the two fields transmitted by each arm of the interferometer.

$$U_r(\vec{p}) = U_0(\vec{p}) + U_1(\vec{p}) \quad (77)$$

If the Ludwig tube is placed in arm 1 of the interferometer, each field component may be written in terms of the extended Huygens-Fresnel theory.

$$U_0 = (ik/2\pi) \int d^2\vec{r}_1 U_A(\vec{r}_1) \cdot \text{Exp}\{ik|\vec{r}_1 - \vec{p}|\} / |\vec{r}_1 - \vec{p}| \quad (78)$$

$$U_1 = (-ik/2\pi) \int d^2\vec{r}_2 U_A(\vec{r}_2) \cdot \text{Exp}\{ik|\vec{r}_2 - \vec{p}| + \psi(\vec{r}_2, \vec{p})\} / |\vec{r}_2 - \vec{p}| \quad (79)$$

where:

$$\vec{\rho} = (\vec{p}, z) \quad (80)$$

Thus:

$$\begin{aligned} \langle I_r(\vec{\rho}) \rangle &= \langle U_0(\vec{\rho})U_0^*(\vec{\rho}) + U_1(\vec{\rho})U_1^*(\vec{\rho}) + U_0(\vec{\rho})U_1^*(\vec{\rho}) + U_0^*(\vec{\rho})U_1(\vec{\rho}) \rangle \\ &= I_0(\vec{\rho}) + \langle I_1(\vec{\rho}) \rangle + \langle U_0(\vec{\rho})U_1^*(\vec{\rho}) \rangle + \langle U_1(\vec{\rho})U_0(\vec{\rho}) \rangle \end{aligned} \quad (81)$$

From previous calculations:

$$\begin{aligned} I_0(\vec{\rho}) &= (k^2/z^2) [|U|^2 / (1 + 4f^2/b^2)] \cdot [1 / (n^2 + 16T^2)] \\ &\quad \cdot \text{Exp}\{ -(k^2 p^2 / 4Tz^2) [16T^2 / (N^2 + 16T^2)] \} \\ \langle I_1(\vec{\rho}) \rangle &= (k^2/z^2) [|u|^2 / (1 + 4f^2/b^2)] \cdot [1 / (N^2 + 16BT)] \\ &\quad \cdot \text{Exp}\{ -(k^2 p^2 / 4Bz^2) [16T^2 / (N^2 + 16BT)] \} \end{aligned} \quad (82)$$

Using Eqs. (78) and (79):

$$\begin{aligned} \langle U_1(\vec{\rho})U_0^*(\vec{\rho}) \rangle &= (k^2/4\pi^2 z^2) \int d^2\vec{r}_1 \int d^2\vec{r}_2 U_A(\vec{r}_1)U_A^*(\vec{r}_2) \\ &\quad \cdot \text{Exp}\{ (ik/2z) [r_2^2 - r_1^2 + 2\vec{\rho} \cdot (\vec{r}_1 - \vec{r}_2)] \} \cdot P'' \end{aligned} \quad (83)$$

where:

$$F'' = \langle \text{Exp}\{\psi(\vec{r}_1, \vec{p})\} \rangle \quad (84)$$

If $\psi = \psi_1 + \psi_2$ where $\psi_1 \sim n_1$ and $\psi_2 \sim n_1^2$:

$$\langle \text{Exp}\{\psi\} \rangle \approx \text{Exp}\{\langle \psi_2 \rangle + \langle \psi_1^2 \rangle / 2\} \quad (85)$$

After Yura:³³

$$\langle \psi_2 \rangle = \langle \phi_2 \rangle - \langle \psi_1^2 \rangle / 2 = -[\langle |\psi_1|^2 \rangle + \langle \psi_1^2 \rangle] / 2 \quad (86)$$

Therefore:

$$F'' = \text{Exp}\{-\langle |\psi_1|^2 \rangle\} \quad (87)$$

From the previous calculations:

$$\begin{aligned} \langle |\psi_1|^2 \rangle = \langle \psi_1(\vec{r}_1, \vec{p}) \psi_1^*(\vec{r}_2, \vec{p}) \rangle &= 4\pi^2 k^2 z \int_0^1 dt C_n^2(z t) \int_0^\infty d\kappa \kappa \Phi_n^0(\kappa) \\ &\cdot J_0[(1-t)r_{12}\kappa] \end{aligned} \quad (88)$$

evaluated at:

$$r_{12} = |\vec{r}_1 - \vec{r}_2| = |\vec{r} - \vec{r}| = 0 \quad (89)$$

Thus:

$$\langle |\psi_1|^2 \rangle = 4\pi^2 k^2 z \int_0^1 dt C_n^2(zt) \int_0^\infty dk \kappa \Phi_n^0(\kappa) \quad (90)$$

where C_n^2 and Φ_n^0 have been previously defined. I_1 will be defined as the integration over dt in Eq. (90) and I_2 will be defined as the integration over dk . I_1 has been previously evaluated and I_2 may be evaluated with the help of a previously tabulated form.³⁹

$$\langle |\psi_1|^2 \rangle = (6\pi^{5/2} k^2 z C_n^2 / 5\kappa_0^{5/3}) \cdot \alpha \quad (91)$$

where:

$$\alpha = 1 + D/2L_0 \quad (92)$$

Thus:

$$F'' = \text{Exp}\{-\beta_2\} \quad (93a)$$

where:

$$\beta_2 = \langle |\psi_1|^2 \rangle \quad (93b)$$

Using the methods employed in the previous calculations:

$$\begin{aligned} \langle U_1(\vec{p}) U_0^*(\vec{p}) \rangle &= (k^2/z^2) [|U_0|^2 / (1 + 4f^2/b^2)] \cdot \text{Exp}\{-\beta_2\} \\ &\cdot \text{Exp}\{-(k^2 p^2 / 4Tz^2) [16T^2 / (N^2 + 16T^2)] \} \end{aligned} \quad (94)$$

and likewise:

$$\langle U_0(\vec{p}) U_1^*(\vec{p}) \rangle = \langle U_1(\vec{p}) U_0^*(\vec{p}) \rangle \quad (95)$$

Thus using Eqs. (82), (94) and (95), (81) may be written in the form:

$$\begin{aligned} \langle I_r(\vec{p}) \rangle &= (k^2/z^2) [|U_0|^2 / (1 + 4f^2/b^2)] \cdot [(1 - 2\text{Exp}\{-\beta\}) / (N^2 + 16 T^2)] \\ &\cdot \text{Exp}\{-(k^2 p^2 / z^2) [4T / (N^2 + 16BT)] \} \cdot \text{Exp}\{-(k^2 p^2 / z^2) [4T / (N^2 + 16T^2)] \} \\ &\cdot \text{Exp}\{1 / (N^2 + 16BT) \} \end{aligned} \quad (96)$$

G. Conclusions

It is apparent from the form of the preceding calculations that all the cases treated are capable of providing information about the

existence of turbulence in the Ludwig flow nozzle and limited statistical information about the characteristics (C_n^2 , L_0 and δ). None of the cases presented here can form the basis for a "turbulence meter", capable of providing spatially resolved measurements, on its own. This is due to the fundamental scale sizes of the turbulent field and their effects on the spatial filter functions as summarized by Ishimaru^{27,28} and evident in the functional nature of A.

In all cases, the measurable quantities reflect a complicated superposition of effects from each differential length element, dz , along the optical path z . There is no apparent method to separate the effects produced by turbulence at one point along the path from those produced by turbulence at any other point, and thus there is no way to probe the turbulence within the flow nozzle with any spatial resolution.

Also, although it is quite feasible to measure A, these methods will not allow the direct measurement of C_n^2 , L_0 , l_0 or d . Knowing the value of A provides one only with a knowledge of the product of the parameters of interest (see Eq. (48) for example). Since the dependence of each method on the turbulence parameters is identical, no one method or combination of methods will allow the determination of the individual parameters. It is quite possible, however, that these models in conjunction with the use of multiple beams and appropriate calibration methods may contribute to the design of a practical technique for the remote measurement of turbulent fields in a compressible flow.

It is also apparent that any one of the cases treated here could provide the basis for an experiment to test the validity of the extended

Huygens-Fresnel formalism in modeling the effects of a known supersonic turbulent field on laser beam propagation and thus determine the usefulness of the "atmospheric" approach to remote wind tunnel measurements. Figure 27 provides a schematic diagram of one possible single beam experiment using a low power laser and uncoated, off-the-shelf optics. The TEM_{00} beam propagates through the turbulent field in the flow nozzle and then is incident upon a circular aperture having a radius approximately equal to that of the beam. Figure 31 plots the time-averaged power (Eq. (52) integrated over the blocking aperture) as a function of the distance (Z) between the input window of the flow nozzle and the plane of the aperture. The symbol b represents the confocal parameter of the beam:

$$b \equiv kw_0^2 \quad (97)$$

and is a very useful figure of merit indicating the "tightness" of the focusing and, consequently, the spot radius of the beam.⁴⁰ It is obvious that the detailed structure shown in Fig. 31 may be compared to experimental data directly with a good match providing very strong and unambiguous evidence of a valid theoretical model.

This is, in fact, just the approach employed in chapters V and VI to draw conclusions not only regarding the validity of EHF theory but also to suggest possible experimental schemes that have the potential for providing the physical basis of a remote turbulence "meter" suitable for use in bounded, supersonic flows.

CHAPTER IV

PITOT TUBE/HOT WIRE ANEMOMETRY OF THE LUDWIG TUBE FLOW

A. Introduction

As noted in the previous chapters, one of the most fundamental goals of this work is the determination of the validity of extended Huygens-Fresnel formalism in modeling the turbulent field in a bounded, supersonic flow such as that produced in a laboratory scale wind tunnel. Chapter III has suggested several experiments capable of such a determination, but all such experiments depend upon having access to a well-characterized turbulent flow where the important turbulence parameters have been measured by some independent, outside technique. The accuracy with which the flow can be characterized will, in turn, determine the accuracy of the conclusions drawn from these experiments.

For decades, researchers in the field of fluid dynamics have characterized both compressible and incompressible fluid flows using two intrusive measurement techniques known as pitot tube and hot wire anemometry.⁴¹⁻⁴⁶ These methods require the presence of physical transducers in the flow path and, consequently, have a rather limited usefulness when applied to supersonic (compressible) flow. (See Chapters I and II for a discussion of the reasons for these limitations). It is

possible to use these techniques in the case of the Ludwieg tube flow nozzle described in Chapter II, albeit at the expense of some high frequency information, with quite reasonable accuracy. It is not, however, a trival matter to design the necessary hardware to allow the positioning of a hot wire transducer in a supersonic flow without drastically altering the characteristics of the flow.⁴³

A pitot tube (see Figure 3) consists of a hollow tube with a fairly small outer diameter compared to the dimensions of the turbulent field. When inserted in the flow region, the pressure in this tube can be related to the local "instantaneous" pressure of the working fluid at the point of insertion. From this pressure measurement, and a knowledge of some of the basic thermodynamical principles governing the flow (such as adiabatic or non-adiabatic isolation, free or driven expansion of the working fluid through the firing valve, etc.), the basic flow parameters may be computed. These parameters include pressure, density, temperature, velocity and, in the case of compressible flow, the Mach number. While this device is capable of providing a highly linear dynamic response, even a small pitot tube has a very limited frequency bandwidth on the order of 1-5 kHz (hence the use of quotation marks in the sentence above) and thus it is capable of measuring only the average (low frequency component) of the fluctuating flow parameters. This means that pitot tube anemometry alone will not be sufficient to adequately characterize the flow for the purposes of this work, but may be used in conjunction with another, higher speed measurement technique known as hot wire anemometry to glean the necessary knowledge of the

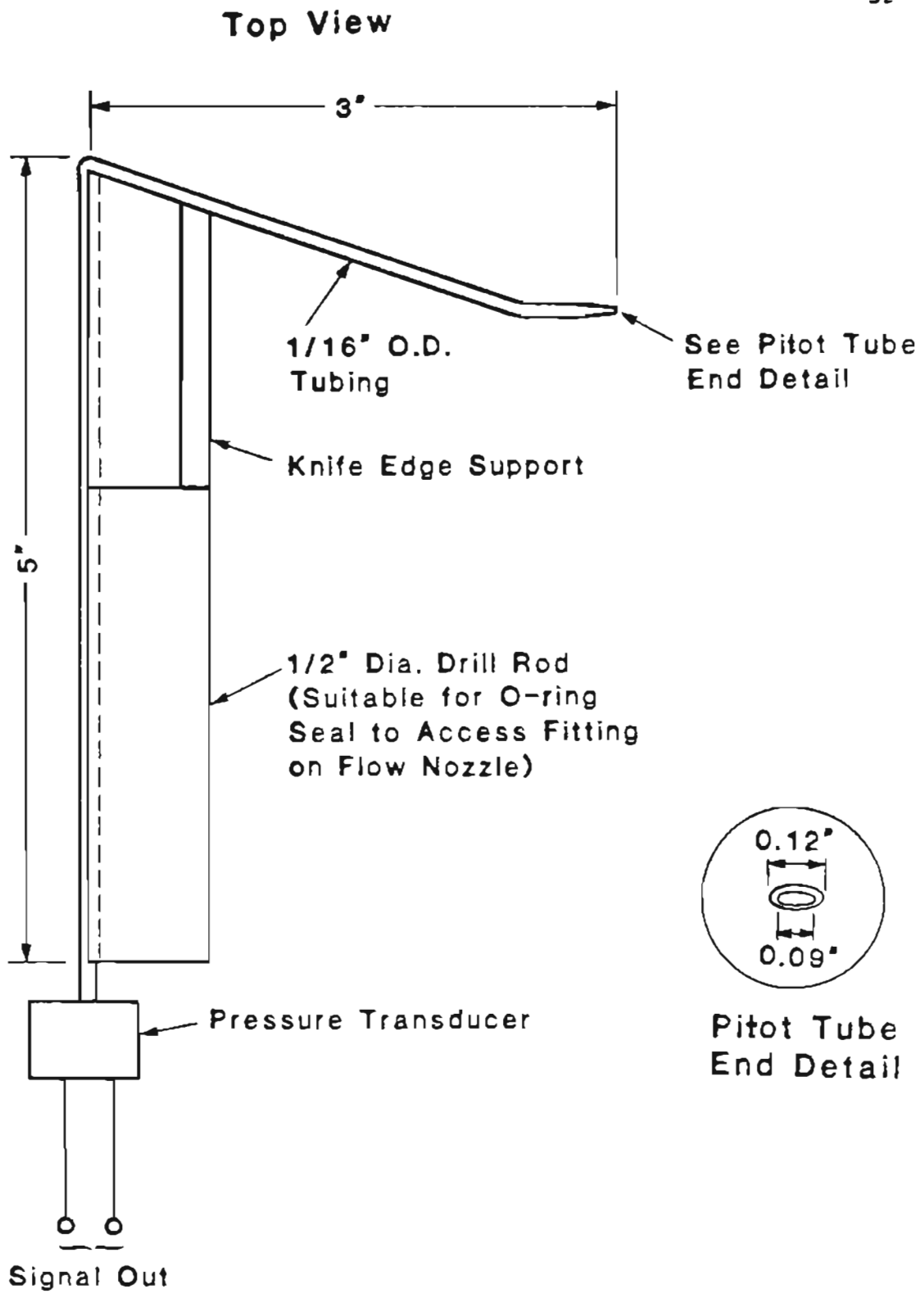


FIGURE 3. Pitot Tube Assembly

turbulence parameters.

As its name implies, the hot wire anemometer is based on a small heated filament with dimensions greater than or on the order of 5 μ m diameter by 1mm in length (see Figure 4). The device senses the exchange of heat between the wire and its local surroundings with an external bridge circuit and thus provides the basic information from which the important flow parameters may be calculated.⁴⁷ While this heat exchange information is an integrated measurement over the length of the wire and the exposed up-wind surface area, the very small physical dimensions of the wire provide at least limited spatial resolution in the flow. The hot wire anemometer is capable of providing at least an order of magnitude improvement in frequency response over that of the pitot tube instrument (on the order of 70-100 kHz), but suffers from the fact that it has a highly nonlinear dynamic response with an output that requires at least a two-step data reduction in order to measure the important flow parameters (density, temperature, velocity, etc.).⁴¹⁻⁴⁷ These facts serve to drastically complicate a theoretical analysis of the response of the hot wire anemometer in a compressible flow, and thus require the development of an appropriate calibration technique.⁴⁷

While the pitot tube instrument does not have the frequency response to measure more than the mean of the fluctuating quantities, this averaged information may be conveniently used to calibrate the hot wire anemometer with its correspondingly higher frequency response. Over the years, the two techniques have been merged to become probably

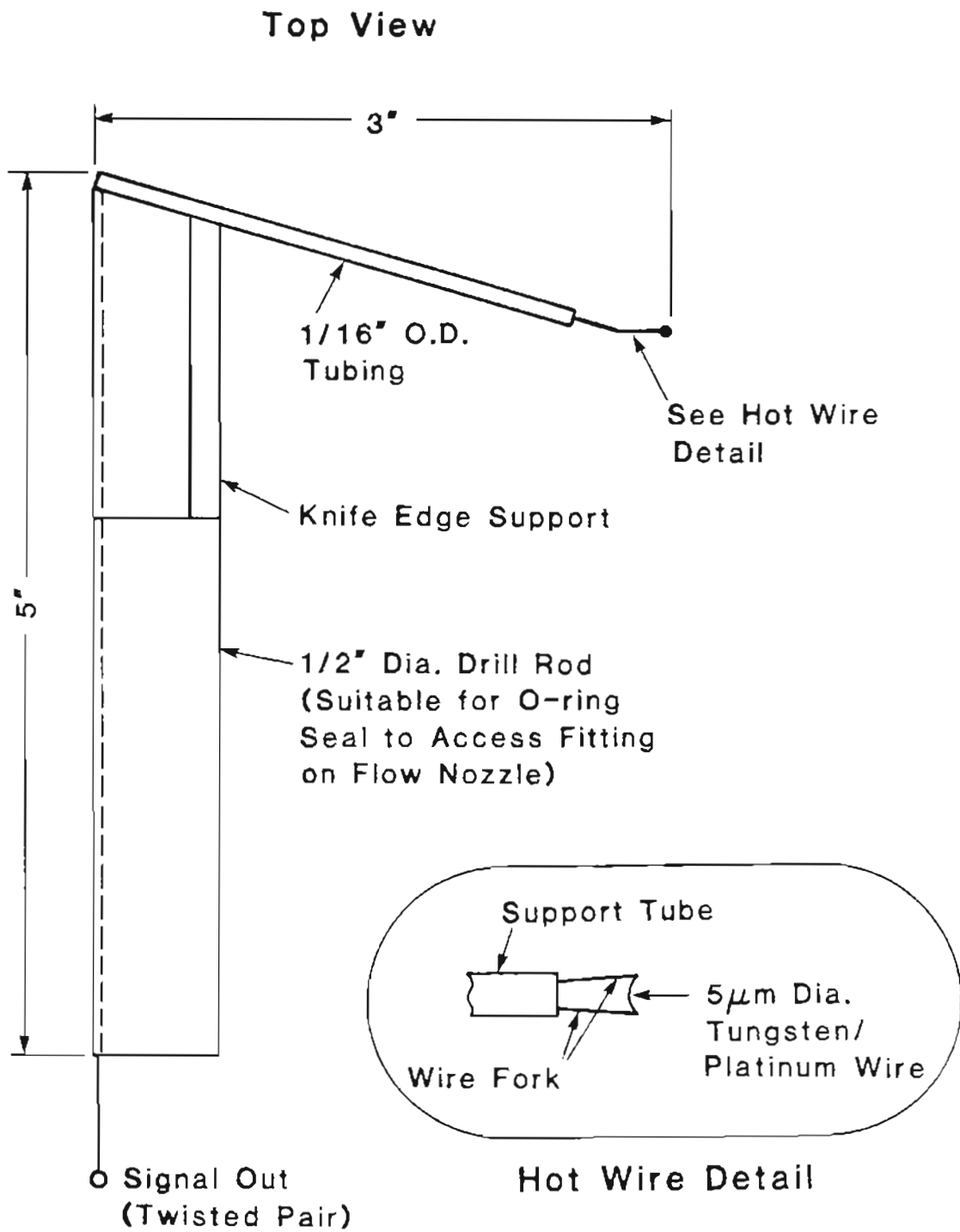


FIGURE 4. Hot Wire Probe Assembly

the most commonly used intrusive measurement method in the field of experimental fluid dynamics.

B. Analysis and Results of the Measurement of the Ludwig Tube Flow using a Pitot Tube Anemometer

A schematic representation of the experiment is shown in Figure 5. The basic flow nozzle was modified with a down-stream access port which allowed the insertion of a raked pitot tube (see Figure 6). The pitot tube was positioned to sample the local flow in the region of the optical windows and could be scanned in transverse location with a micrometer translation stage (see Figure 6).

The original design called for a knife edge support which was 1/8 in. in thickness to minimize flexing of the mount in the flow. This was impossible to achieve, however, as this particular flow nozzle was designed with very little excess longitudinal taper and thus a foreign object of greater than 1/16 in thickness caused the flow to "choke off", that is, the flow velocity became subsonic with a resultant thickening of the turbulent boundary layers to encompass the entire cross sectional area of the nozzle. Figure 7 presents a series of shadowgraph photos (see Chapter I) showing the unobstructed flow, the flow perturbations produced by the presence of a 1/8 in.-thick knife edge alone, and the flow produced by the final pitot tube/knife edge design.

As illustrated in Figure 3, the pressure in the tube is detected by means of a pressure transducer which senses the change in the capacitance of a parallel plate capacitor as one plate is deflected by

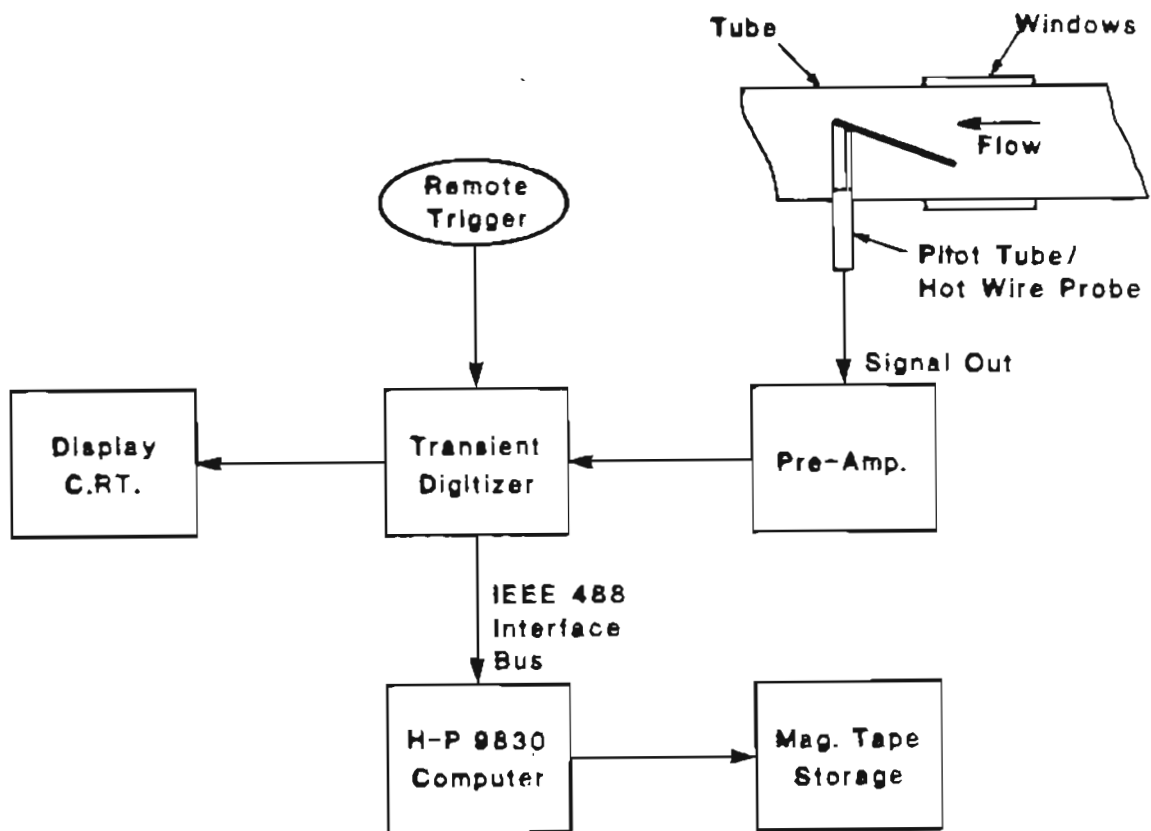


FIGURE 5. Block Diagram of the Pitot Tube/Hot Wire Measurements

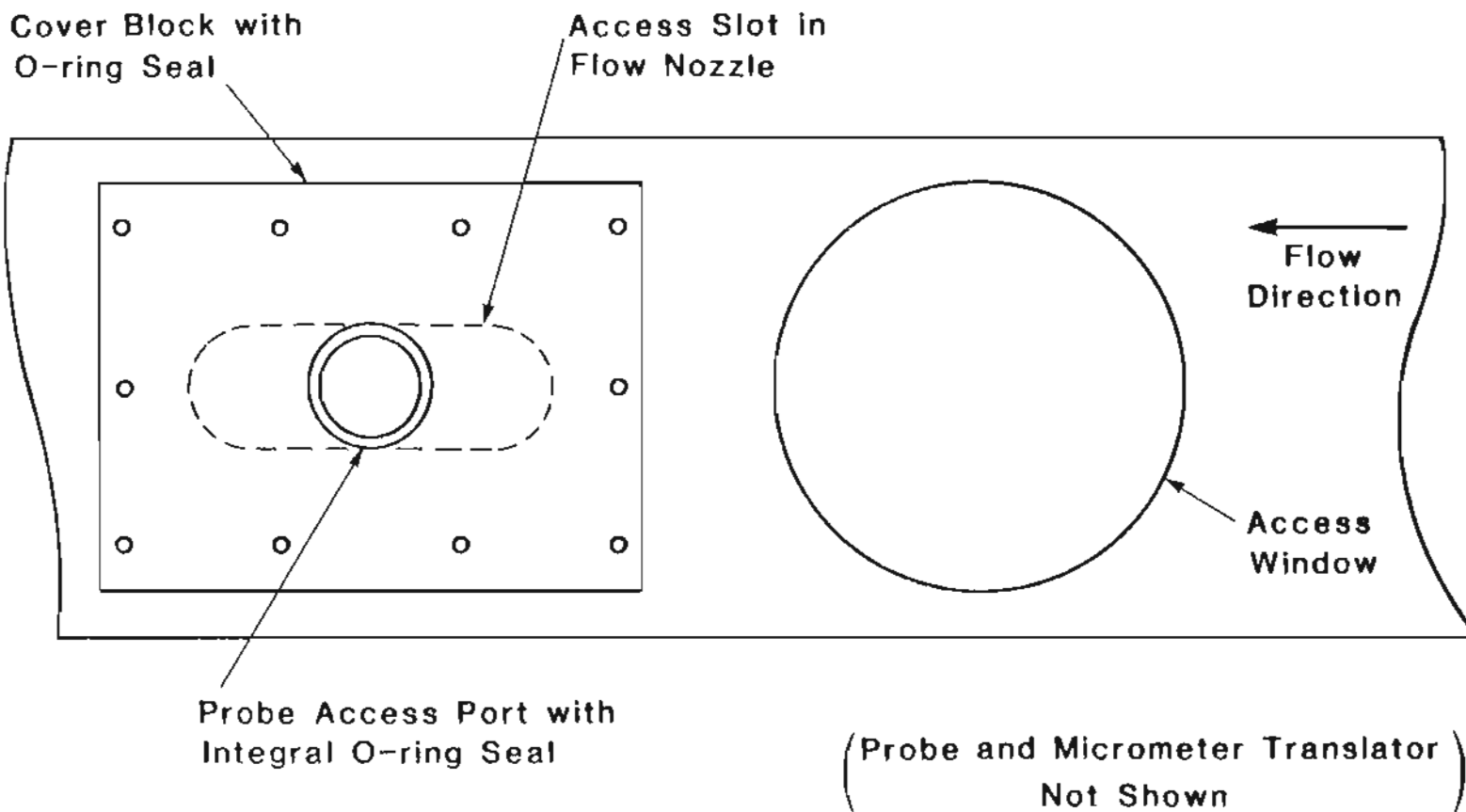


FIGURE 6. Access Port Detail

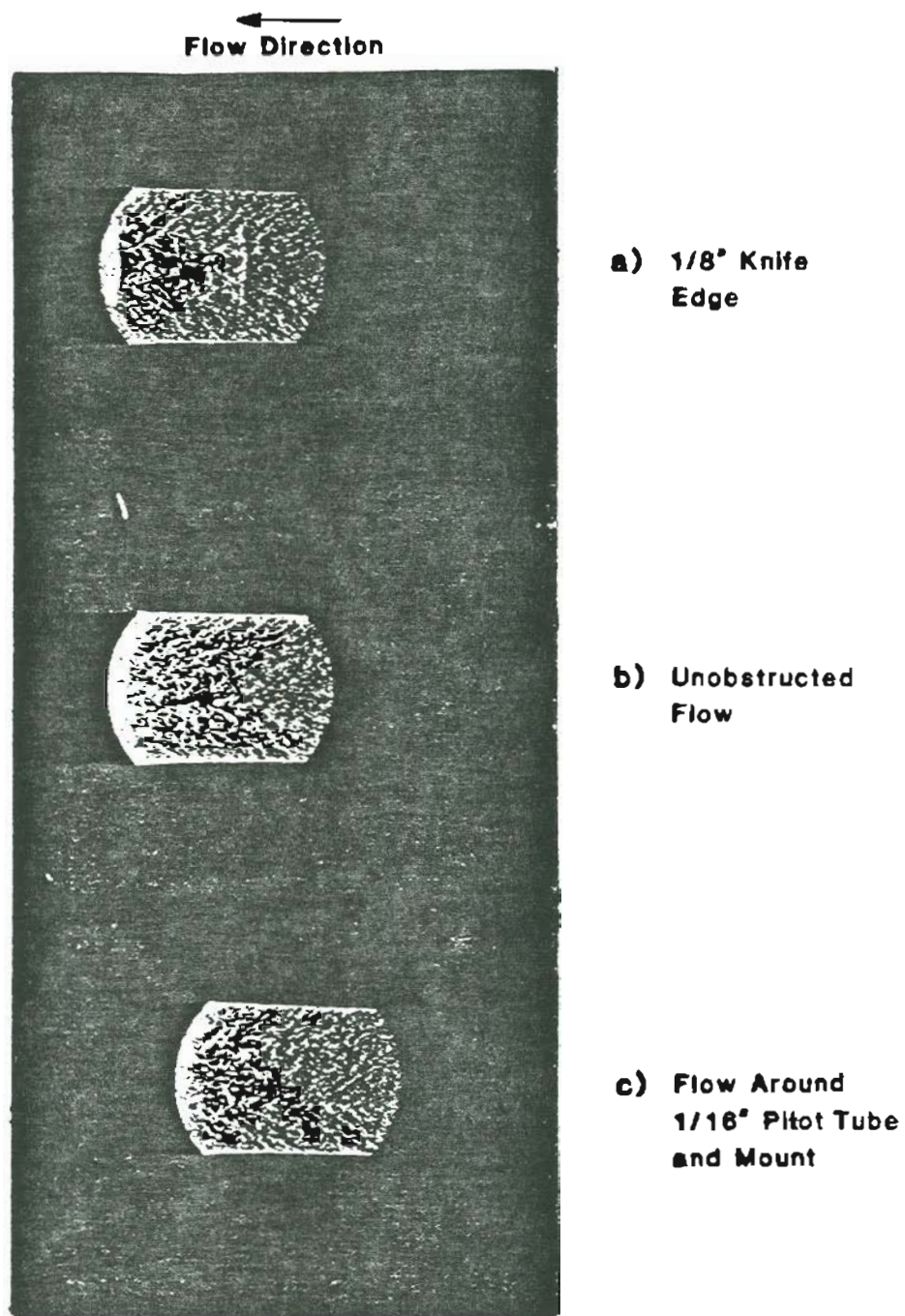


FIGURE 7. Shadowgraphs of the Flow Around the Mounting Hardware

the pressure in the tube. This change in capacitance is, in turn, converted to a fluctuating voltage signal by making the pressure transducer one arm of an external capacitance bridge circuit. In the experiment described here, this voltage signal was scaled using an analog amplification stage (see Figure 5) and then digitized using a Physical Data 515 transient digitizer sampling at a frequency of 200 kHz. The digitized signal was then transferred to an H-P 9830 desktop computer via an HPIB (IEEE 488) parallel interface bus and stored on magnetic tape for further analysis.

(As noted in Chapter II (see Figure 2), the Ludwig tube flow nozzle is operated in a shock tube (pulsed) configuration with each plateau in the resultant pressure curve representing an approximately 50 ms time interval of equilibrium flow. The optimum sample interval is on the first plateau, if for no other reason than signal-to-noise considerations. While this was attempted at first, the hot wire data revealed a very strong, transient starting effect occurring at the beginning of the first plateau and significantly perturbing the equilibrium flow. For this reason, the following results represent measurements taken from intervals in the second plateau which exhibited quite stable equilibrium flow.)

The following very detailed and convenient pitot tube data reduction scheme has been developed and summarized by Mr. Daryl Monson at NASA Ames Research Center and the author is very grateful for the use of this method.⁴⁸ This analysis procedure requires the measurement of the following parameters using both a pitot tube and some additional

instrumentation (see Figure 8):

1. P_{T1} - the pressure upstream of the flow nozzle.
(Measured using a static port coupled to a pressure transducer).
2. T_{T1} - the absolute temperature upstream of the flow nozzle. (Measured using a thermocouple).
3. P_w - the static pressure at the wall in the test section. (Measured using a static port).
4. P_{T2} - the pressure measured by the pitot tube.

The following common assumptions are also employed:

1. $T_T(z) = T_{T1} = \text{Const.}$ Where $T_T(z)$ is the total temperature as a function of displacement at right angles to the wall. The total temperature is the temperature that would exist if the flow could be suddenly brought to a rest isentropically.⁴⁸
2. $P_\infty \approx P_w = \text{Const.}$ Where P_∞ is the free stream pressure that exists at the center (laminar flow) region of the test section.⁴⁸

The local and mean Mach number may be calculated from the Rayleigh

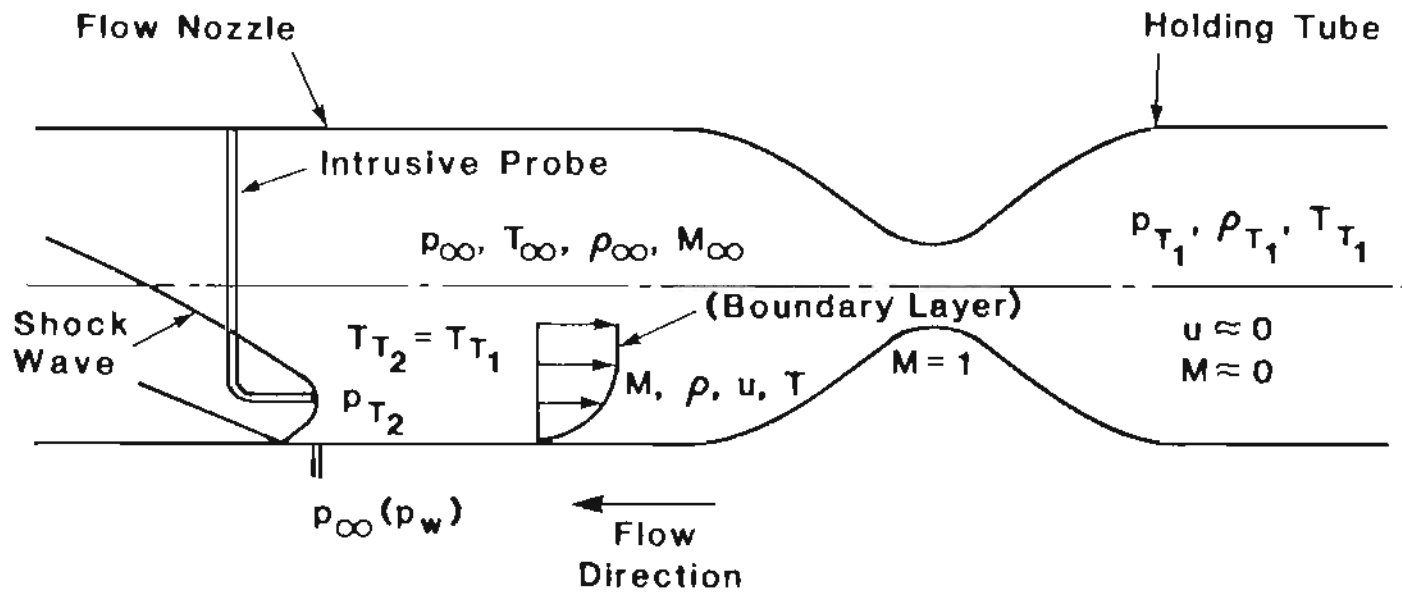


FIGURE 8. Parameters of Interest in the Pitot Tube Experiment

supersonic pitot formula:^{48,49}

$$P_w/P_{T2}(z) = P_\infty/P_{T2}(z) = [(aM^2 - b)^p]/[(cM^2)^q] \quad (1a)$$

Where:

$$a = 2\gamma/(\gamma + 1)$$

$$b = (\gamma - 1)/(\gamma + 1)$$

$$c = (\gamma + 1)/2$$

$$p = 1/(\gamma - 1)$$

$$q = \gamma/(\gamma - 1)$$

$$\gamma = c_p/c_v = 1.4 \text{ for a diatomic gas such as } N_2 \quad (1b)$$

Since Eq. (1a) is transcendental in Mach number (M), it may be solved using appropriate numerical methods or tabulated solutions of the normalized equation.⁴⁹

Using Eq. (1a) and measuring P_{T2} at the centerline of the flow nozzle allows the calculation of the free stream (laminar flow) Mach number (M_∞) which may be compared to the value given by:

$$P_{\infty}/P_{T1} = \{1 + [(\gamma - 1)/2]M_{\infty}^2\}^{\gamma/(\gamma - 1)} \quad (2)$$

to test the consistency of the experimental measurements.

Figure 9 is a plot of the local Mach number (M) plotted as a function of normalized distance away from the wall (y/H), where H is distance from the wall to the centerline). The boundary layer thickness is defined to be the distance away from the wall at which the Mach number has achieved 90% of the free stream value. As noted on Figure 9, this number (δ) is 1.43 cm for this particular flow nozzle.

The local velocity (u), as a function of y/H, may be calculated from:

$$(u/a^*) = \{(\gamma + 1)/[(2/M^2) + \gamma - 1]\} \quad (3a)$$

where a^* is the so called "critical velocity" or the local speed of sound. This quantity may be calculated from:

$$a^{*2} = \gamma RT_{T1} / \{1 + [(\gamma - 1)/2]M^2\} \quad (3b)$$

where R is the ideal gas constant. Once again, the centerline measurement provides the free stream value of the parameter, in this case the velocity (u_{∞}) value. Figure 10 shows a plot of normalized velocity (u/u_{∞}) as a function of normalized transverse position (y/H).

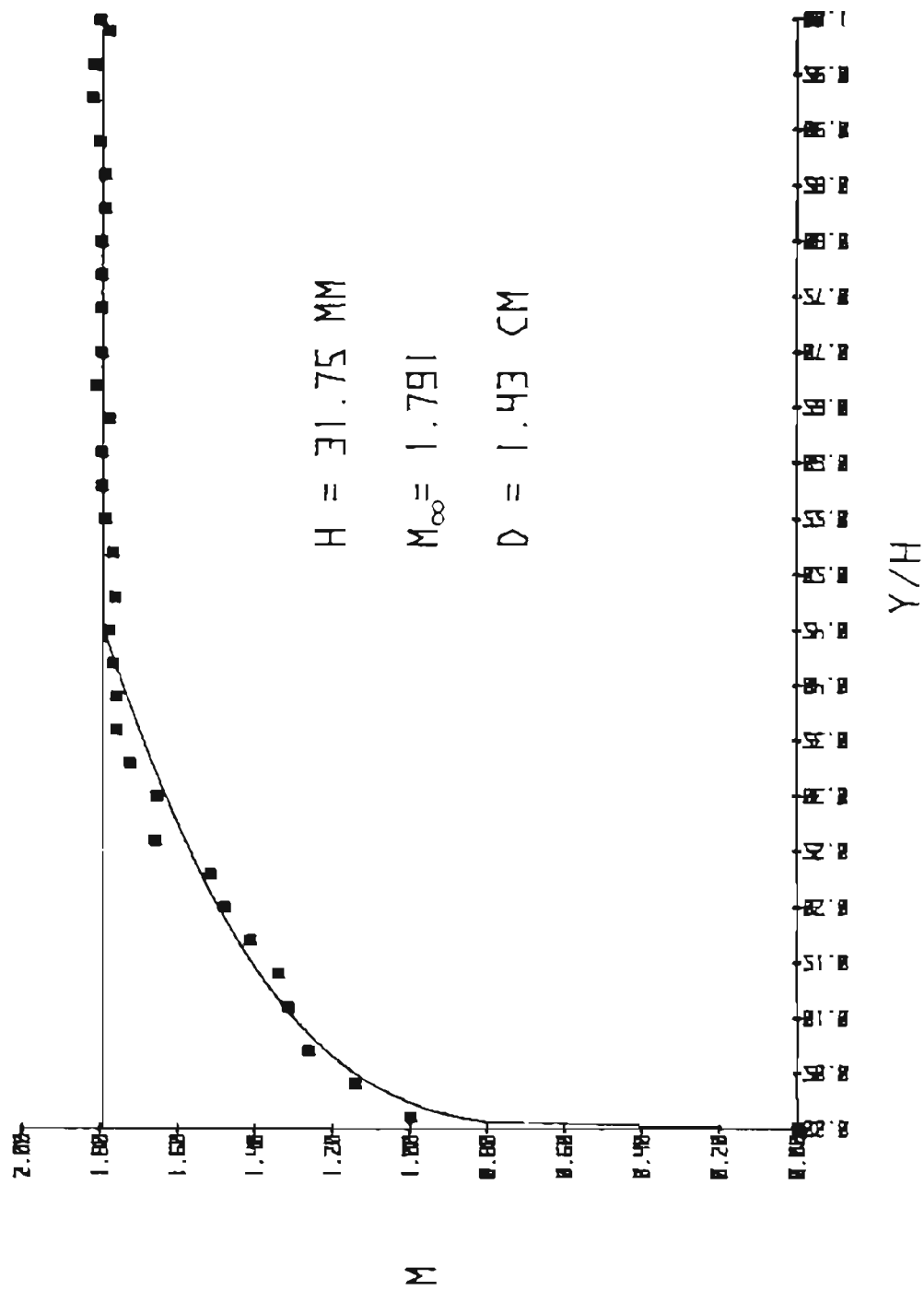


FIGURE 9. Mach Number vs. y/H

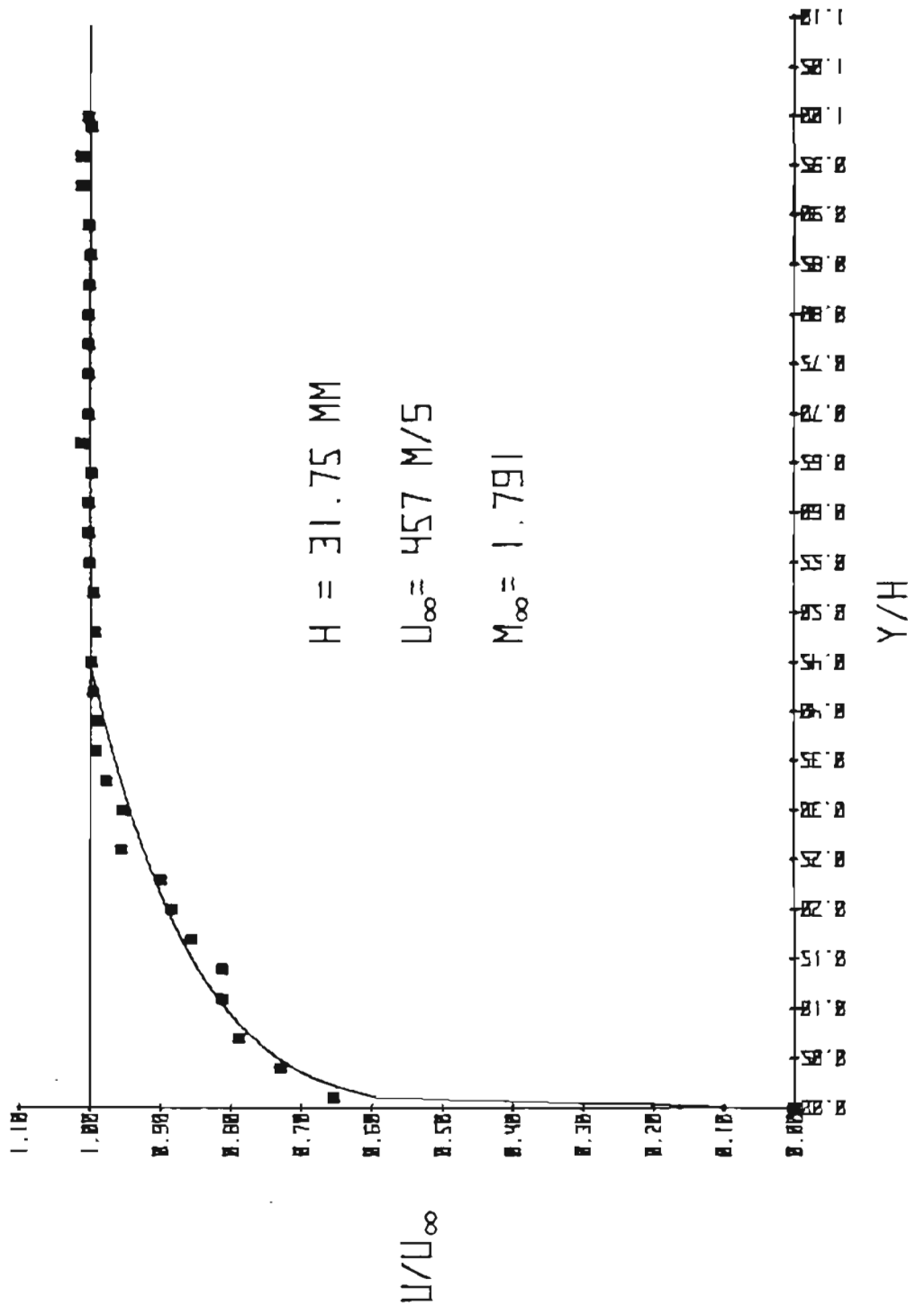


FIGURE 10. Normalized Velocity vs. y/H

Similarly, Figure 11 shows a plot of normalized temperature (T/T_∞) as a function of normalized distance (y/H) computed from:

$$T/T_{T1} = \{1 + [(\gamma - 1)/2]M^2\}^{-1} \quad (4)$$

Lastly, the local normalized density (ρ/ρ_∞) is plotted in Figure 12 as a function of normalized distance (y/H) computed using:

$$\rho/\rho_\infty = p_w T_\infty / P_\infty T \quad (5)$$

Not only do these curves illustrate the average nature of the flow, but they also provide the basic ingredients necessary for the calibration of the hot wire instrument which will be capable of at least limited time-resolved measurements.

C. Analysis and Results of the Measurement of the Ludwig Tube Flow using a Hot Wire Anemometer

As shown in Figure 4, the hot wire anemometer is based on a small heated wire filament placed in the flow path. If an electric current is forced to flow in the filament, the voltage subsequently induced will depend on the resistance of the wire.⁴⁷ This resistance will, in turn, be a function of the instantaneous temperature of the wire. As the turbulent eddies, consisting of perturbations in density, temperature and velocity, are convected past the heated filament by the mean

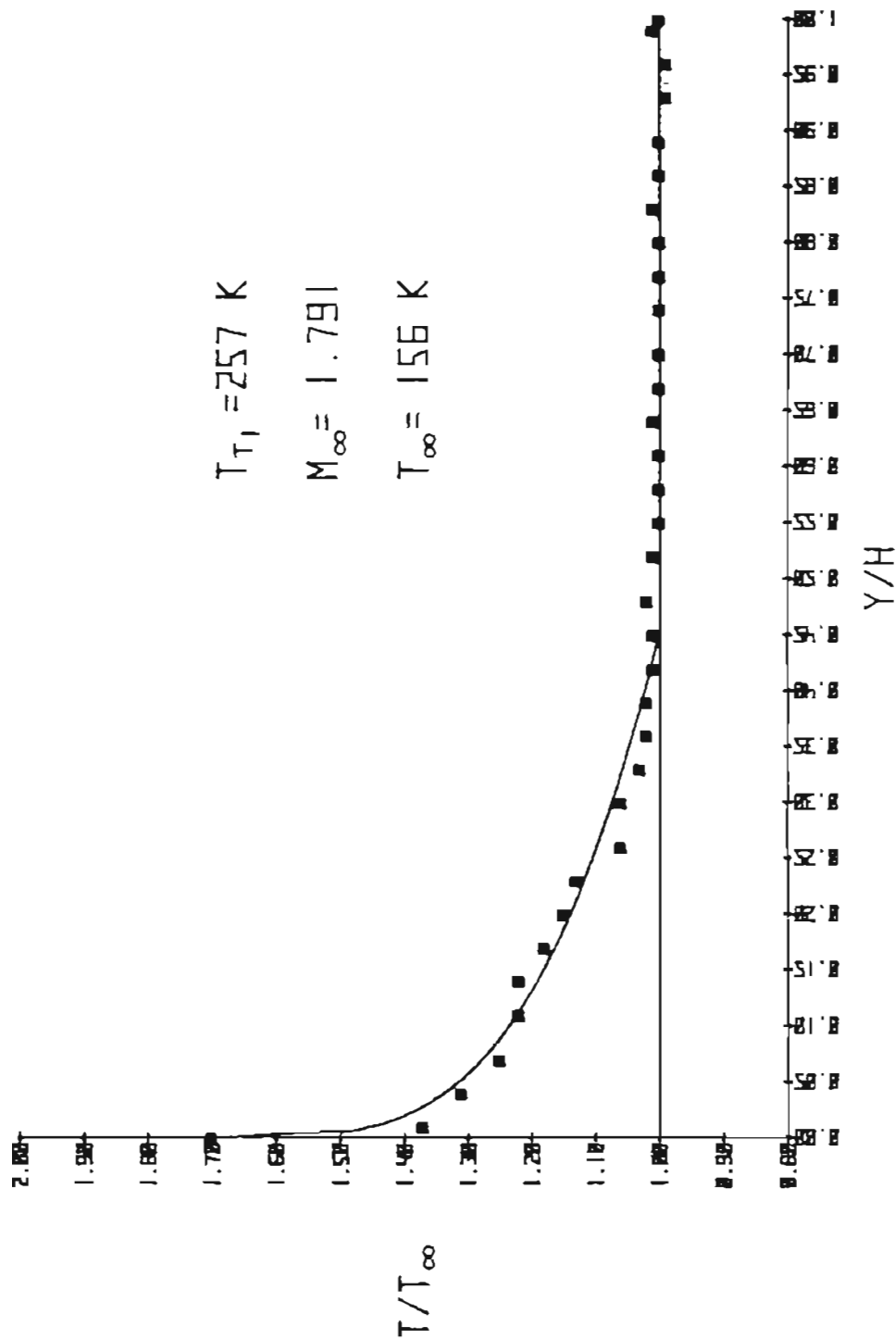


FIGURE 11. Normalized Temperature vs. y/H

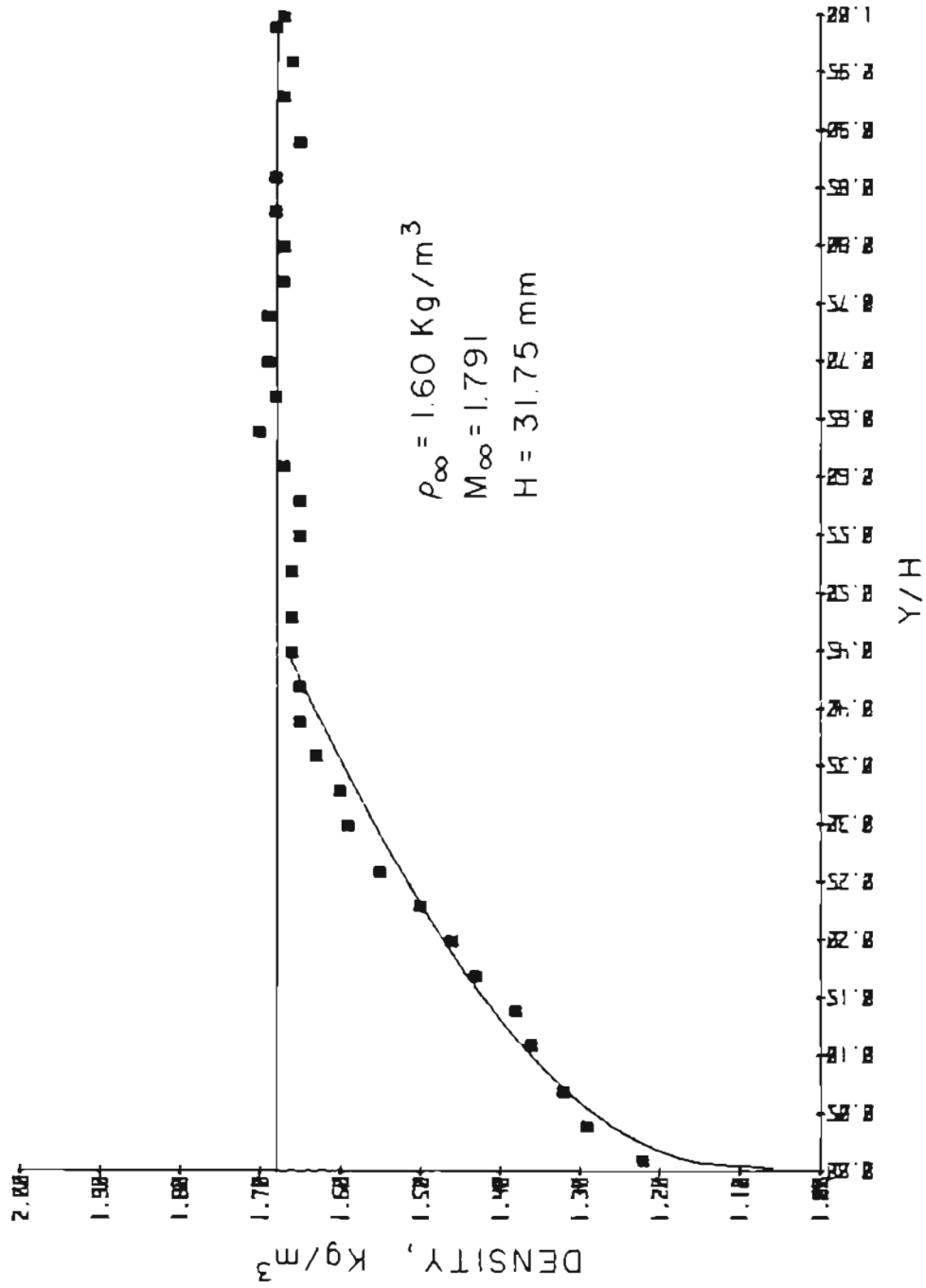


FIGURE 12. Normalized Density vs. y/H

velocity of the flow, heat energy will be either gained or lost by the wire altering its thermal state and thus inducing a slight, time dependent perturbation of the resistance.⁴⁷ This perturbation will be manifested as a fluctuation in the voltage drop across the wire and can be easily detected, with a good signal-to-noise ratio, by means of an A.C. bridge circuit.^{47,50-54} With the proper analysis of the hot wire dynamic response and appropriate data reduction techniques, it is possible to measure the turbulence parameters of interest.

Several authors have treated the theoretical dynamic response of a hot wire anemometer in detail.^{41-47,50-54} It is quite apparent that this instrument is sensitive to many fluctuations and processes in the turbulent working fluid and thus a completely theoretical analysis of the hot wire response is very complicated and so qualified as to be of limited practical use.⁴⁷ It is most productive to use a simplified dynamic analysis in conjunction with a calibration technique based on the averaged data provided by pitot tube measurements.

In general, the fluctuating signal (e') may be written in the following convenient form:⁵⁰⁻⁵⁴

$$e'/\bar{e} = S_u(u'/\bar{u}) + S_\rho(\rho'/\bar{\rho}) + S_{T_t}(T'_t/\bar{T}_t) \quad (6)$$

where u denotes flow velocity, ρ denotes density and T_t denotes total temperature. The bar (-) denotes time averaging and the prime symbol (') denotes fluctuating quantities. S represents the response

sensitivity to a specific variable and is defined as:

$$S_u = (\partial \ln e) / (\partial \ln u), \text{ holding } \rho, T_t \text{ and } R_w \text{ constant.} \quad (7a)$$

$$S_\rho = (\partial \ln e) / (\partial \ln \rho), \text{ holding } u, T_t \text{ and } R_w \text{ constant.} \quad (7b)$$

$$S_{T_t} = (\partial \ln e) / (\partial \ln T_t), \text{ holding } u, \rho \text{ and } R_w \text{ constant.} \quad (7c)$$

(R_w denotes wire resistance.)⁵⁰

For compressible flows in excess of Mach 1.2, it is possible to simplify Eq. (6) to:^{47,50,53,54}

$$e'/\bar{e} = S_{\rho u} [(\rho u)' / \overline{\rho u}] + S_{T_t} (T'_t / \bar{T}_t) \quad (8)$$

where the product (ρu) is known as the mass flux of the flow. The wire overheat ratio (a_w) is defined as:

$$a_w \cong (R_w - R_r) / R_r \quad (9)$$

where R_w represents the resistance of the heated wire and R_r represents the resistance of the wire at ambient or room temperature. At fairly high overheat ratios ($a_w > 0.8$), the total temperature sensitivity (S_{T_t})

becomes small and the total temperature fluctuations (T'_t) are small in the case of adiabatic flow.⁵⁰ It is thus possible to neglect the total temperature term in Eq. (9) and write the mass flow as a direct proportionality to the normalized hot wire signal. Taking the R.M.S. average (denoted by brackets ($\langle \rangle$)) of both sides of the resulting relationship yields:

$$\langle (\rho u)' \rangle / \bar{\rho u} = (1/S_{\rho u}) (\langle e' \rangle / \bar{e}) \quad (10)$$

Two fundamental approximations allow the further reduction of Eq. (10).^{41-47, 50-54} As noted above, the total temperature fluctuations (T'_t) may be neglected if sufficiently high overheat ratio is employed. Several authors have indicated that pressure fluctuations (P') are also small enough to be neglected in this application without serious loss of accuracy.⁵⁰⁻⁵⁴ (Numerical estimates of the probable error introduced by this approximation will be presented later in this chapter.) Under these assumptions, it is possible to write the normalized static temperature fluctuations in terms of the normalized velocity fluctuations.

$$T'/\bar{T} = -(\gamma - 1) M^2 (u'/\bar{u}) \quad (11)$$

The following expressions may then be derived using Eq. (10) as a

starting point:

$$\langle u' \rangle / \bar{u} = (1/A) \langle \langle \rho u \rangle' \rangle / \bar{\rho u} \quad (12)$$

$$\langle \rho' \rangle / \bar{\rho} = [(A - 1)/A] \langle \langle \rho u \rangle' \rangle / \bar{\rho u} \quad (13)$$

$$\langle T' \rangle / \bar{T} = [(1 - A)/A] \langle \langle \rho u \rangle' \rangle / \bar{\rho u} \quad (14)$$

where:

$$A \equiv 1 + (\gamma - 1)M^2 \quad (15)$$

For this application, A will be less than or on the order of 2.3. The maximum error introduced by the neglect of pressure fluctuations will be on the order of $|\langle P' \rangle / P|$.^{41,50-52} Preliminary measurements of a similar Ludwig tube flow using laser-induced fluorescence techniques (LIF), see chapter I) indicate this quantity to be on the order of 2-3%, which is quite acceptable error for the purposes of this measurement.⁵⁵

A schematic representation of the experiment is shown in figure 5. The hot wire probe shown in Figure 4 was inserted into the Ludwig tube flow via the access port shown in Figure 6 and positioned in the window region of the test section. The probe was scanned at right angles to the wall by means of a micrometer-driven translation stage.

The raw signal from the hot wire probe was input to one arm of a commercial A.C. bridge analyzer. The bridge output was scaled to TTL

levels using an analog pre-amplifier and then input to a Physical Data 515 transient digitizer. The bridge signal was then digitized at a sampling rate of 200 kHz. The digital data was then transferred to an H. P. 9830 computer via an HPIB (IEEE 488) interface bus and stored on magnetic tape for further analysis. A Prime 350 computer was later used for more complex and detailed data reduction, including fast Fourier transform (FFT) analysis.

An oscilloscope photo of a typical run response is shown in Figure 13. Note the severe oscillatory anomaly occurring on the first plateau of the shock tube operation. This transient effect made it impossible to use data generated during approximately the first 50 ms of the run. As noted previously, all experimental data was recorded during the second plateau of the shock tube operation. A typical digitized raw data set, taken on the second plateau, is shown in Figure 14.

The hot wire anemometer was calibrated using the pitot tube data. Two methods of calibration are in common use. The first method requires averaged pitot tube measurements of the density (ρ) and the flow velocity (u) taken on the centerline. By varying the load pressure of the N_2 working fluid (the pressure in the holding tube, see chapter 2, just before the firing valve is opened), it is possible to vary the mass flux (ρu product). If the averaged hot wire response is then measured on the centerline for the same load pressure values, a calibrated response curve ($\ln[e]_{av}$ versus $\ln[(\rho u)_{av}]$) may be drawn. A second method involves a "dynamic" calibration technique requiring averaged mass flux data from pitot tube measurements taken at various points in

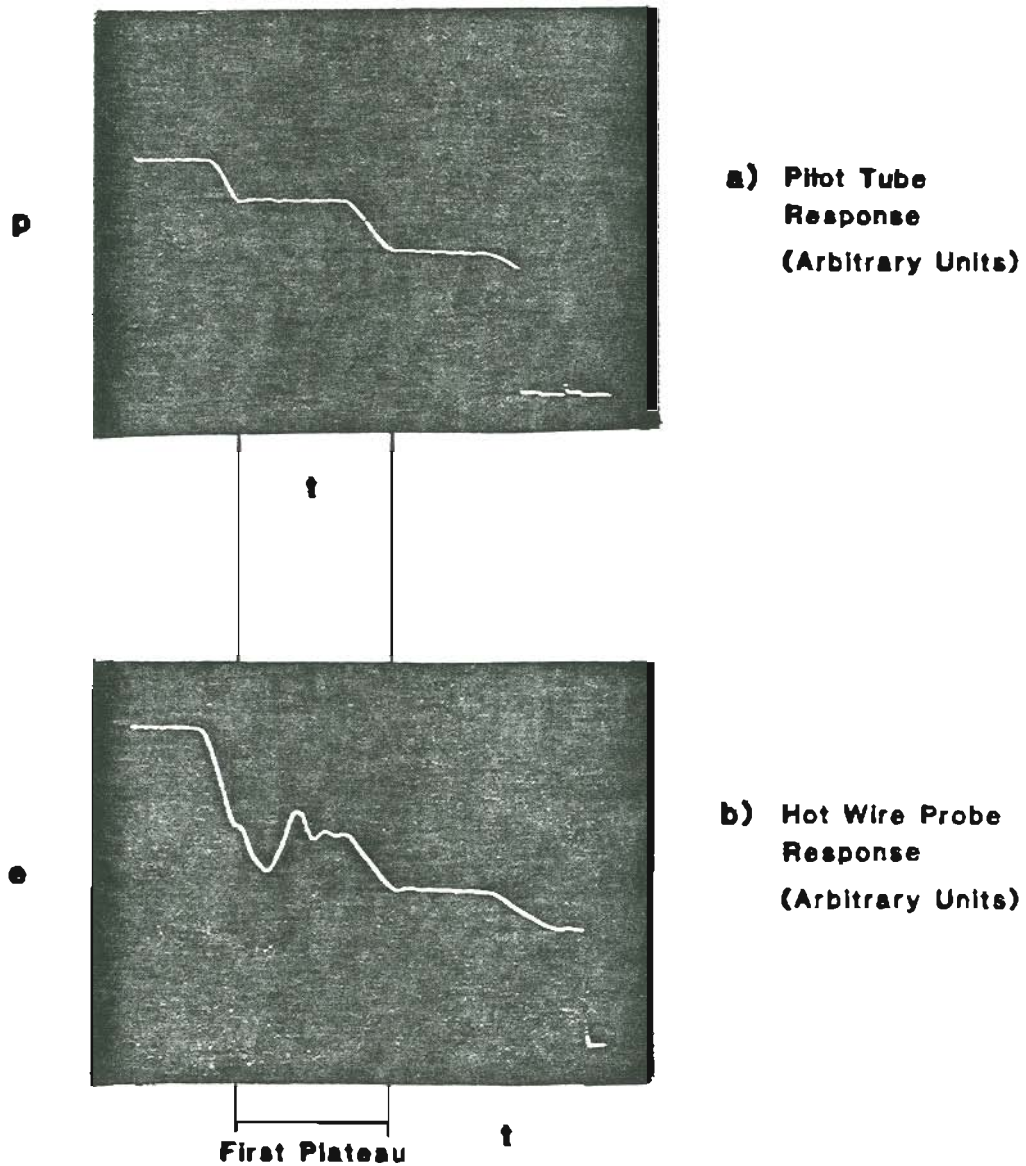


FIGURE 13. Comparison of Hot Wire and Pitot Tube Signals

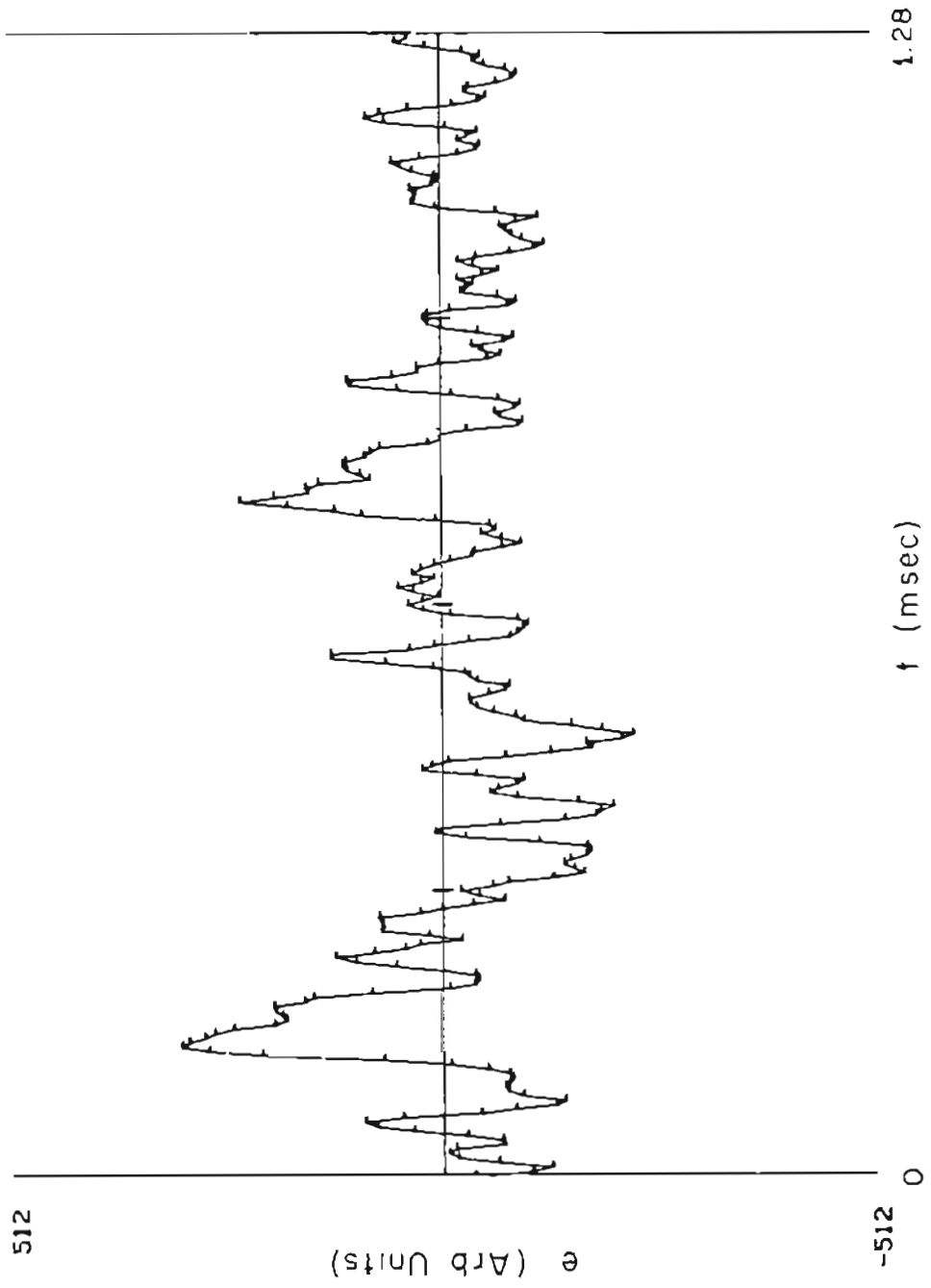


FIGURE 14. Typical Hot Wire Data

the turbulent boundary layer. If the hot wire response is then measured at the same points in the boundary layer, a similar calibrated response curve to the one resultant from the first method may be plotted. While in theory these two methods should yield equivalent response curves, it became apparent quite early that such was not the case.

The first, or "centerline" method, results in mass flux numbers much higher than any comparative measurement could detect, while the dynamic method agreed quite well with other related work in a similar flow. This prompted a great deal of discussion and work in an attempt to explain this phenomenon with mixed results. It is beyond the scope of this work to attempt to address this problem in detail, but suffice it to say that the consensus among respected researchers in the field of fluid dynamics is that the dynamic method is the much more accurate and representative calibration technique. The centerline method simply does not see the perturbational processes that are dominant in the turbulent boundary layer. Indeed, the dynamic method provided the first confirmation of the LIF measurements (taken in a very similar test section at essentially identical Mach number) which had been plaguing several workers for an extended period of time. The dynamic calibration technique was also confirmed by the optical data taken in this work and presented in later chapters. Figure 15 shows the dynamic calibration curve measured in the Ludwig tube test section.

The RMS perturbation in mass flux versus normalized transverse displacement relative to the wall is plotted in Figure 16. This curve demonstrates the classic "flat plate" boundary layer structure with the

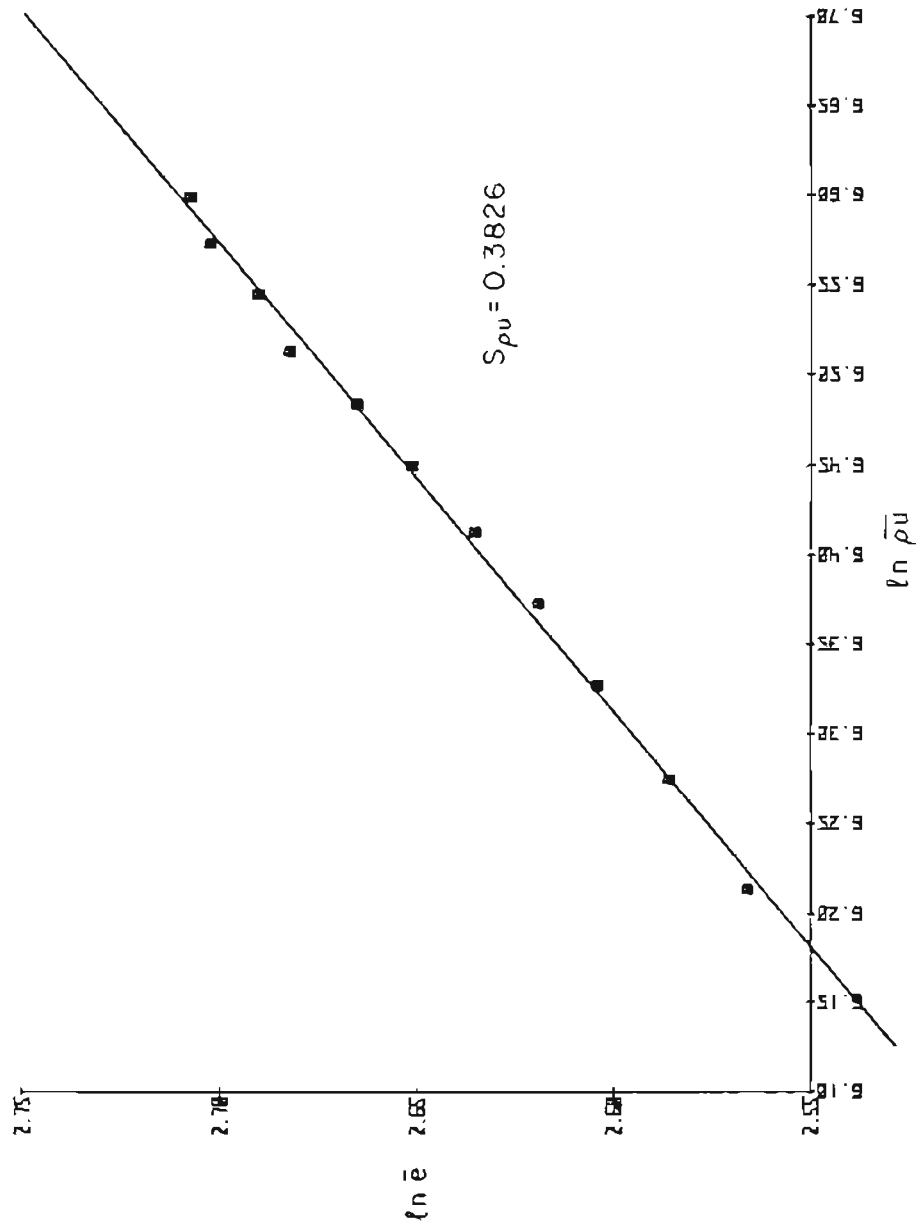


FIGURE 15. Hot Wire Calibration Curve

maximum mass flux perturbation being about 9.5%. The symbol delta (δ) represents the boundary layer thickness (1.43 cm in this case). The raw hot wire data was also subjected to intensive Fourier analysis which will be presented in a following chapter.

Figure 17 shows the RMS density fluctuations as a function of position and Figure 18 shows a comparison of RMS temperature fluctuations compared to those values measured using LIF in an essentially identical flow nozzle operated at Mach 2.05 in a closed expansion or "blow down" mode.

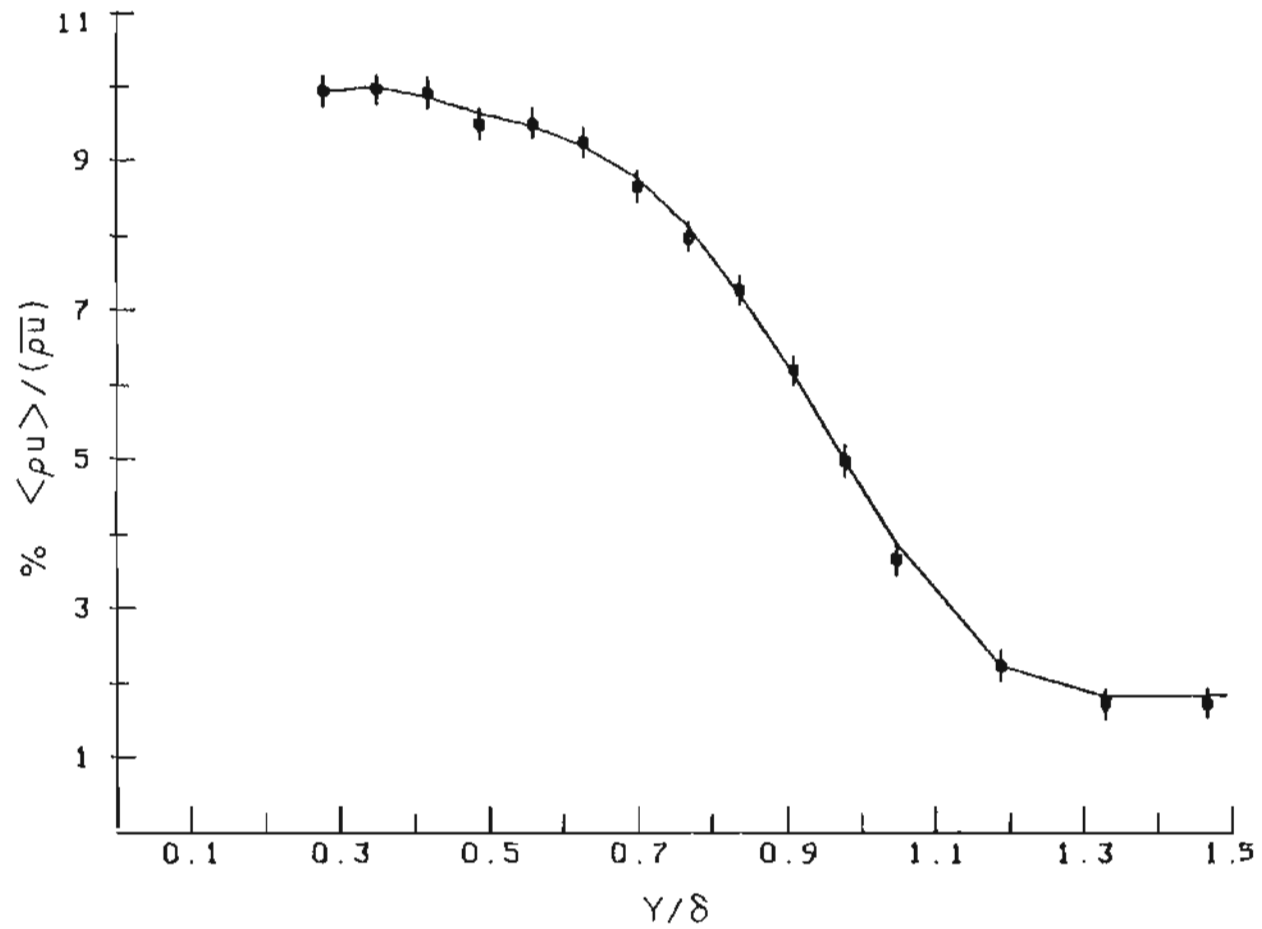


FIGURE 16. RMS Mass Flow Fluctuations vs. y/δ

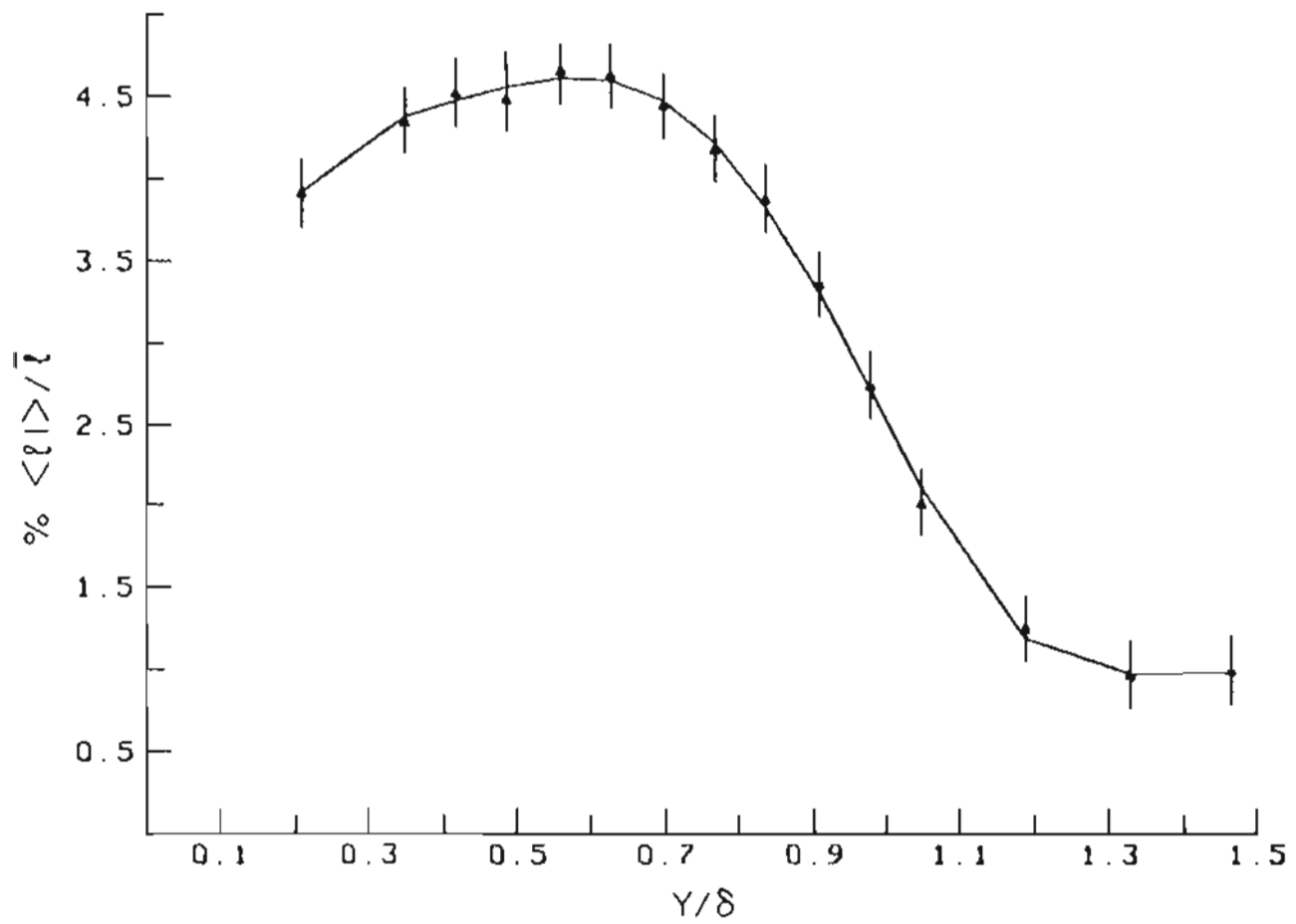


FIGURE 17. RMS Density Fluctuations vs. y/δ

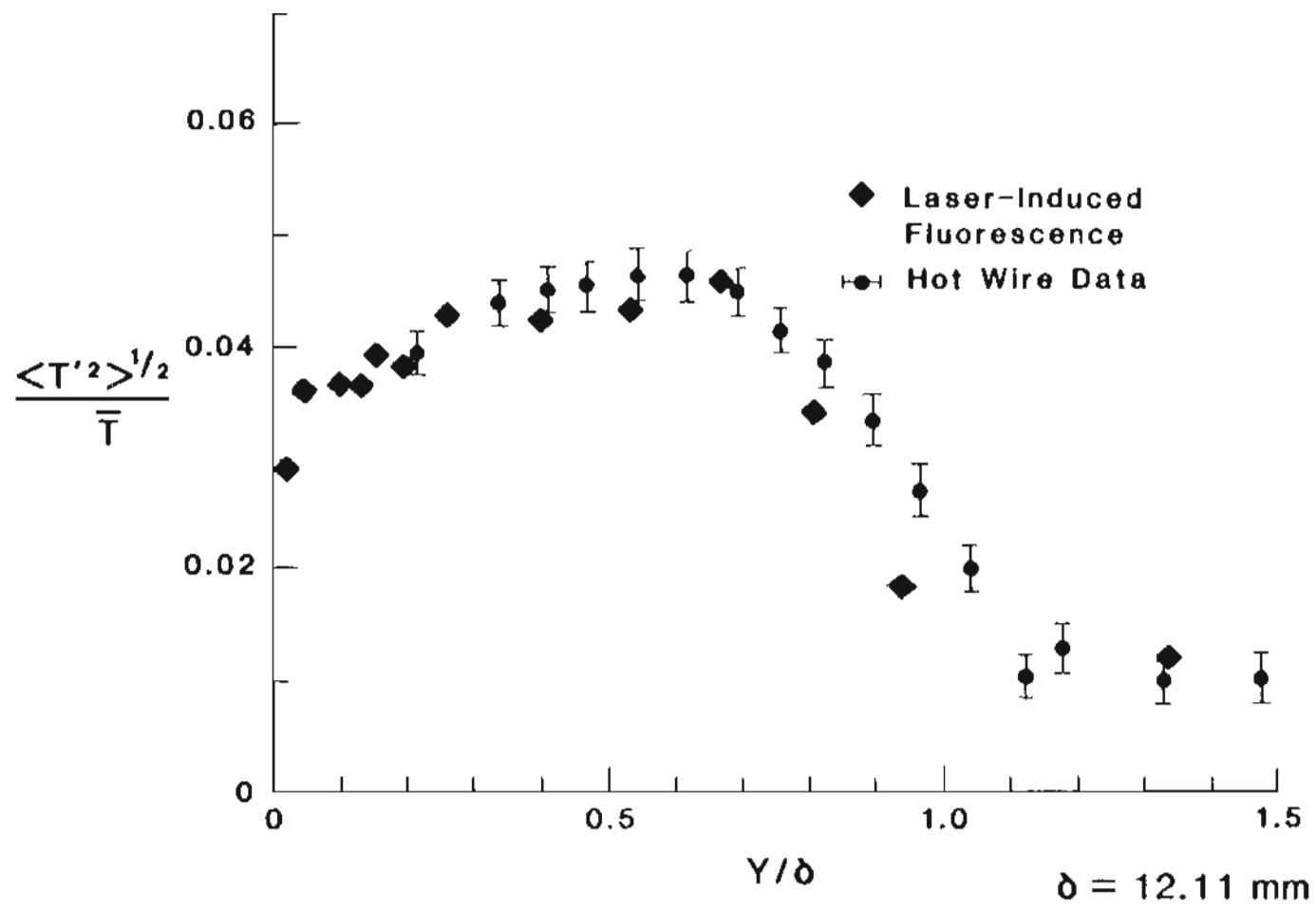


FIGURE 18. Comparison of Hot Wire Data with LIF Data

CHAPTER V

THE DESIGN OF A SINGLE BEAM EXPERIMENT TO TEST THE APPLICABILITY OF THE
EXTENDED HUYGENS-FRESNEL THEORY TO THE CASE OF SUPERSONIC FLOWA. Introduction

The calculations of Chapter III provide several possible approaches to the design of an experiment capable of testing the validity of the extended Huygens-Fresnel theory in modeling the turbulent field produced in a supersonic, bounded flow. The most desirable experimental approach was one involving the use of a visible, low power ($< 10\text{mW}$), TEM_{00} Gaussian laser beam in a manner that is insensitive to mechanical perturbations, such as mount vibration or acoustic noise coupling effects, and also capable of providing low noise data in the rather dirty environment of the typical laboratory wind tunnel. Several practical considerations were also placed on the design of such an experiment, the most important of which was the use of existing data acquisition and analysis equipment (described in detail in Chapters II and VI).

Bearing in mind all of these considerations, the most straightforward method of testing the extended Huygens-Fresnel theory in a supersonic environment consists of measuring the effects of the turbulent field on a single TEM_{00} laser beam propagating through the

field. Since these effects consist primarily of phase perturbations of the optical wavefront, and not energy attenuation, it is possible to design high speed optical and measurement systems based around a low power He-Ne laser beam and existing NASA electronics.^{20,24,56}

It is possible to develop an intuitive picture of the effects induced on the beam in a turbulent field by considering two extreme cases. If a laser beam is expanded to a diameter which is large when compared with the smallest turbulent eddy size, l_0 (see Chapter III for further details), the interaction of the beam with the eddies in the turbulent field will produce a distorted, but relatively undeflected, far field spot (see Figure 19). If, on the other hand, the beam is focused so that it is small when compared to the minimum eddy size, then the dominant effect of the beam-turbulence interaction will be to induce a fairly uniform tilt in the entire optical phase front and hence cause a deflection of the beam while leaving the far field spot relatively circular and unperturbed (see Figure 19).²⁰ While measurement of a distorted (or phase scrambled) wave front will typically require the use of interferometric techniques requiring rather sophisticated and noise sensitive equipment, many quite simple methods exist (as shall be discussed shortly) for the measurement of beam deflection or wander. The simplicity of experimental design, in conjunction with the development of a closed form model of the situation using the extended Huygens-Fresnel theory, made the beam deflection experiment most desirable.

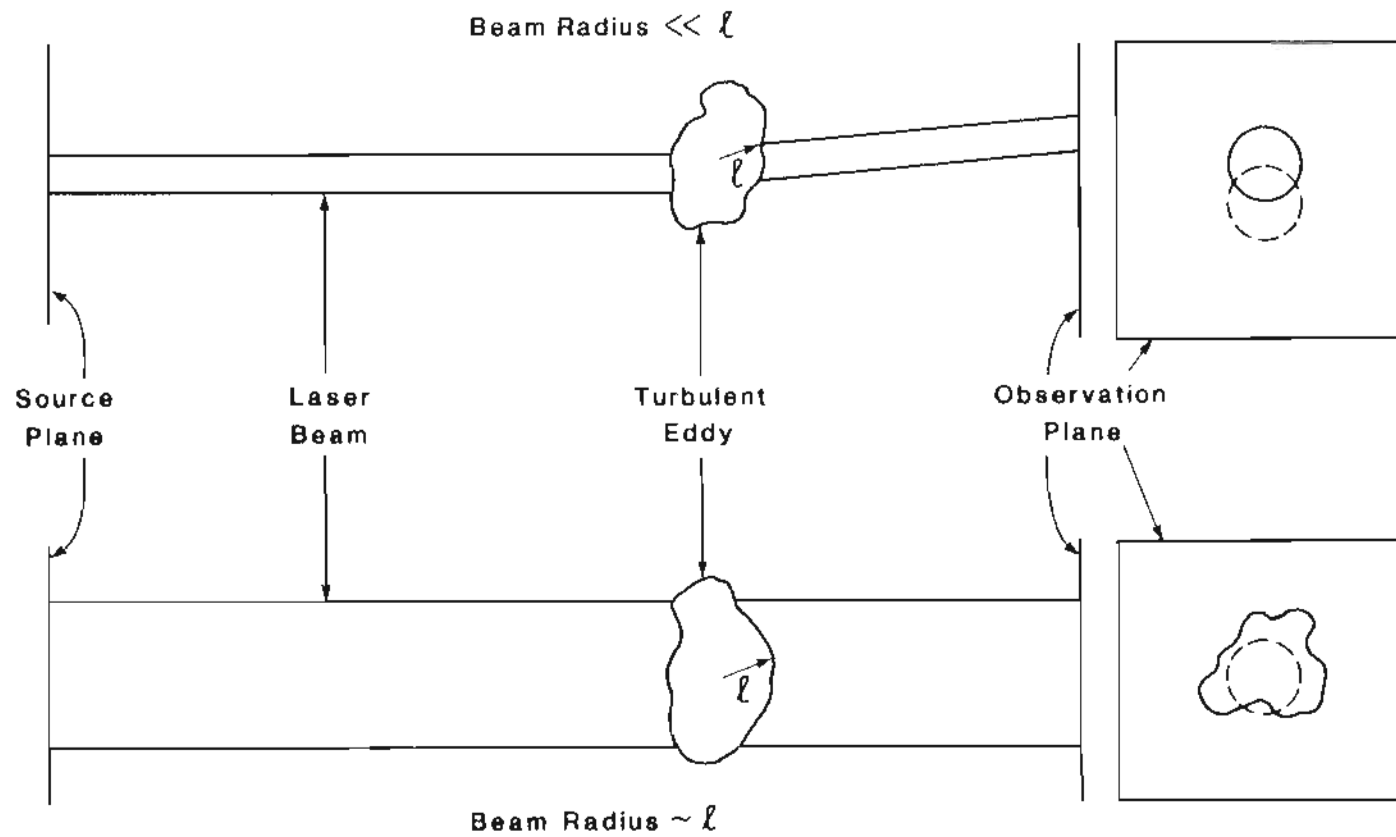


FIGURE 19. The Effect of Beam Size on the Far Field Spot

B. The Calculation of the Refractive Index Spectrum and the Structure "Constant" from the Hot Wire/Pitot Tube Measurements

Section C of Chapter III presents a detailed calculation of the mean output irradiance (or intensity) of a laser beam propagating in an idealized approximation to the turbulent field existing in NASA's Ludwig tube facility. (See Eq. (52) in Chapter III.) Using the results of the hot wire/pitot tube measurements reported in Chapter IV, it is possible to employ the extended Huygens-Fresnel theory to model the output intensity of a laser beam propagating in the real-world turbulent field. The two functions of prime interest in the determination of this model are the spectrum ($\Phi_n^0[\kappa]$) of the refractive index covariance function (B_n) and the structure "constant" (C_n^2), a function of position in this case. The measurement of time-resolved density fluctuations, using the previously described methods of hot wire/pitot tube anemometry, allows the calculation of these two prime functions by employing the proper data reduction techniques.

As shown in Chapter IV, the response of a hot wire anemometer (for Mach numbers greater than 1.2 and for high wire overheat ratios) may be written in the form:⁴⁸

$$e'/\bar{e} = S_{\rho u} \{ (\rho u)' / \overline{\rho u} \} \quad (1)$$

where:

e denotes the voltage signal from the hot wire anemometer.

ρ denotes the density of the working fluid.

u denotes the velocity of the working fluid.

S is a proportionality constant (see Chapter IV).

' denotes local fluctuating quantities.

$\bar{\quad}$ denotes local time-averaged quantities.

It has also been shown (see Chapter IV) that, neglecting pressure fluctuations:

$$(\rho u)' / \overline{\rho u} \propto \rho' / \bar{\rho} \quad (2)$$

The turbulence induced perturbation in the index of refraction (n_1) of the working fluid may be related directly to the normalized density fluctuations (the right-hand side of Eq. (2)) by the Gladstone-Dale relation.⁵⁷ Thus a knowledge of the local normalized density fluctuations allows the calculation of $n_1(r)$ and B_n and hence the determination of the desired function $C_n^2(\kappa)$. Figure 20 shows a schematic representation of the data reduction necessary to calculate the form of $C_n^2(\kappa)$ from raw density data measured from the anemometer.

Referring to Figure 20, it is possible to generate a plot of the refractive index perturbation (n_1) as a function of time from the normalized local density measurements of the hot wire anemometer. It is further possible to scale the time axis of this plot such that length-scale information is presented. This is done by multiplying the time axis by the mean local velocity of the working fluid at the position of the hot wire probe. This data is available from the pitot tube

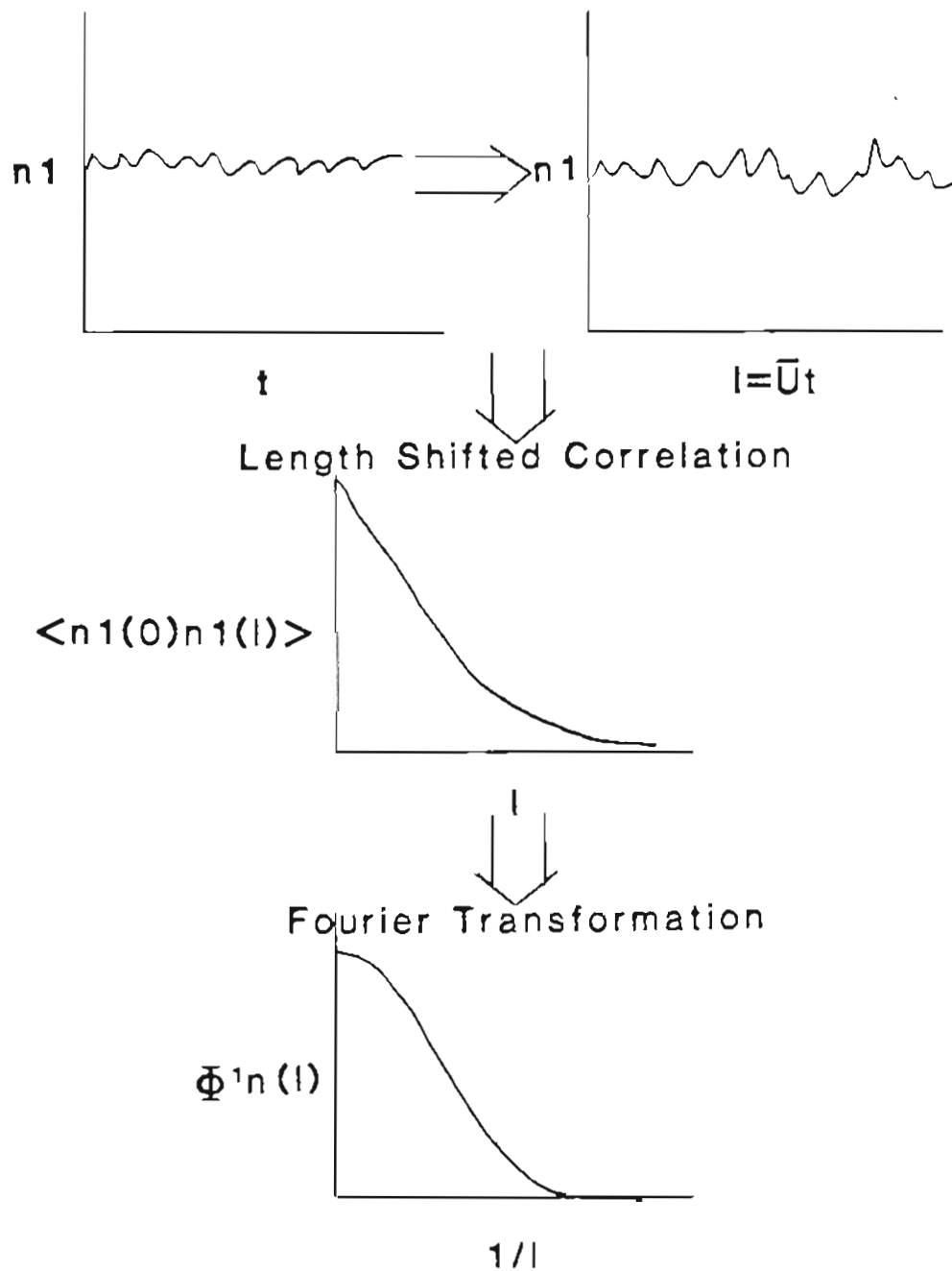


FIGURE 20. Hot Wire Data Reduction

measurements. Assuming that Taylor's frozen flow hypothesis is valid for the case of the Ludwieg tube flow and, hence, turbulent eddies are neither created or destroyed over the temporal span of the measurement, the one-dimensional refractive index covariance function (B_n) may be determined by performing length-shifted correlation (the spatial analog of time-delayed correlation in temporal Fourier analysis) on the n_1 versus l data. The Fourier transform of the covariance function B_n (which is $\langle n_1(0)n_1(l) \rangle$ by definition) versus l data may now be employed to determine the spectrum of the refractive index fluctuations.

A typical result of this data reduction procedure is the spatial spectrum of the refractive index fluctuations as shown in Figure 21 ($y/\delta = 0.5$). The well-defined high frequency peaks readily apparent in Figure 21 are due to standing and traveling shock waves produced by surface irregularities in the Ludwieg tube and may be neglected for the purposes of this calculation.

It is a reasonable a priori assumption that the modified von Karman spectrum (see Chapters I and III) should provide an adequate description of the spectrum of the refractive index covariance function.^{20,24,56}

The modified von Karman spectrum is given by:⁵⁸

$$\Phi_n^0(\kappa) = (\text{Exp}[-\kappa^2/\kappa_m^2]) / (\kappa^2 + \kappa_0^2)^{11/6} \quad (3)$$

where:

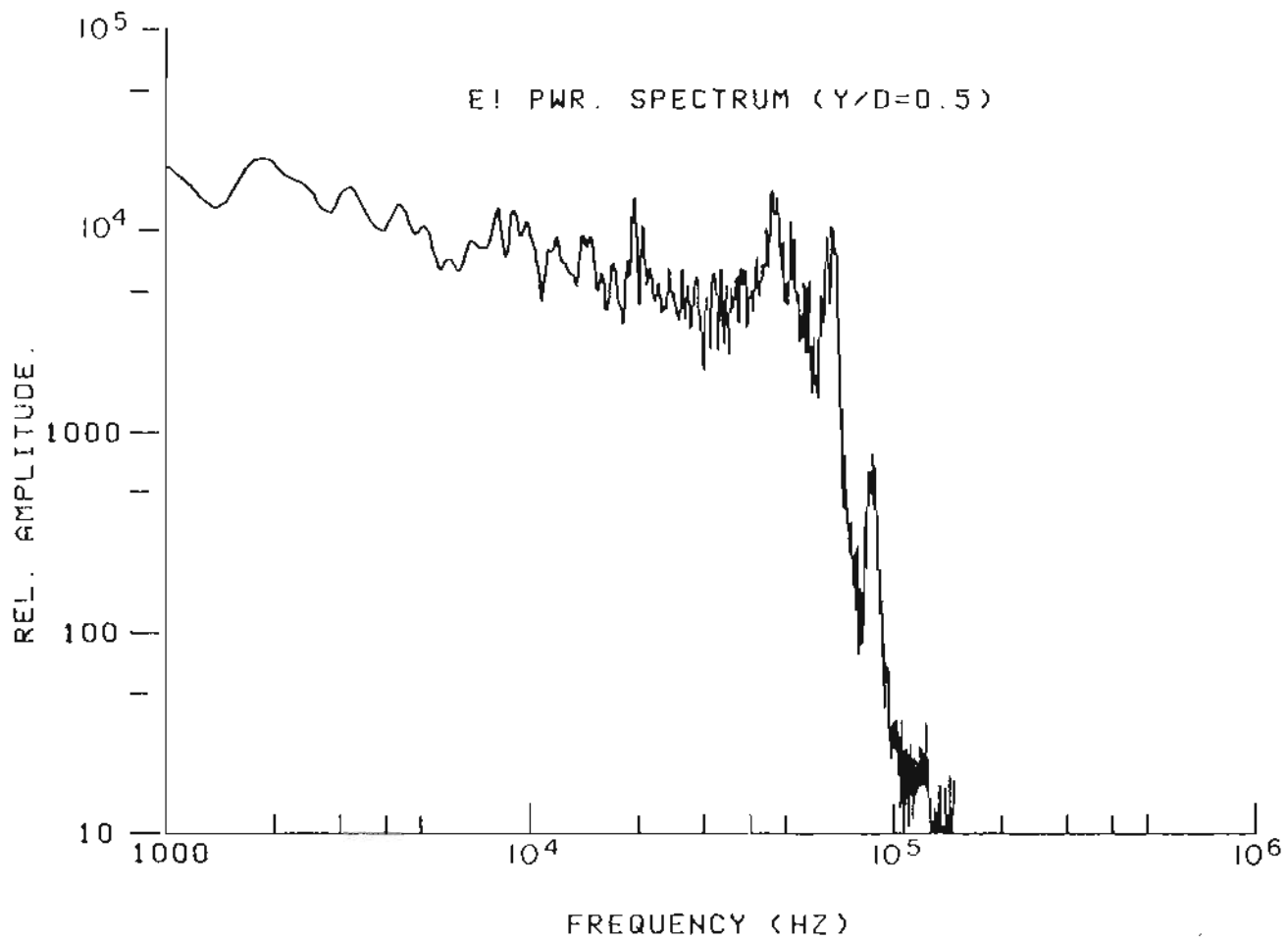


FIGURE 21. Typical Power Spectrum of the Hot Wire Data

$$\kappa_0 \equiv 2\pi/L_0 \quad (4a)$$

$$\kappa_m = 2\pi/l_0 \quad (4b)$$

The turbulence parameters κ_m and κ_0 may be estimated by noting that the outer, or largest, turbulence scale length (L_0) can be no larger than the boundary layer thickness (δ) and that the inner, or smallest, turbulence scale length will be on the order of 1/100 the outer scale length (if the turbulence in the wind tunnel scales in approximately the same fashion as atmospheric turbulence).^{20,56} For the case of NASA's Ludwig flow nozzle, $\delta \sim 1.5$ cm and thus:

$$\kappa_m \sim 10^4 \text{ m}^{-1} \quad (5a)$$

$$\kappa_0 \sim 400 \text{ m}^{-1} \quad (5b)$$

Since $\kappa_m \gg \kappa_0$, it is possible to approximate the von Karman spectrum as:

$$\Phi_n^0(\kappa) \approx (\kappa^2 + \kappa_0^2)^{-11/6} \quad (6)$$

In order to compare this three-dimensional spectrum to the one-dimensional information provided by the reduction of the hot wire

data, it will be necessary to find an expression for the one-dimensional spectrum (${}_1\phi_n^0$) in terms of the three-dimensional spectrum (ϕ_n^0). Tatarskii has shown that:²⁵

$$\phi_n = (-1/2\pi\kappa) \cdot d[{}_1\phi_n^0]/d\kappa \quad (7)$$

Thus, solving Eq. (8) for ${}_1\phi_n^0$ yields:

$${}_1\phi_n^0 = -2\pi \int d\kappa \kappa \phi_n^0(\kappa) \quad (8)$$

Substituting Eq. (6) into Eq. (8) and using methods from elementary calculus gives:

$${}_1\phi_n^0 = (6/5)\pi(\kappa^2 + \kappa_0^2)^{-5/6} + C \quad (9a)$$

Since as $\kappa \rightarrow \infty$, ϕ_n^0 and ${}_1\phi_n^0 \rightarrow 0$; C must be zero. Therefore Eq. (9a) becomes:

$${}_1\phi_n^0 = (6/5)\pi(\kappa^2 + \kappa_0^2)^{-5/6} \quad (9b)$$

A comparison of the one-dimensional modified von Karman spectrum with the data measured by the hot wire anemometer is shown in Figure 22. Note that the fit is quite good except for the previously noted and

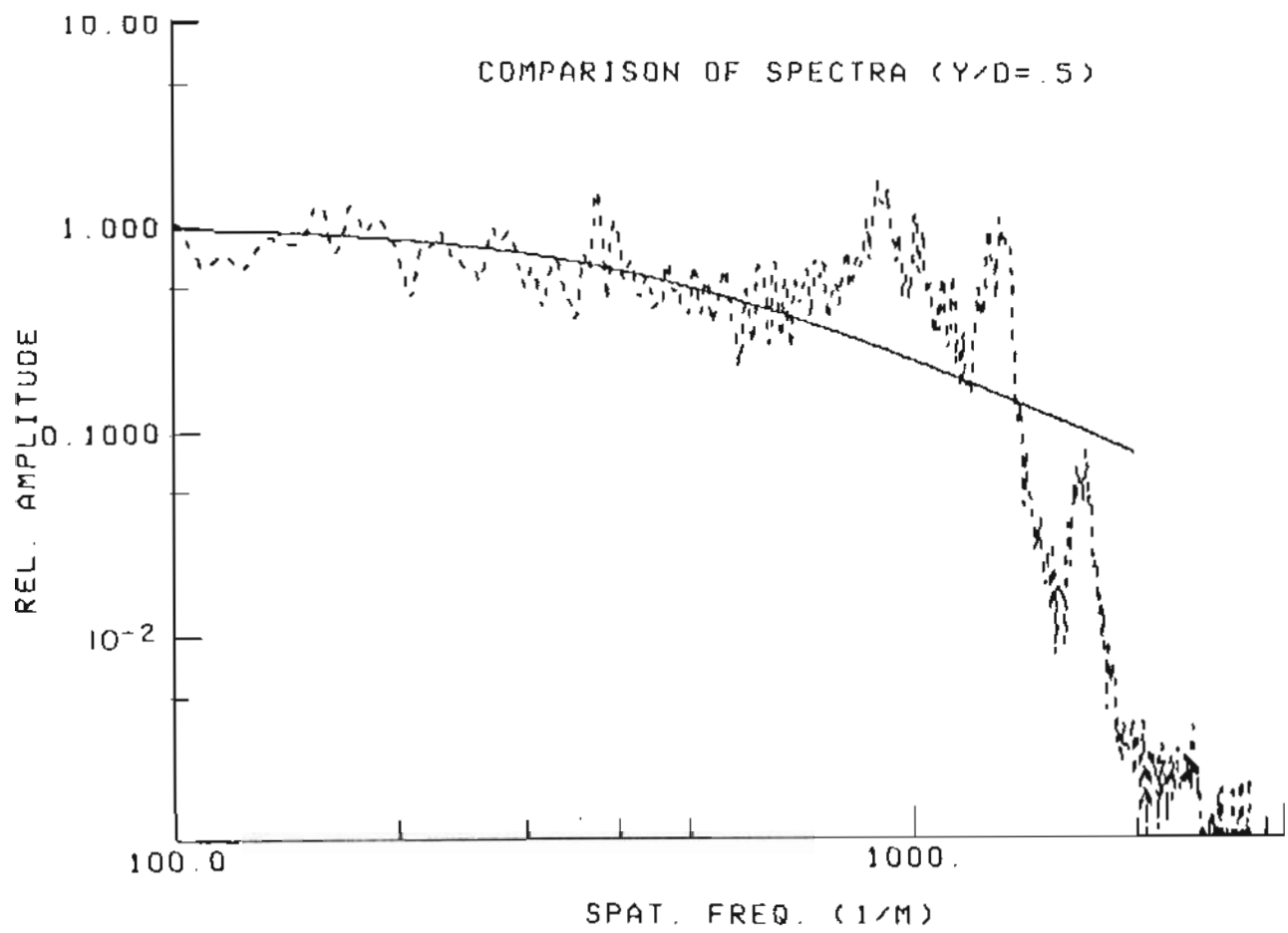


FIGURE 22. Comparison of Experimental and Theoretical Spectra

unimportant high frequency peaks. As noted in Chapter IV, even the hot wire anemometer does not have a sufficiently large bandwidth to resolve the high frequency (~ 10 MHz) components of the turbulence field, and thus the hot wire spectrum "rolls off" at high (spatial) frequency. The overall agreement of the one-dimensional von Karman spectrum with the hot wire spectral data justifies the use of the three-dimensional von Karman spectrum in the extended Huygens-Fresnel calculations which follow.

It is also possible to calculate the functional form of C_n^2 as a function of propagation path from the R.M.S. density data measured by the hot wire anemometer. From the definition of the refractive index covariance function, it may be shown that:

$$\langle n_1^2 \rangle = B_n(0) = \int d^3\vec{\kappa} \Phi_n(\kappa, z) \quad (10)$$

Following the notation presented in Chapter III,

$$\langle n_1^2 \rangle = C_n^2(z) \int d^3\vec{\kappa} \Phi_n^0(\kappa) \quad (11)$$

Thus,

$$C_n^2 \propto \langle n_1^2 \rangle \propto \langle \rho' \rangle / \bar{\rho} \quad (12)$$

where the proportionality constants have been previously determined in Chapter III (see Eq. (43), Chap. III). A plot of C_n^2 as a function of y/δ is shown in Figure 23. It is possible, at this point, to quantitatively test the validity of the reduced hot wire/pitot tube data in two ways.

Figure 24 shows the power spectra of the fluctuating hot wire signal (E') for three values of y/δ and, consequently, three different values of the Mach number (velocity). It is readily apparent that the general form of the three spectra is the same with the exceptions that the detailed structures in the curves (peaks) are shifted toward lower frequencies and that the peaks tend to be broadened with decreasing velocity (decreasing y/δ). This is most easily seen by comparing the location and width of the same shock-induced peak in the three spectra as illustrated in Figure 24.

The frequency composition of the signal will be determined by both the range of turbulent eddy sizes and the local flow velocity at the specific probe locations. If, as a first approximation, the range of eddy sizes is assumed to be fairly constant over the turbulent boundary layer, then the faster these eddies are convected past the hot wire probe, the larger the frequency bandwidth of the resulting signal. Since the local velocity perturbations are small compared to the local mean velocity, the bandwidth of the spectra should scale, at least to first order, with the local mean velocity. Local mean velocity information has already been presented in Chapter IV as a result of the pitot tube measurements (see Figure 10) and is presented in Figure 25 in a slightly

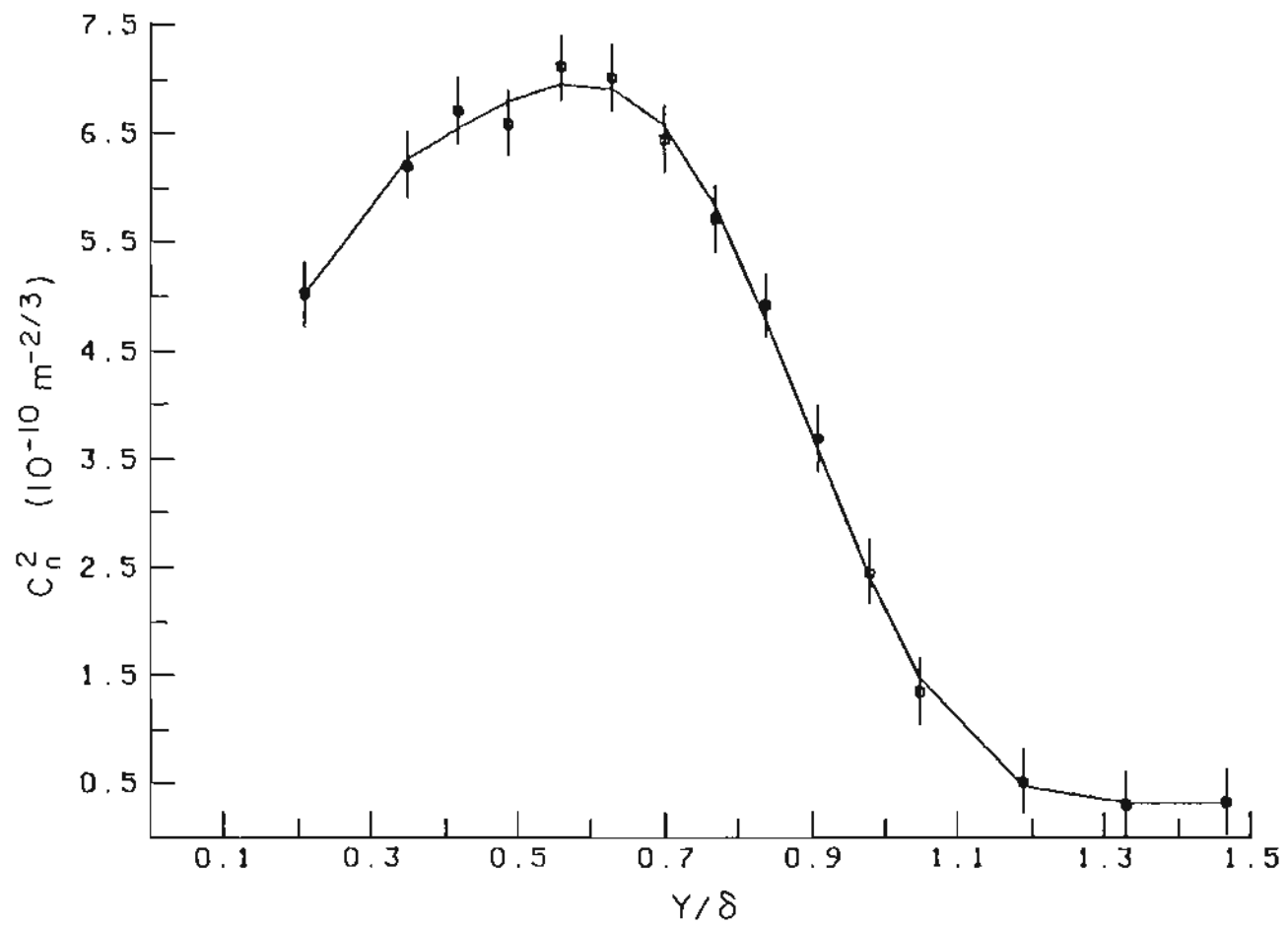


FIGURE 23. C_n^2 vs. y/δ

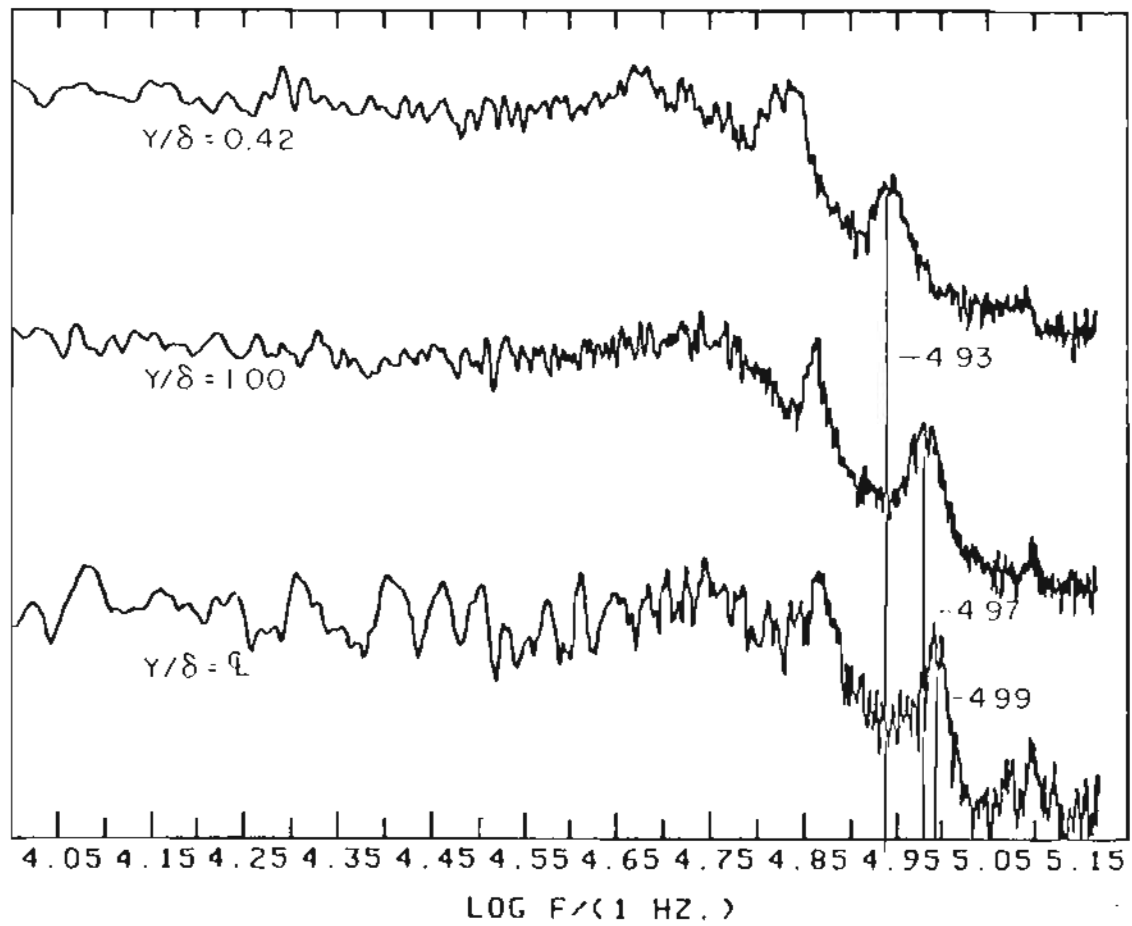


FIGURE 24. Power Spectra at $y/\delta = 0.42, 1.00$ and C. L.

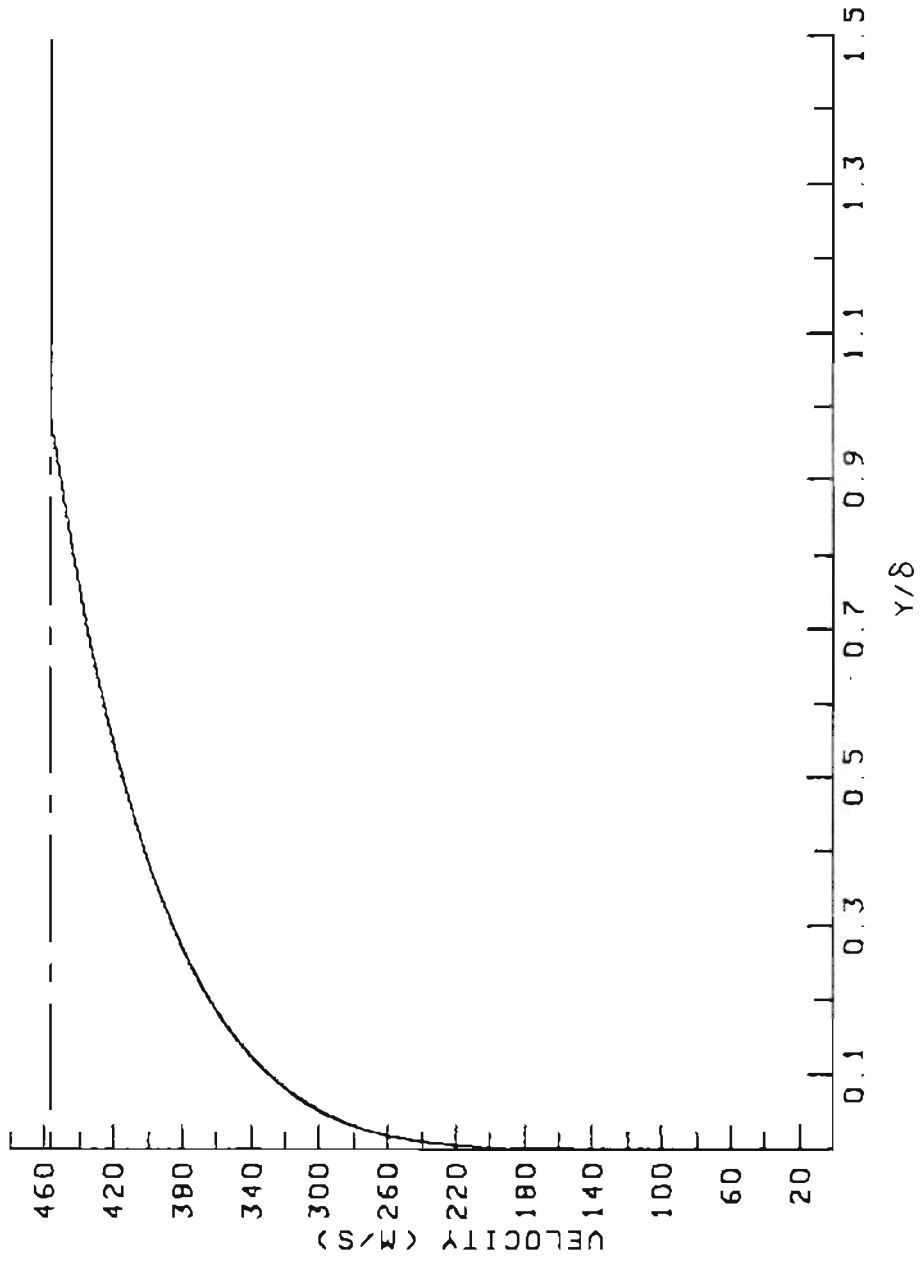


FIGURE 25. Mean Velocity vs. y/δ

different form.

Given the rationale outlined above, the structure of the spectra should scale with local mean velocity in just the manner illustrated by the curves in Fig. 24. A given shock-induced peak should occur at a smaller frequency value for a lower mean velocity due to the fact that it is being convected more slowly past the hot wire probe and will thus affect the signal for a longer period of time. The width of the spectral peak will tend to increase with a smaller local mean velocity for the same reason.

Certainly these spectra conform to the expected results in a qualitative fashion, but it is also possible, using the data presented in Figures 24 and 25, to test the validity of the spectral results in a quantitative manner as well. The relationship between frequency and mean velocity is given by:

$$f \propto V \tag{13}$$

where f is the peak frequency of a shock induced-spectral artifact and V is the local mean velocity at the given point y/δ . Thus:

$$f_i/f_j = V_i/V_j \tag{14}$$

$$\text{Log}(f_i) - \text{Log}(f_j) = \text{Log}(V_i/V_j) \tag{15}$$

This result may be tested by substituting the numbers shown in

Figures 24 and 25 in Eq. 15. Using the values for the two points y/δ on the centerline and $y/\delta = 0.42$, the left side of Eq.(15) is evaluated at 0.060 while the right side is 0.058. Thus the frequency behavior of the spectral data scales with mean velocity as expected from the basic physics of the problem.

A second quantitative test of the spectral results may be accomplished by comparing the low frequency average of the spectral data to the C_n^2 curve presented in Figure 23. Since the C_n^2 information was generated by the RMS averaging of the refractive index perturbation values (n_1) generated from the hot wire/pitot tube survey, the "amplitude" of the spectra (or the spectral values averaged over the lower frequencies) should be proportional to the value of C_n^2 at the probe location.

Figure 26 shows a quantitative plot of the spectra described above (taken at $y/\delta = 0.42, 1.00$ and the centerline). These spectra have been normalized, for comparative purposes, by the amplitude of the $y/\delta = 0.42$ spectrum and plotted on a standard log-log scale. In order to minimize the effect of scale error, consider the difference between the amplitudes of the $y/\delta = 0.42$ and the centerline spectra. This is measured to be -0.45. C_n^2 values at these spatial locations may be obtained from Figure 24. The difference in the log of the normalized C_n^2 values is measured to be -0.48. Thus the amplitude of the spectral information also behaves just as one would expect from the physics of the problem.

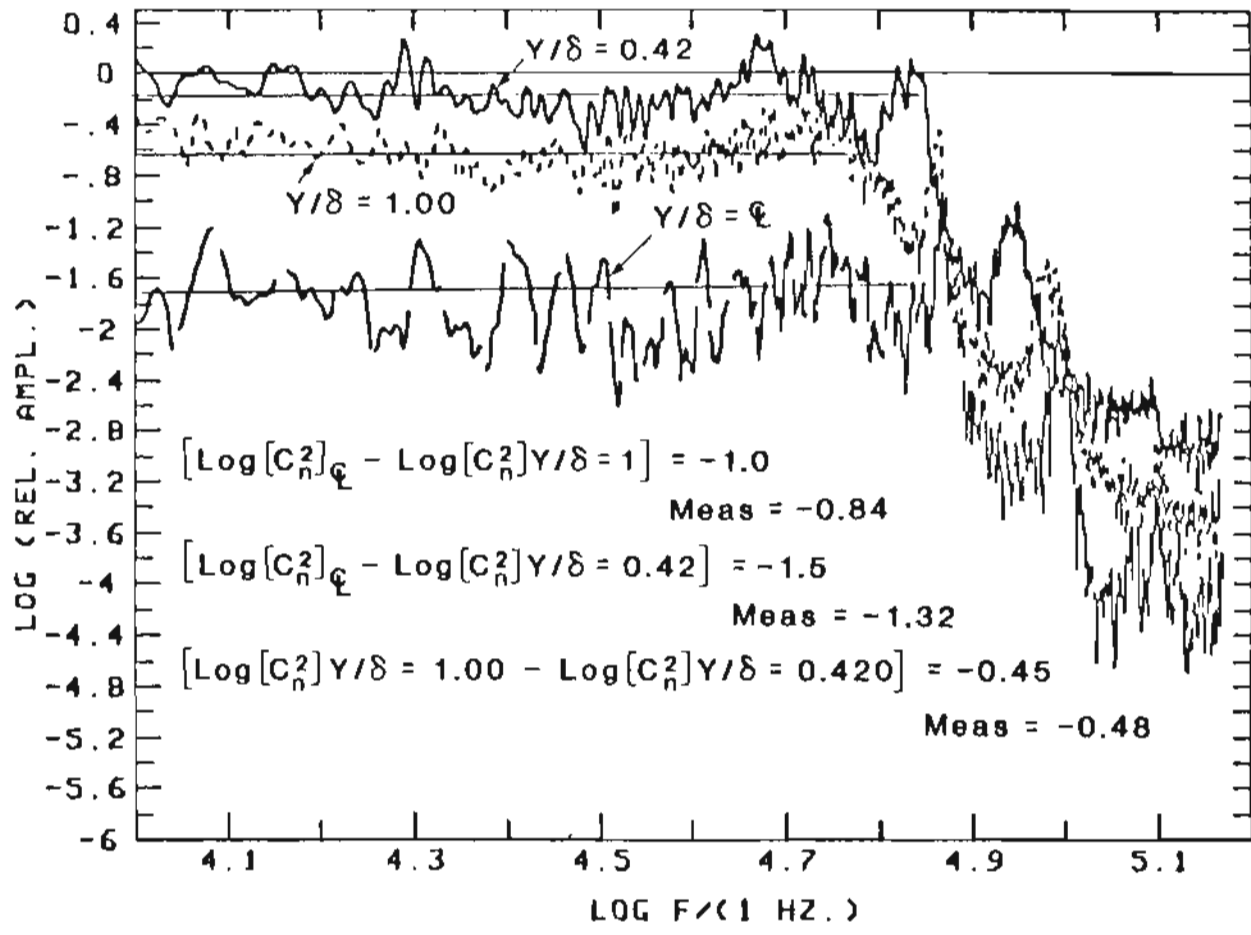


FIGURE 26. Quantitative Spectral Plots

C. A Theoretical Model of the Single Beam Experiment using the Extended Huygens-Fresnel Theory

Using the results of the preceding chapters, it is possible to model a single beam experiment using the extended Huygens-Fresnel theory. A block diagram of the experimental arrangement is shown in Figure 27.

The experiment consists of a focused He-Ne laser propagating through the cross-section of the Ludwig tube with the waist of the beam being incident upon an aperture of, at present, arbitrary diameter. The power transmitted by the aperture is collected in a light pipe and transmitted, with negligible loss, to a high speed photodiode. The waist size of the beam and the distance between the input window of the wind tunnel and the aperture (z) are assumed to be variable. Power (as a function of time) is measured by the photodiode, digitized and transmitted to an on-line computer for storage and processing.

Referring to the theoretical development presented in Chapter III, the first calculation involving the functional forms of ϕ_n and C_n^2 occurs in Equation (37) (Chap. III), presented here in slightly modified form:

$$\langle \psi_1(\vec{r}_1, \vec{p}) \psi_1^*(\vec{r}_2, \vec{p}) \rangle = 4\pi^2 z k^2 \int_0^\infty d\kappa \kappa \phi_n^0(\kappa) \int_0^1 dt C_n^2[(1-t)z] J_0(t\kappa r) \quad (16a)$$

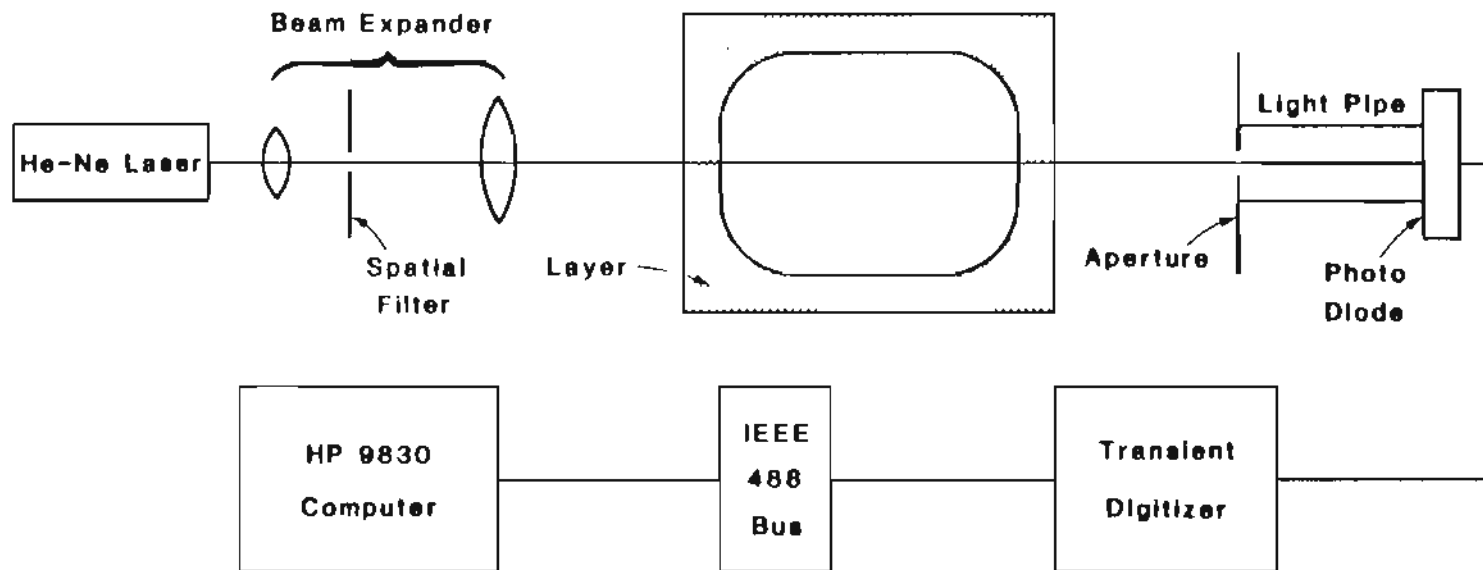


FIGURE 27. Block Diagram of the Single Beam Experiment

where:

$$r = |\vec{r}_1 - \vec{r}_2| \quad (16b)$$

It has been shown from the results of the hot wire/pitot tube survey that the spectrum of the refractive index fluctuations may be written in the form:

$$\Phi_n^0 = (\kappa^2 + \kappa_0^2)^{-11/6} \quad (17)$$

The integration over κ in Eq. (16) (I_κ) may be reduced to:

$$I_\kappa = \int_0^\infty d\kappa \kappa J_0(a\kappa) / (\kappa^2 + \kappa_0^2)^{11/6} \quad (18)$$

where $a \equiv tr$. Eq. (18) may be integrated in closed form to yield:⁵⁹

$$I_\kappa = (a/2\kappa_0)^{5/6} \cdot (\Gamma\{11/6\})^{-1} \cdot K_{-5/6}(a\kappa_0) \quad (19)$$

where K refers to the modified Bessel function of the second kind.

Using the definition of this function, it may be shown that:⁶⁰

$$K_{-\nu} = K_\nu = \{\pi/2\sin(\nu\pi)\} \cdot (I_{-\nu} - I_\nu) \quad (20)$$

where I refers to the modified Bessel function of the first kind and may be expressed as the following infinite series:⁶⁰

$$I_\nu(z) = (z/2)^\nu \sum_{k=0}^{\infty} [k! \Gamma(1 + \nu + k)]^{-1} \cdot (z^2/4)^k \quad (21)$$

By combining Equations (19), (20) and (21) it is possible to show that the k th term of K will depend on the quantity:

$$K_{5/6}(z) \propto [(z/2)^{2k}/(k! \Gamma(k + 1/6)) - (z/2)^{2(k + 5/6)}/(k! \Gamma(k + 11/6))] \quad (22)$$

where:

$$z = t \kappa_0 r \quad (23)$$

It is possible to estimate both the upper and lower bounds of z by noting that:

$$0 \leq t \leq 1$$

$$\kappa_0 \sim 2\pi/\delta = 440 \text{ m}^{-1} \quad (24)$$

where δ is the turbulent boundary layer thickness (see Chapter IV). The integrands of the extended Huygens-Fresnel theory will fall to zero rapidly for values of $r > 2w$ where w is the radius of the Gaussian beam.

For this experiment, the maximum value of r will be about 2mm. Thus:

$$0 \leq t\kappa_0 r \leq 1, \quad 0 \leq z \leq 1$$

Substituting this result in Eq. (22) yields:

$$K_{5/6}(z) \propto \{1/\Gamma(1/6) - (z/2)^{5/6}/\Gamma(11/6) + (z/2)^2/2\Gamma(7/6) + O(|z^2|)\} \quad (26)$$

It is desirable to approximate the second term in Eq. (26) as a quadratic function of z as this will allow the evaluation of the Fresnel integrals in closed form. Figure 28 shows that the function S , defined below, provides an adequate representation of the second term over the range of interest.

$$S(z) \equiv [1.30/\Gamma(11/6)] \cdot (t\kappa_0 r/2)^2 \quad (27)$$

K may then be reduced to:

$$K_{5/6} = [\pi/\Gamma(1/6)](z/2)^{-5/6}(1 - 1.17z^2) \quad (28)$$

Substituting Eq. (28) in Eq. (18) yields:

$$I_k = (3/5)\kappa_0^{-5/3}[1 - 1.17(t\kappa_0 r)^2] \quad (29)$$

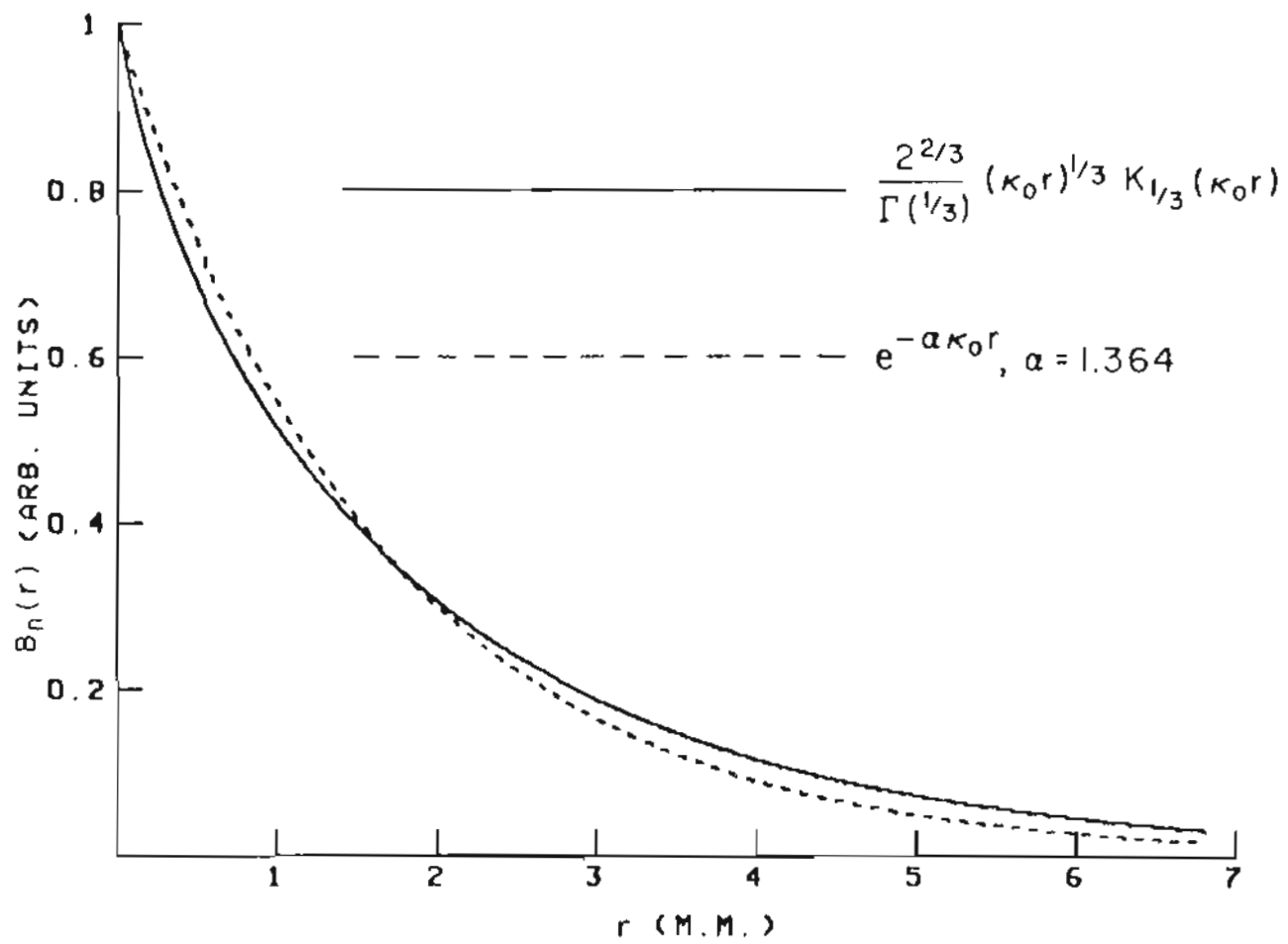


FIGURE 28. Second Term Approximation

and, thus, Eq. (16) may be reduced to:

$$\langle \psi_1(\vec{r}_1, \vec{p}) \psi_1^*(\vec{r}_2, \vec{p}) \rangle = (2.4\pi^2 z k^2 / \kappa_0^{5/3}) \cdot \int_0^1 dt C_n^2 [(1-t)z] [1 - 1.17(\kappa_0 t r)^2] \quad (30)$$

Again referring to Chapter III (Eq. (16):

$$F \equiv \text{Exp}\{\langle |\psi_1|^2 \rangle - \langle \psi_1(\vec{r}_1, \vec{p}) \psi_1^*(\vec{r}_2, \vec{p}) \rangle\} \quad (31)$$

The argument of Eq. (31) may be evaluated using Eq. (30).

$$\langle |\psi_1|^2 \rangle - \langle \psi_1 \psi_1^* \rangle = (14/5)\pi^2 z k^2 \kappa_0^{1/3} r^2 \int_0^1 dt t^2 C_n^2 [(1-t)z] \quad (32)$$

Figure 23 shows the measured variation in C_n^2 with the normalized length coordinate y/δ , where δ refers to the boundary layer thickness. In order to derive an analytical representation of this function, a quadratic equation in y/δ has been fit to the curve of Fig. 23. Figure 29 shows the detail of the resultant fit while Figure 30 shows the complete variation in C_n^2 along a cross section of the Ludwig tube. The two peaks represent the maximum turbulence levels in the boundary layers on each wall while the small constant turbulence level in the center of the nozzle represents the near laminar flow in that region.

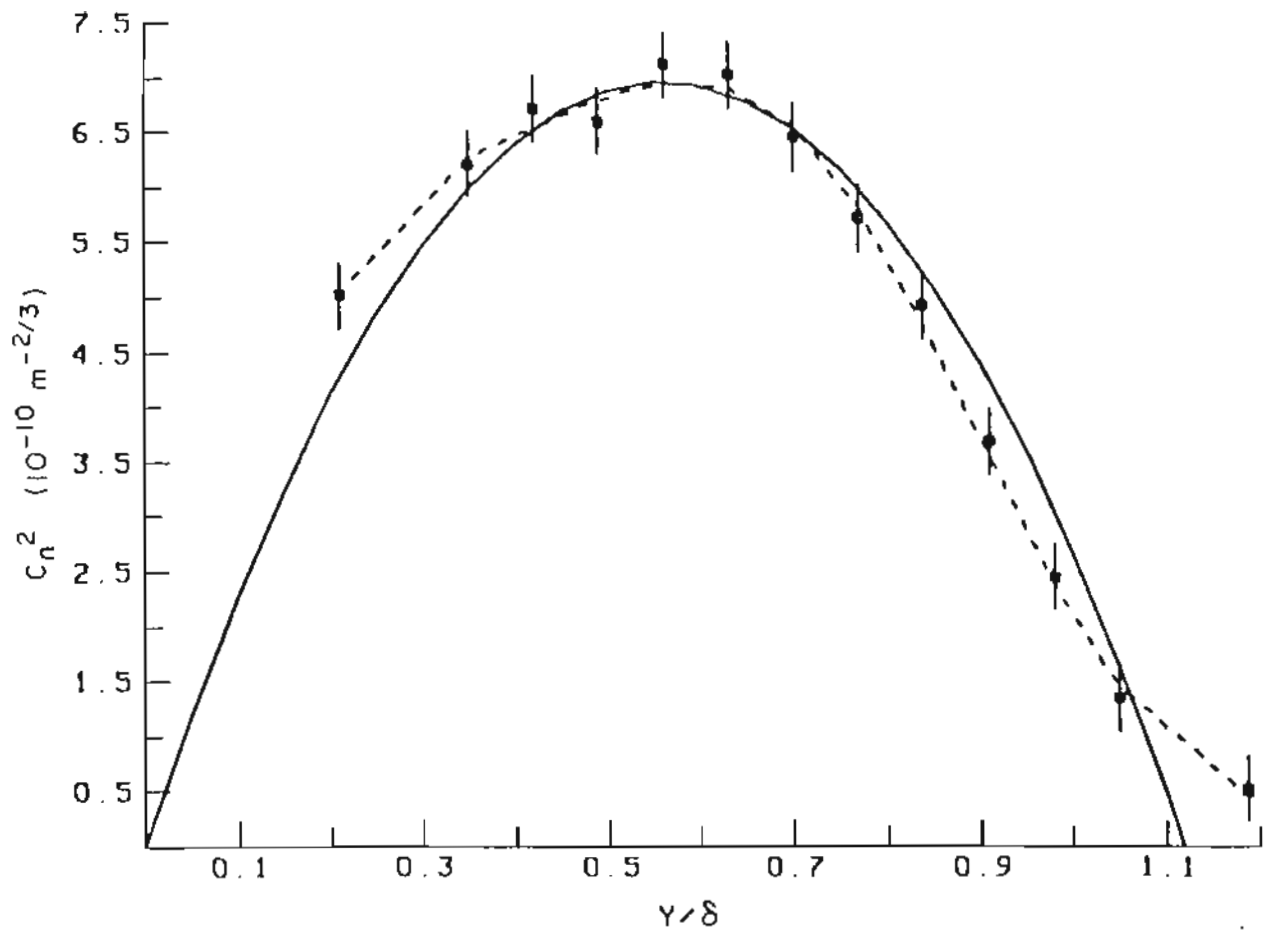


FIGURE 29. Analytical Fit to $C_n^2(y/\delta)$

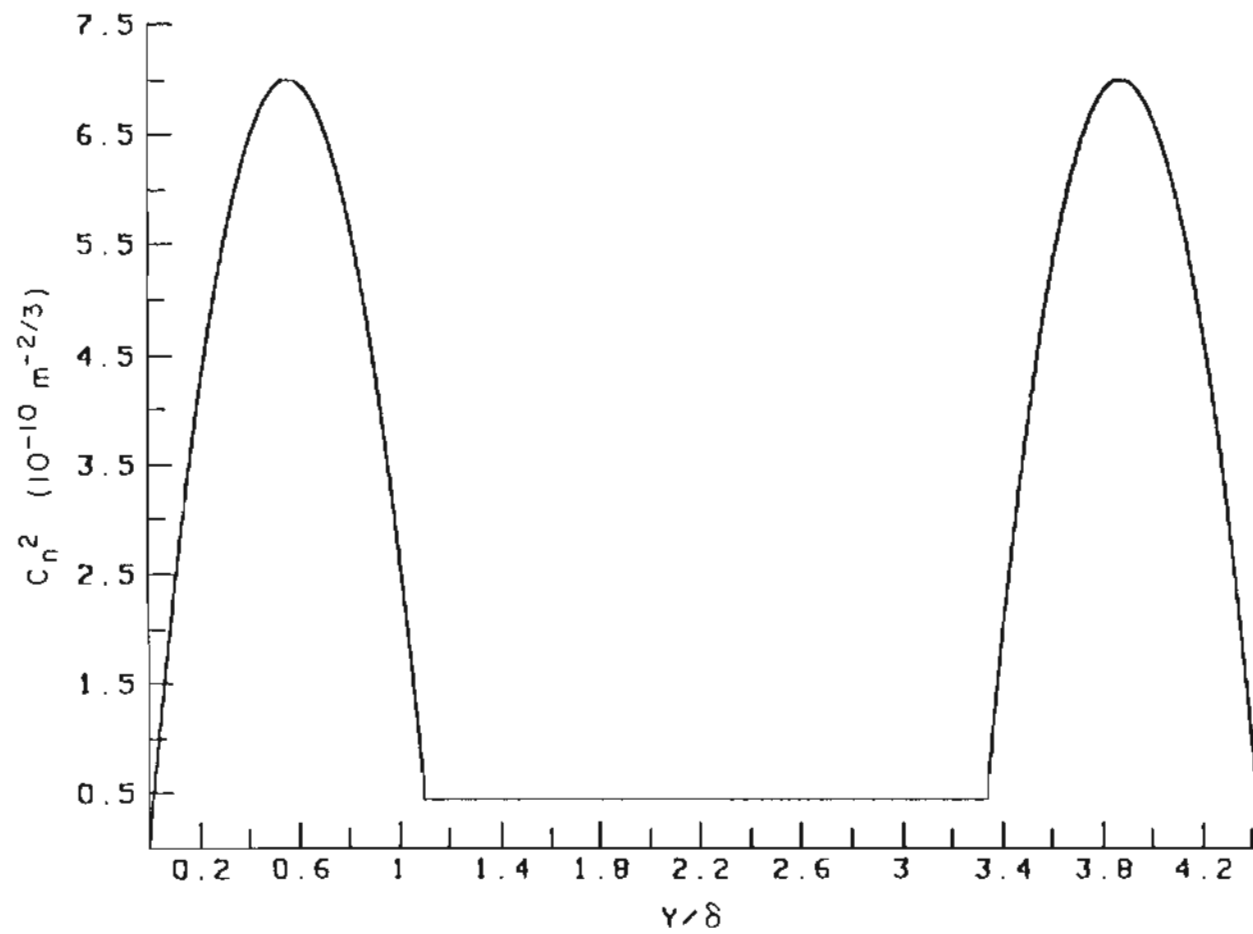


FIGURE 30. C_n^2 as a Function of Position

$C_n^2(y/\delta)$ may be written in the form:

$$\begin{aligned}
 C_n^2(y/\delta) &= 7[1 - 3.19(y/\delta - 0.56)^2] \quad 0 \leq y \leq 1.10\delta \\
 C_n^2(y/\delta)/(10^{-10} \text{ m}^{-2/3}) &= 0.45 \quad 1.10\delta \leq y \leq 3.34\delta \\
 &= 7[1 - 3.19(y/\delta - 3.88)^2] \quad 3.34\delta \leq y \leq 4.44\delta
 \end{aligned} \tag{33}$$

Eq. (33) may now be substituted in Eq. (32) and the integration over t carried out. While this is a tedious process, the solution involves only the use of elementary methods and will not be presented in detail. This evaluation of the integration over t (I_t) in Eq. (32) yields:

$$I_t = C_n^2(\delta/z)\alpha \tag{34a}$$

where:

$$\alpha \cong 1 - 4.42(\delta/z) + 7.42(\delta/z)^2 \tag{34b}$$

Eq. (32) may thus be written in the form:

$$\langle |\psi_1|^2 \rangle - \langle \psi_1 \psi_1^* \rangle = Ar^2 \tag{35a}$$

where:

$$A \equiv (14/5)\pi^2 k^2 C_n^2 K_0^{1/3} \alpha \delta \quad (35b)$$

Thus:

$$F = \text{Exp}\{-Ar^2\} \quad (36)$$

As shown in Chapter III, the average light intensity at the transverse point p ($\langle I(p) \rangle$) may be written as:

$$\langle I(p) \rangle \propto \int d^2\vec{r} \text{Exp}\{-4T\vec{r}^2\} \int_0^\infty dr r \text{Exp}\{-(A + T)r^2\} J_0(rx) \quad (37)$$

where:

$$T \equiv kb/[2(b^2 + 4z^2)]$$

$$x = |N\vec{R} - (k/z)\vec{p}|$$

$$N \equiv (k/z)[1 - 4z^2/(4z^2 + b^2)]$$

z is the distance between the source and observation planes, b is the confocal parameter of the laser beam (see Chap. III) and J_0 is the zeroth order Bessel function.

The calculation of the average power transmitted by the aperture

may be accomplished by integrating Eq. (37) over the area of the aperture.

$$\langle P \rangle = \left\langle \int d^2\vec{p} I(\vec{p}) \right\rangle = \int d^2\vec{p} \langle I(\vec{p}) \rangle \quad (38)$$

Thus the average power, normalized by the power transmitted by the aperture in the absence of turbulence, is given by:

$$\langle P \rangle / P_0 = (1 - \text{Exp}\{-k^2/4z^2\} [16T/(16TB + N^2)] \Delta^2) / (1 - \text{Exp}\{-2\Delta^2/w_0^2\}) \quad (39)$$

where:

$$B = A + T \quad (40)$$

Δ is the radius of the aperture and w_0 is the radius of the Gaussian laser beam. Eq. (39) becomes unity in the absence of turbulence.

The average power ratio given in Eq. (39) may be measured in a laboratory environment with a large signal-to-noise ratio. Thus the comparison of the measured values of $\langle P \rangle / P_0$, as a function of both z and b (w_0), with Eq. (39), will make a definitive statement regarding the ability of the extended Huygens-Fresnel theory to model the effect of supersonic turbulence on optical radiation.

Figure 31 shows $\langle P \rangle / P_0$ as a function of z for three values of the

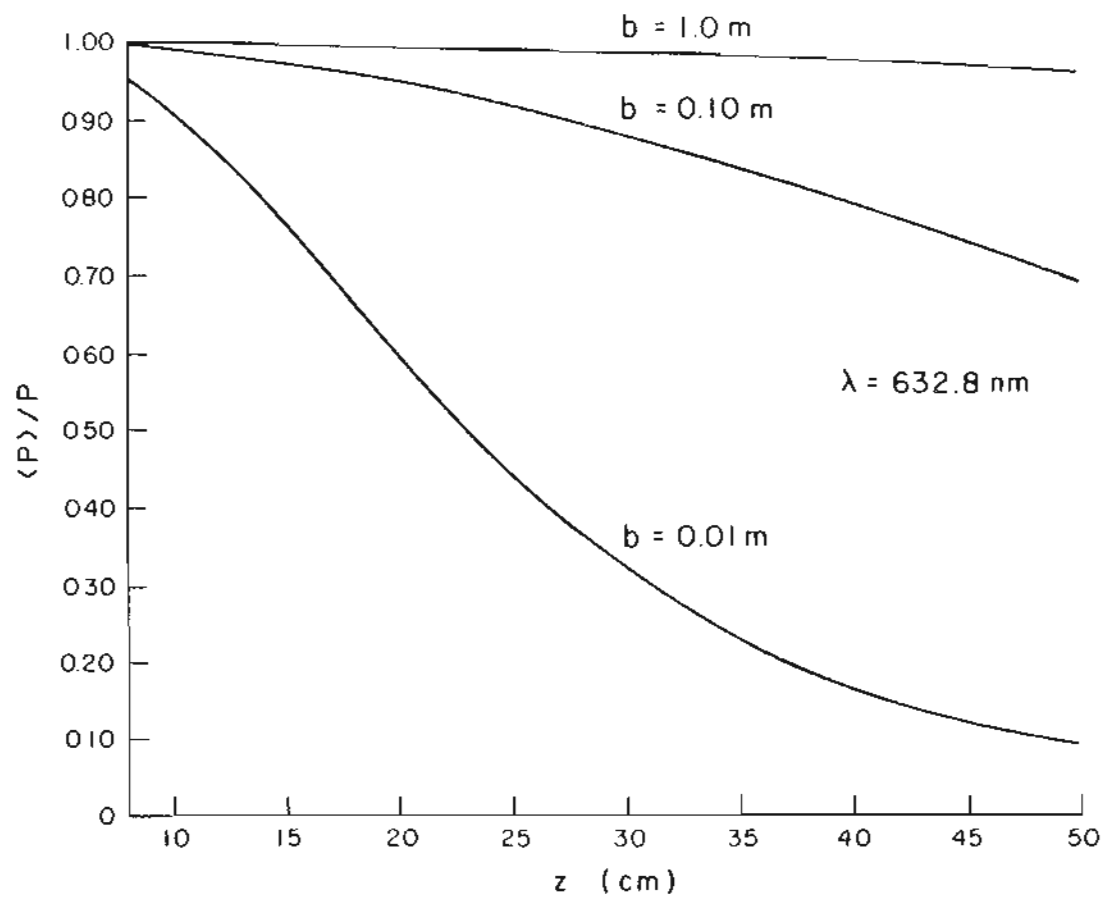


FIGURE 31. $\langle P \rangle / P$ as a Function of Z

beam confocal parameter (b). The range of b extends from rather weak focusing ($b = 8\text{cm}$) to very strong focusing ($b = 7\text{mm}$). It is evident from the basic physics of the problem that the normalized average power transmitted by the aperture should decrease directly (approximately) with z and inversely with b . The z dependence is due to the fact that the absolute beam position on the aperture will be determined by the product of the deflection angle introduced by the turbulence and the distance between the point of perturbation and the aperture which will increase (less power incident on the aperture) as z . The b dependence is due to the fact that, for larger values of w_0 (b), the smaller turbulent eddies will not be large enough to deflect the entire beam, but will tend to "scramble" the laser spot while still keeping the power concentrated near the clear aperture of the pinhole (see Fig. 19), and thus transmitting a relatively large portion of the total beam power. These trends are quite evident in Figure 31, indicating that the theoretical model is correctly predicting the gross qualitative nature of the average power.

The implementation of a series of experiments based on the above development and the results of these experiments are discussed in the following chapter.

CHAPTER VI

THE RESULTS OF THE SINGLE BEAM EXPERIMENT

A. Introduction

The engineering details of the actual single beam experiment performed in the NASA Ludwig tube are shown in Figure 32.

The light source for the experiment was a Spectra Physics Model 133 He-Ne laser having a TEM₀₀ output power of 1 mW (nominal). The beam waist radius was 0.4 mm at the output coupler of the laser. An optical multichannel analyzer (OMA) was used to observe the near-field intensity distribution, and the results indicated that it would be necessary to "clean" the raw output beam using a spatial filter in order to obtain a Gaussian intensity distribution.

The raw laser beam was expanded and cleaned by means of the two-element beam expander shown in Figure 32. A 55 mm focal length positive lens was employed to focus the raw beam to a diffraction limited spot size of approximately 28 μm (the term spot size refers to the $1/e^2$ radius of the beam). An aperture having a diameter of 150 μm placed at the waist location was used to filter the non-diffraction limited component of the raw beam. The result of this spatial filtering was a 0.93 mW beam having an intensity distribution matching a Gaussian to

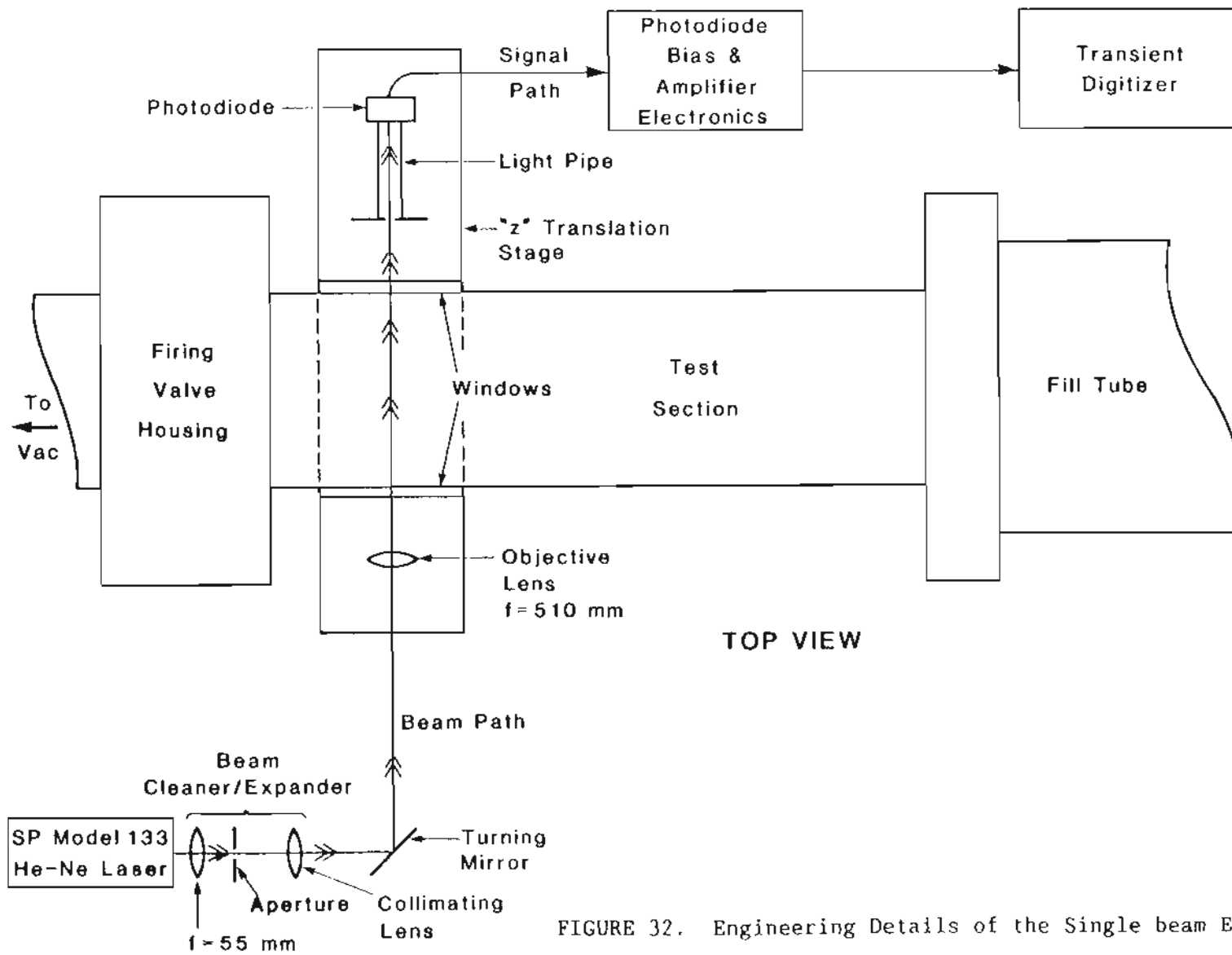


FIGURE 32. Engineering Details of the Single beam Experiment

better than 5% as verified by OMA data. A second positive lens was placed at a distance of one focal length from the waist-aperture location to collimate the Gaussian beam. The focal length of this lens was varied, as described later, to provide three different beam spot sizes propagating across the flow nozzle. The resulting collimated beam had a Rayleigh range of not less than 6 m and thus the beam divergence could be neglected over the distance scales used in this experiment.³⁸ The flexibility provided by this arrangement allowed the scanning of the objective lens/aperture combination so that the average power transmitted by the aperture could be measured as a function of z (see Fig. 31).

An objective lens having a focal length of 510 mm was employed to focus the collimated beam to a waist location about 50 cm away from the lens as shown in Figure 32. The objective lens (and the resulting focal distance) was held constant over the three beam waist sizes used in this experiment. By holding the focal distance constant, it was possible to carry out identical scans across a section of the flow nozzle for each waist value.

The Gaussian beam was focused through the Ludwig tube and onto an aperture of approximately equal to the diameter of the waist. The power transmitted by the aperture was collected by a brass lightpipe and conducted, by internal reflection in the pipe, onto the active area of a United Detector Technology PIN-10 photodiode. The photodiode was operated in the photoconductive mode, using a back bias of 9V and a 50 Ω load resistor. This resulted in a frequency response of the photodiode

in excess of 2 MHz, meaning that the overall frequency cutoff of the data acquisition system was determined by the sampling rate of the external sample-and-hold device.

A Physical Data 515A transient digitizer was employed as the sample-and-hold device. Sampling at various rates showed that the optical signal had little or no frequency components above 200-250 kHz and, therefore, 400 kHz was chosen as the sampling rate for data acquisition. The PD 515A is capable of acquiring four channels of data simultaneously, with each channel having 4096 eight bit words of storage available so at this sampling rate, approximately 10 ms, or one fifth, of the steady state flow could be examined (See Chapter II).

As described in previous chapters, the data stored in the transient digitizer memory was transferred to an H-P 9830 desktop computer via an IEEE 488 bus for off-line analysis. In this case, the analysis consisted simply of averaging the digitized power signal, normalizing and plotting the results.

The objective lens, aperture, lightpipe and photodiode were all mounted on a movable track which could be scanned with one millimeter accuracy. As shown in Figure 32, this meant that the distance from the input window of the wind tunnel to the blocking aperture (z in the analysis of Chapter V) could be varied over an approximately 20 cm range. While this scanning range appears at first glance to be small, it represents about three times the entire width of the flow nozzle and is quite adequate for this purpose.

Three different objective lenses were chosen with focal lengths of

520 mm, 310 mm and 156 mm. These lenses were used to produce Gaussian beams having waist sizes (confocal parameters) of 27 μm ($b = 7.35 \text{ mm}$), 46 μm ($b = 2.05 \text{ cm}$) and 90 μm ($b = 8.02 \text{ cm}$) respectively, corresponding roughly to the range of confocal parameters shown in Figure 31. Figure 33 shows a typical data run as viewed on a monitor oscilloscope showing the digitized data after storage in the memory of the transient digitizer.

B. Vibrational Noise Evaluation

The laboratory wind tunnel environment, by its very nature, harbors many sources of mechanical and acoustical vibrations, all of which are potential noise sources. In order to eliminate the major vibrational noise sources and evaluate the overall signal to noise ratio of the apparatus, the experimental configuration shown in Figure 34 was employed. The beam was diverted around the flow nozzle by means of two turning mirrors. The wind tunnel could then be operated in a normal fashion while any time variation in the transmitted power could be attributed directly to vibrational noise.

Figure 35 shows the results of this test. The reference signal is the response of the photodiode, as viewed by the transient digitizer, while the tunnel is not in operation. The apertured signal is the response of the photodiode during the firing of the wind tunnel. As can be seen from the oscilloscope photos, the vibrational noise induced on the data due to the mechanical operation of the wind tunnel is

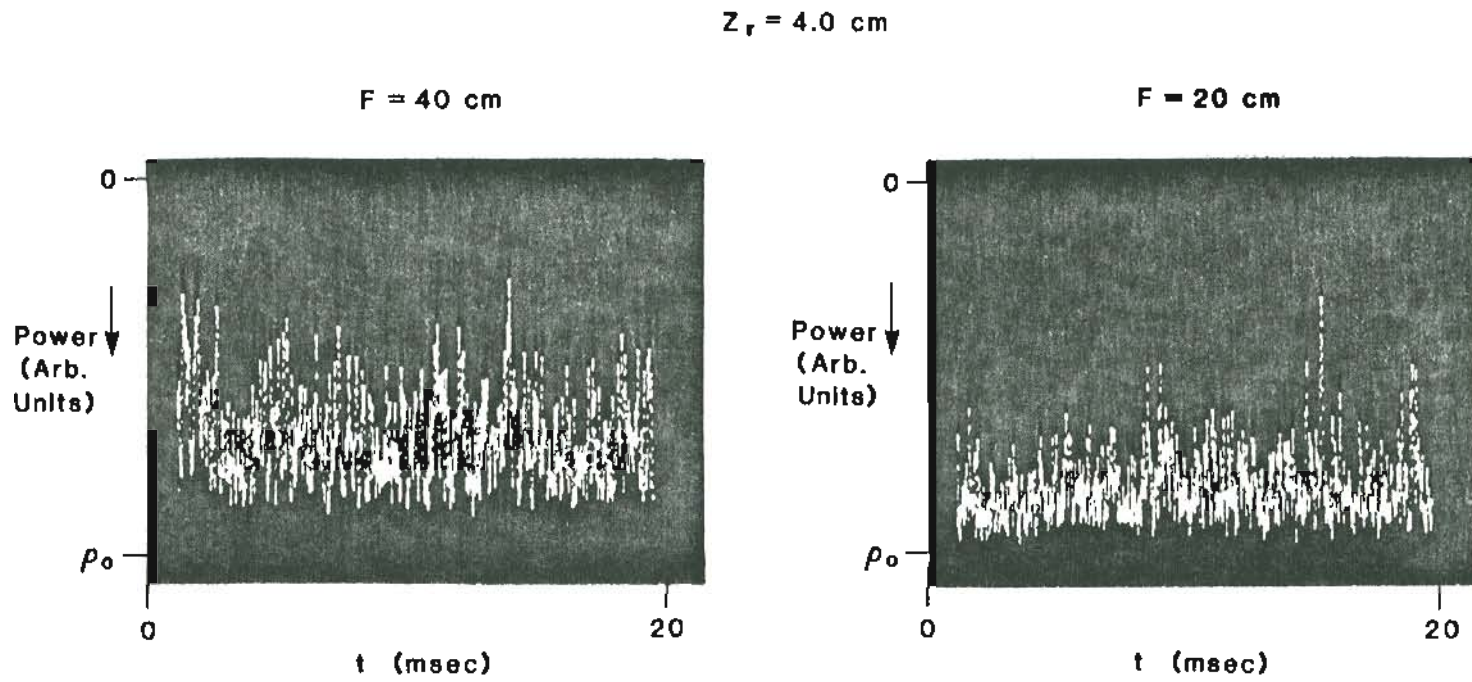
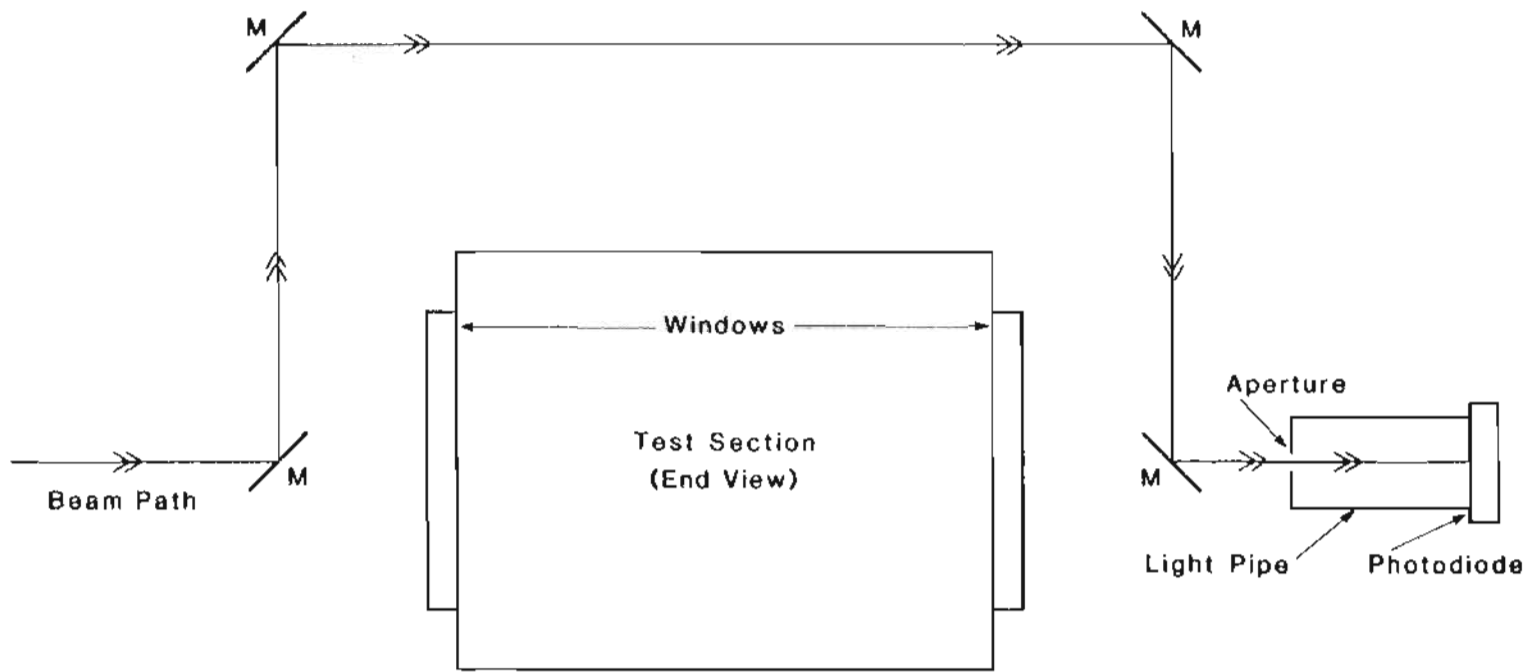


FIGURE 33. Typical Transient Digitizer Output



M - Denotes Plane Mirror

FIGURE 34. Beam Path for Vibration Test

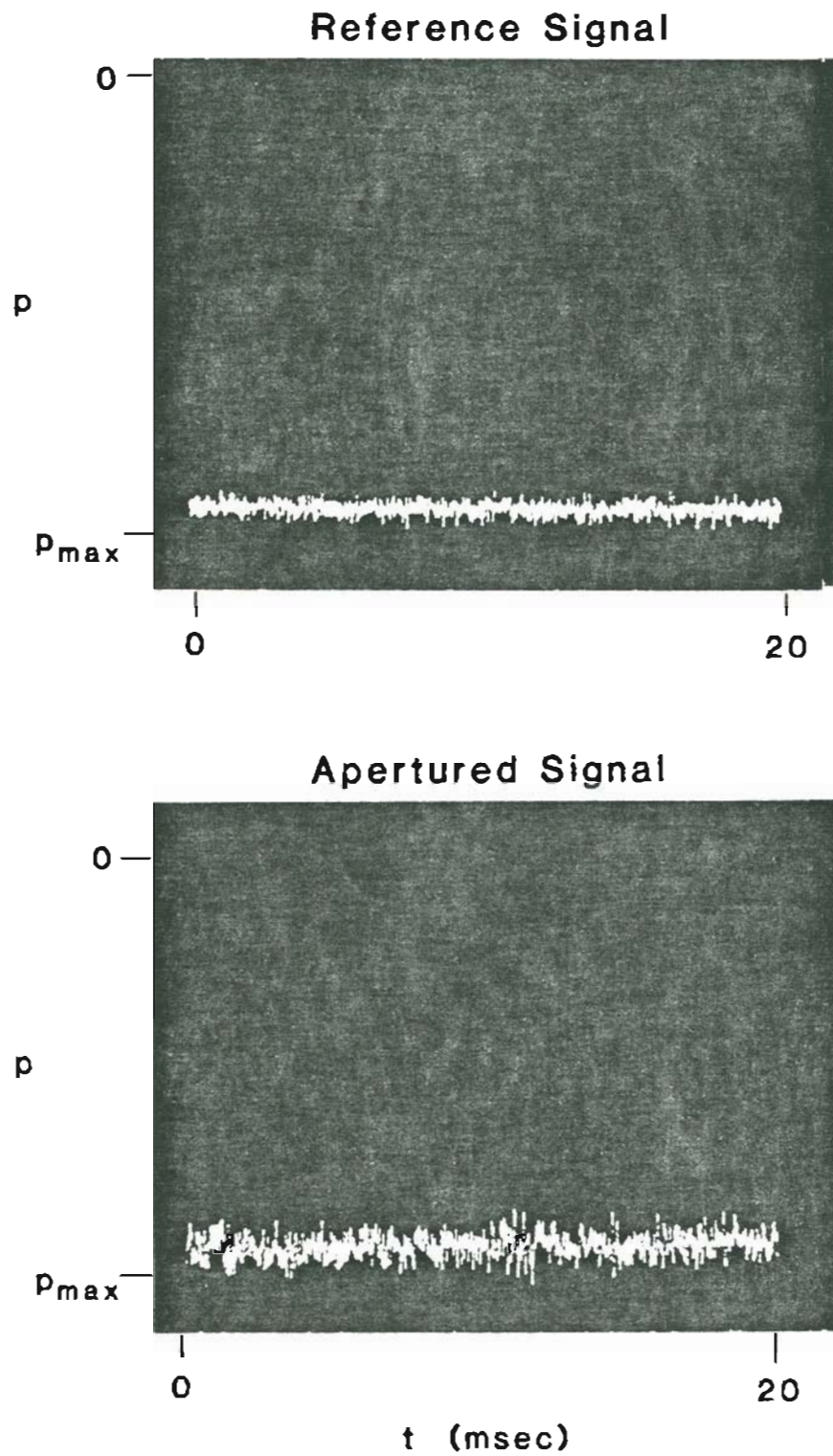


FIGURE 35. Results of the Vibration Test

negligibly small. Quantitative analysis shows that the noise is on the order of five counts out of 1024 full scale (8-bit A/D conversion) yielding a signal-to-noise ratio in excess of 200:1.

C. Correction of the Data for the Effects Introduced by the Windows in the Flow Nozzle

The 0.5 in.-thick fused silica windows which allow optical access to the flow introduce the possibility of two types of error in the data. First of all, a Gaussian beam incident on a window may be imagined as a collection of rays, each having a slightly different angle of arrival at the window. Since the window presents a slab of refracting material to the beam, the beam will be spread slightly as it passes through the window. It is possible to quantitatively estimate the error introduced in the power measurement by calculating the increase in the waist size of the focused Gaussian beam due to the presence of the window. Since the beam deflection produced by the turbulent field in the flow nozzle will be small, the laser beam will be incident on the window at near normal incidence. The beam spread introduced by the window may be modeled using standard paraxial Gaussian beam theory.

The paraxial propagation of a laser beam through various optical elements may be described using the complex function q defined by:⁴⁰

$$q \equiv (1/R) - i(1/Z_r) \quad (1)$$

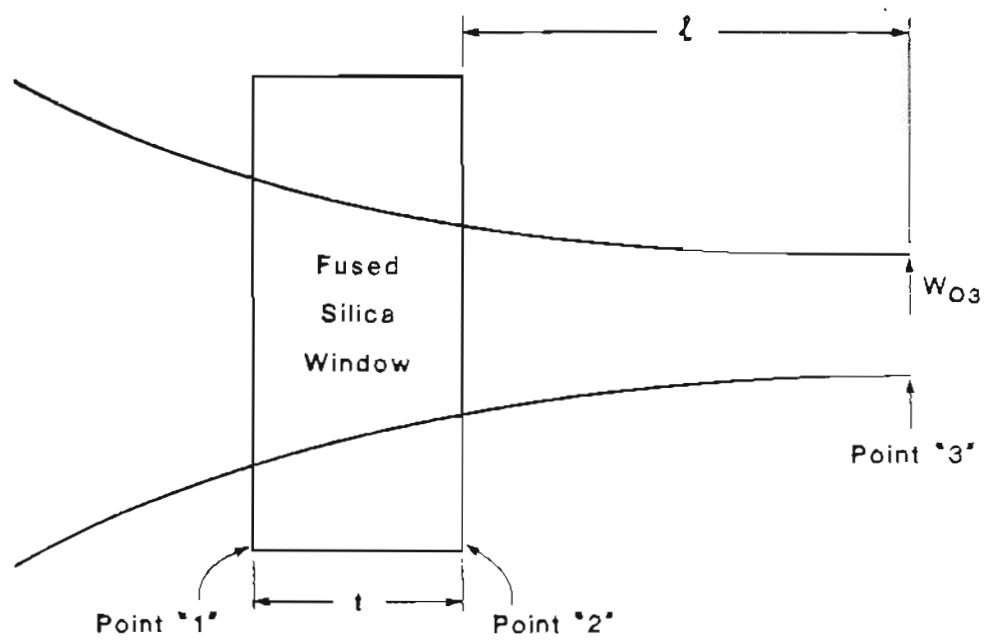
where R is the radius of curvature of the optical phase front, and Z_r is the Rayleigh range of the beam.⁴⁰ The well known ABCD law may be employed to describe the effect of the window on the function q . The mathematical form of this law is given by:⁴⁰

$$q_2 = (Aq_1 + B)/(Cq_1 + D) \quad (2)$$

where A, B, C and D are the elements of the ray matrix describing the propagation of the phase front through a slab of material having a refractive index of n_s .⁴⁰

The geometry of the calculation is shown in Figure 36. A TEM_{00} Gaussian beam propagates through a slab of fused silica as it is focused to a waist. The slab of material depicted in Figure 36 represents the exit window of the flow nozzle. The entrance window may be neglected as the beam spread introduced there will not be a function of the turbulent field parameters and thus will be normalized out when constructing the ratio $\langle P \rangle / P_0$. If the turbulent eddies cause the beam to spread or shrink, the angular spectrum of the ray bundle forming the laser beam will change. This will also produce a change in the refractive effects introduced by the exit window since the angle of incidence of any given ray in the bundle will change.

By employing the ABCD law, the refractive effects of the window may be determined. As shown in Figure 36, the ray matrix elements



$$M_{12} = \begin{vmatrix} 1 & a \\ 0 & 1 \end{vmatrix} \quad M_{23} = \begin{vmatrix} 1 & l \\ 0 & 1 \end{vmatrix}$$

$$M_{13} = M_{23} M_{12} = \begin{vmatrix} 1 & l+a \\ 0 & 1 \end{vmatrix} \equiv \begin{vmatrix} 1 & L \\ 0 & 1 \end{vmatrix}$$

FIGURE 36. Window/Beam Geometry

describing the propagation of the beam are given by:⁴⁰

$$A = 1 \quad (3a)$$

$$B = l + n_s t \quad (3b)$$

$$C = 0 \quad (3c)$$

$$D = 1 \quad (3d)$$

where l is the distance from the air side of the exit window to the beam waist and t is the thickness of the window. Substituting Eqs. (3) into Eq. (2) yields:

$$q_3 = R_1 Z_1^2 / (Z_1^2 + (R_1^2)) + L + i Z_1 R_1^2 / (Z_1^2 + R_1^2) \quad (4)$$

where:

$$Z_1 \equiv \lambda / (\pi w_1^2) \quad (5)$$

and L is the total optical path length between the nozzle side of the window and the waist location ($l + n_s t$). The subscripts refer to the regions shown in Figure 36. Since q_3 is evaluated at the focused waist of the beam, $R_3 \rightarrow \infty$ and:

$$q_3 = iz_{r3} \quad (6)$$

One further useful fact is that since $l \gg z_{r3}$ for all cases considered in this experiment, $R_1 \sim 1$.¹ Using this along with Eqs. (4), (5) and (6), it is possible to show that:

$$w_{03}^2 \propto z_{r3} = \lambda l / \pi w_1^2 \quad (7)$$

If the window was removed from the beam path:

$$w'_{03} \propto z'_{r3} = \lambda l_2 / \pi w_1^2 \quad (8)$$

Thus,

$$w_{03} / w'_{03} = (L/l)^{1/2} \quad (9)$$

substituting the values of the parameters for the NASA flow nozzle yields a beam spread ratio (Eq. (9)) of about 1.03. Thus, the effect of the exit window is negligible assuming the beam does not undergo gross distortion by the turbulent field. This is assured by the design of the experiment (see Chapter V).

There is also a second window perturbation which must be

considered. The primary effect of the turbulent field will be to randomly tilt the entire phase front of the light and thus cause the beam to deflect. This means that the central ray of the beam will exhibit a nonzero, time dependent, angle of incidence on the nozzle side of the exit window (once again the entrance window may be neglected). Since the window will act as a refracting slab, it will affect the angle of arrival on the aperture (as a function of incidence angle) and consequently the instantaneous power transmitted to the photodiode. The refractive effect of the window may best be determined by a ray model. Figure 37 shows the propagation of the central ray of the beam propagating through the window and to the detector plane for an arbitrary incidence angle θ_i . Snell's law, in the small angle approximation, is given by:¹¹

$$n_i \theta_i = n_1 \theta_1 \quad (10)$$

and,

$$\theta_1 = n_i \theta_i / n_1 = 0.69 \theta_i \quad (11)$$

for fused silica. It is possible to show (referring to Figure 37):

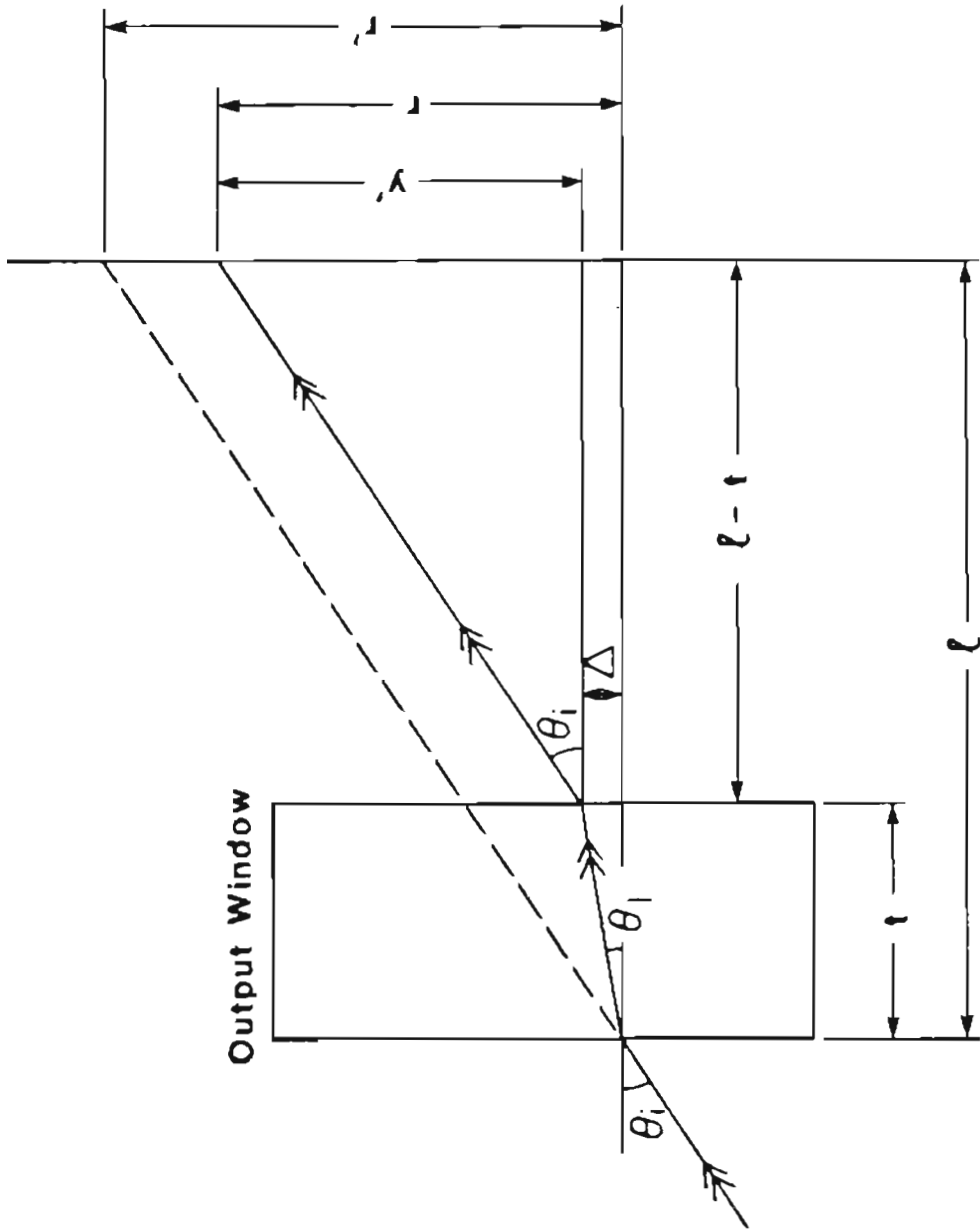


FIGURE 37. Window/Beam Refractive Geometry

$$y' = \Delta + \theta_i(1 - t) \quad (12)$$

Referring again to the geometry shown in Fig 37, it may be shown that:

$$y' = [1 + (\gamma - 1)t]\theta_i \quad (13)$$

and,

$$\Delta y = (\gamma - 1)t\theta_i \quad (14)$$

where γ is 0.69 for fused silica.

Since the beam will be deflected only over a very small angle (on the order of milliradians) the ellipticity in the projection of the beam on the aperture may be neglected and the perturbed beam, at an instant in time, may be modeled on the aperture as two overlapping circles as shown in Figure 38.

In order to estimate the effect of window refraction on the transmitted power, it will be necessary to integrate the truncated Gaussian beam in a very inconvenient geometry. While this is a straightforward calculation, it is very tedious and only an overview will be presented here.

The Gaussian intensity profile of the beam (in polar coordinates) is given by:⁶¹

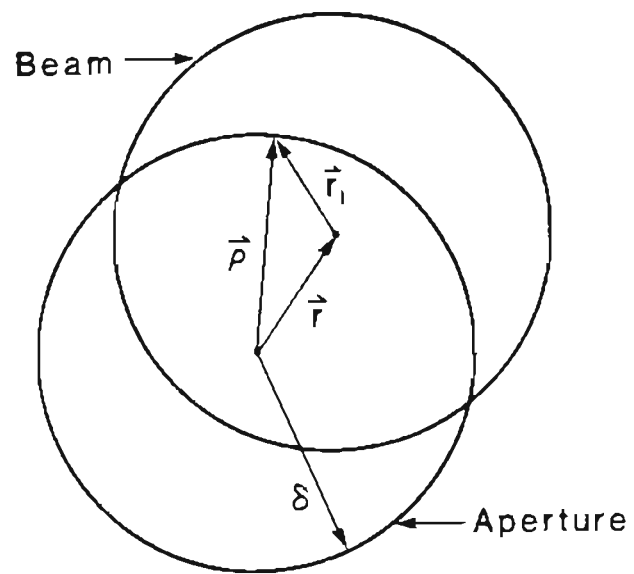


FIGURE 38. A Deflected Beam on the Aperture

$$I = A_0 \text{Exp}\{-2r_1^2/w^2\} \quad (15)$$

where w is the spot size of the beam on the aperture, A_0 is the on-axis intensity and the coordinate r_1 is shown in Fig. 38. The aperture may be described in space by:

$$\rho \leq \delta \quad (16)$$

where δ is the radius of the aperture and ρ is measured from the center of the aperture as shown in Fig. 38. The magnitude of the radius vector ρ may be related to r_1 (again referring to Fig. 38) by the following:

$$r_1^2 = r^2 + \rho^2 - 2r\rho\cos\theta \quad (17)$$

Substituting Eq. (17) into Eq. (15) and integrating the resultant intensity expression over the area of the aperture gives the transmitted power in the form:⁶¹

$$\begin{aligned}
P_t &= A_0 \int_0^{2\pi} d\theta \int_0^\delta d\rho \rho \text{Exp}\{-2(r^2 + \rho^2 - 2\rho r \cos\theta)/w^2\} \\
&= A_0 \text{Exp}\{-2r^2/w^2\} \int_0^\delta d\rho \rho \text{Exp}\{-2\rho^2/w^2\} \int_0^{2\pi} d\theta \text{Exp}\{4r\rho \cos\theta/w^2\} \quad (18)
\end{aligned}$$

By employing an integral representation of the Bessel function, it is possible to write Eq. (18) in the form:⁵⁹

$$P_t = 2\pi A_0 \text{Exp}\{-2r^2/w^2\} \int_0^\delta d\rho \rho \text{Exp}\{-2\rho^2/w^2\} I_0(4r\rho/w^2) \quad (19)$$

where I_0 is the modified Bessel of the first kind. Changing the integration variable in Eq. (19) by the substitution $u \equiv 2\rho^2/w^2$ yields:

$$P_t = (\pi/2)w^2 A_0 \text{Exp}\{-2r^2/w^2\} \int_0^{2\delta^2/w^2} du \text{Exp}\{-u\} I_0[2(2u)^{1/2}r/w] \quad (20)$$

Since $\delta \leq w$ and $r \leq w$ for all cases of interest here:

$$(2u)^{1/2}r/w \leq 4 \quad (21a)$$

and so:

$$I_0\{2(2y)^{1/2}r/w\} \leq I_0(4) \quad (21b)$$

While the integration in Eq. (20) may not be carried out in closed form, it is possible to develop a series expression for the result by noting that, for $0 \leq p \leq 4$, $I_0(p)$ may be accurately approximated by the following polynomial:⁵⁹

$$I_0(p) = 1 + 3.156t^2 + 3.090t^4 + 1.207t^6 + 0.266t^8 + 0.0361t^{10} + 0.0046t^{12} \quad (22)$$

where $t = p/3.75$ and $|\varepsilon| \leq 10^{-6}$.

By substituting Eq. (22) into Eq. (20) and carrying out some tedious but straightforward simplification, it is possible to write a series expression for the normalized power transmitted by the aperture containing only a few terms and accurate to $< 1\%$.

$$P_t/P_0 = \text{Exp}\{-2x^2\} [1 - \text{Exp}\{-2z^2\} + 0.403x^2(1 - \text{Exp}\{-2z^2\}[1 + 2z^2])] + \varepsilon_1 \quad (23)$$

where $x \equiv r/w$, $z \equiv \delta/w$ and $\varepsilon_1/(P_t/P_0) \leq 1\%$.

Referring to Figure 38, it may be shown that the distance between the center of the beam and the center of the aperture in the absence of the window (r') can be related to the value measured with the window in the system (r) by:

$$r = r' \{ 1 - 0.31t / (Z - d) \} \quad (24)$$

(for fused silica) where Z is the distance between the input surface of the first window and the aperture and d is the width of the flow nozzle (≈ 6 cm) measured between the two inner window surfaces.

In order to estimate the magnitude of the refractive effect, the worst relative case will be considered. It is evident from the form of Eq. (24) that the second term will be at its maximum when Z is minimized. For this experiment, $Z \geq 20$ cm. Since the turbulence-induced beam deflection is small, r will be in the range $0 \leq r \leq w$. Substituting these values into Eq. (24) yields:

$$r = 0.977r' \quad (25)$$

Since $x' (= r'/w) = z = 1$, the evaluation of Eq. (23) gives a value of $P_t/P_0 = 0.149$ which is the normalized power transmitted by the aperture neglecting the effect of the window. The evaluation of Eq. (23) for the parameters $x = 0.977$, $z = 1$ yields the value of $P_t/P_0 =$

0.162 which is the transmitted power in the presence of the window. Since these values differ by about 9%, it was evident that the experimental data would have to be corrected for the refractive effect of the exit window.

This was accomplished in the data reduction software by first using the measured value of P_t/P_0 to calculate the refracted value of r using Eq. (20), Eq. (24) was then employed to calculate the unrefracted coordinate r' and Eq. (20) was then used a second time to calculate the normalized transmitted power corrected for the effect of the window.

D. Experimental Results

The single beam experiment was performed in the NASA wind tunnel for the range of focusing mentioned earlier. The results of the experiment are shown in Figure 39 which is a plot of the average normalized transmitted power ($\langle P \rangle / P_0$) as a function of the distance between the input window and the aperture. The solid lines represent the predictions of the extended Huygens-Fresnel model developed in Chapters IV and V. It is readily apparent that this model is quite capable of predicting the effect of bounded turbulent fields in a supersonic flow on Gaussian optical radiation. Its quantitative accuracy rarely exceeds the measurement error in the individual data points.

It should be pointed out, however, that the range of the closed form model (as presented in Chapter V) is limited to turbulent fields

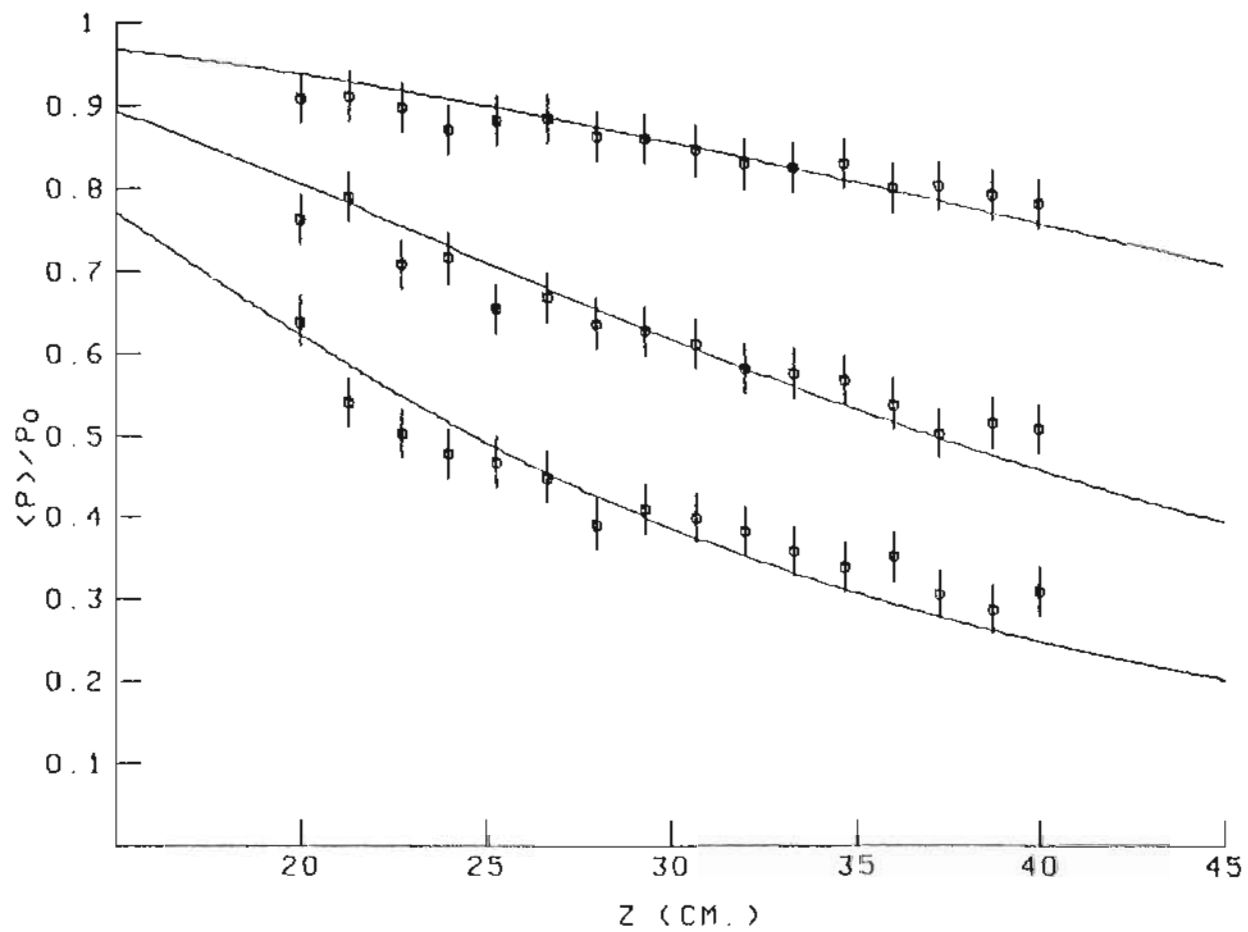


FIGURE 39. Results of the Single Beam Experiment

having a thickness which is small when compared to the optical path length. When the boundary thickness becomes a significant fraction of the optical path, several of the approximations which allowed a closed form solution are no longer valid and a closed form, analytical solution becomes impossible. A treatment of this case is a formidable problem in numerical analysis.

CHAPTER VII

THE DESIGN OF A TWO BEAM EXPERIMENT

A. Introduction

The results of the single beam experiment, presented in Chapter VI, show that the extended Huygens-Fresnel theory of atmospheric optics is capable of modeling the effects of a turbulent boundary field in a supersonic flow. As the basis for a remote sensing device, the single beam approach has the drawbacks that, due to the statistical nature of the theory, real time measurements are not possible and that, due to the path integration inherent in the theory, it is not possible to achieve spatially-resolved measurements. The first drawback is due to a fundamental property of the theory and may not be circumvented. Methods of achieving spatial resolution have been explored in atmospheric turbulence, and it is proposed that these methods be applied to the case of supersonic flow.

Several authors have explored the concept of crossed beam correlation as a remote sensing technique which is capable of providing at least limited spatial resolution.^{16,30,62} The basic concept of this approach is shown in Figure 40. As stated in Chapter III, turbulent eddy size is defined as the distance in space (a sphere in three

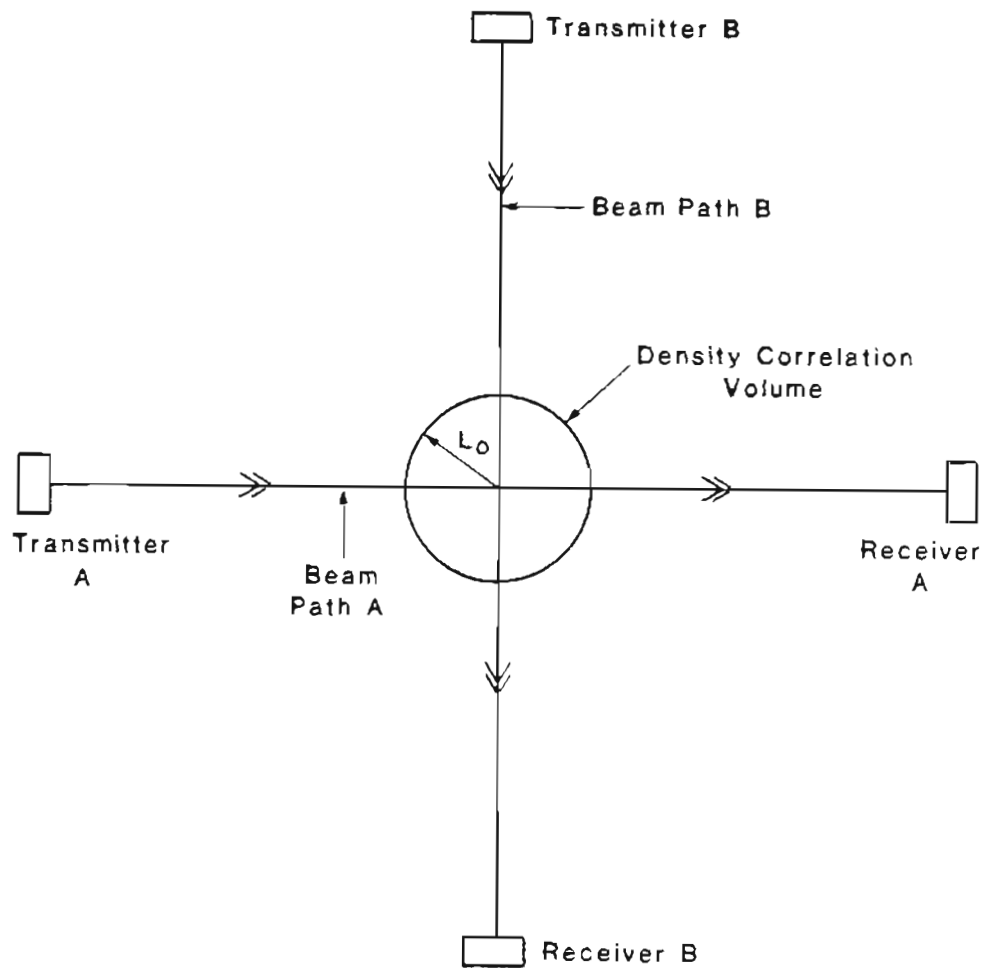


FIGURE 40. Crossed Beam Correlation Geometry

dimensions) in which the density of the working fluid remains constant. In other words, eddy size is a correlation length. L_0 (the outer scale size) represents the largest sphere of density correlation within the flow.

If two small beams propagate through the turbulent field as shown in Fig. 40, the major effect of the turbulence will be to cause beam deflections as described in Chapter V. If the deflection of each beam is measured and the two signals correlated, it is clear that the turbulence along the paths lying more than a distance L_0 from the crossing point will not contribute to the correlation, thus allowing the measurement of information with at least partial spatial resolution.

Several authors have applied this technique in conjunction with a schlieren deflection measurement to the problem of remote sensing in rather large scale flows with some success.^{16,63} The results have tended to be somewhat limited quantitatively due to rather crude theoretical modeling of the problem. One of the goals of this work was to explore the feasibility of using this technique, in conjunction with extended Huygens-Fresnel theory, as the basis for a remote sensing device for use in a supersonic environment. For this to be successful, several problems must be overcome.

The model shown in Figure 40 has only limited spatial resolution due to the distribution of eddy sizes within the flow. Obviously, the effect of a small scale eddy within the correlation volume may be "washed" out by the presence of a larger scale eddy nearby as shown in Figure 41. This presents a severe problem for remote sensing in a small

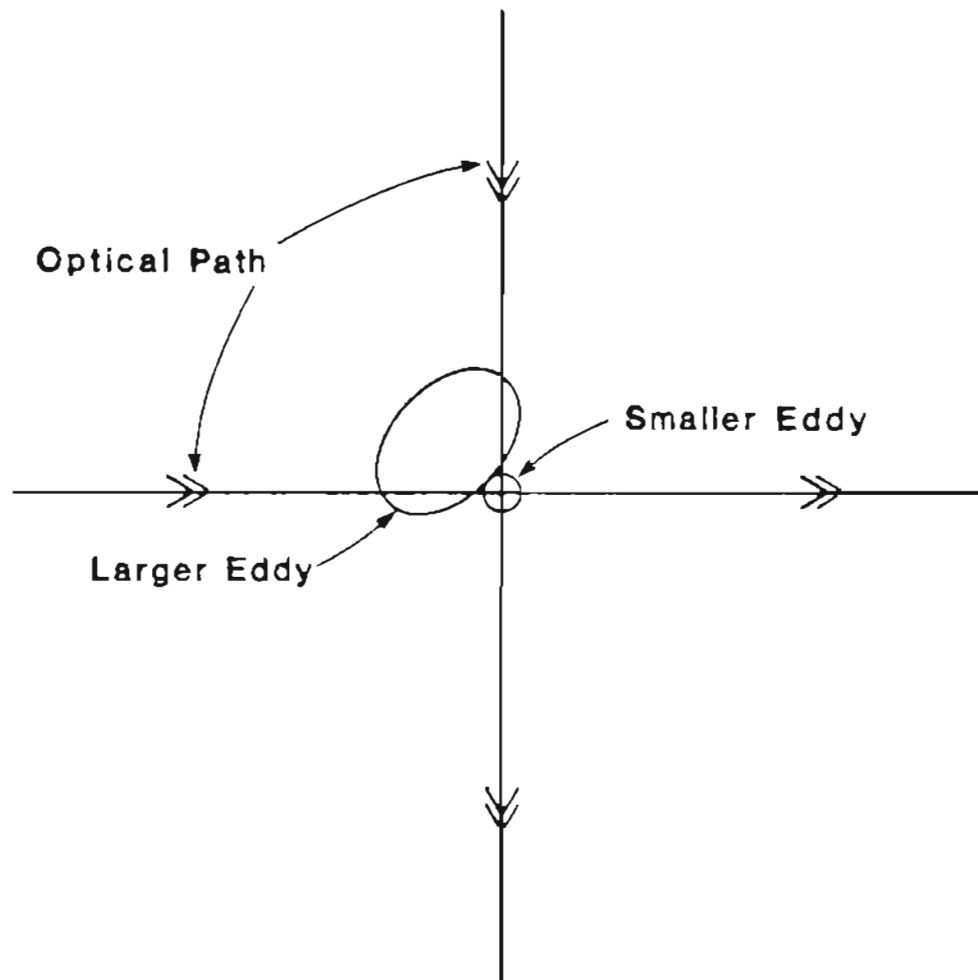


FIGURE 41. Multiple Eddy Interaction

bounded flow, such as found in the NASA test nozzle, since L_0 is on the order of the boundary layer thickness thus rendering impossible any spatially resolved measurements within the layer.

It has been shown that the beam focusing parameters can have a drastic effect on this response, even over a short path length, and thus it was the hope of the author that the use of focused beams might present a way around this difficulty. This technique will be discussed in detail in a later section of this chapter.

Another approach involved modeling the turbulent boundary layer as a series of two dimensional flow fields (phase screens) stacked one after the other.⁵⁶ If the turbulent field behaves in this manner, it means that the maximum correlation distance along the optical propagation path is quite small and not a significantly limiting factor. There is some evidence for this in the results of the single beam experiment due to the successful use of the $C_n^2(z)$ function in the extended Huygens-Fresnel theory (see Chapter III). This technique has been employed in atmospheric optics only for the case of $C_n^2(z)$ varying over distances in excess of the outer scale size (L_0). This condition was, of necessity, relaxed in the Ludwig tube model, and the resultant success of this model is evidence that the effective outer scale size along the propagation path may be much smaller than the boundary layer thickness (δ). An experiment using two hot wire probes simultaneously present in the flow to measure the longitudinal correlation length (and thus determine the applicability of the phase screen model), failed due to cross-talk (shock wave interference) between the two intrusive

probes. The applicability of this approach was also rendered indeterminate by problems with the optical experiments which will be presented later.

One final problem with the traditional atmospheric theory is the need to separate the phase and amplitude information carried by the optical radiation.⁵⁸ As will be shown shortly, this requirement is due to the basic formalism of the atmospheric optics model. It was the hope of the author that a similar theoretical approach could be used to model the intensity of the arriving radiation, as was done in the single beam theory, and consequently achieve adequate spatial resolution by a direct optical power measurement.

The various techniques and ideas presented above will be analyzed in detail in the following sections of this chapter. It is unfortunate that, due to a combination of logistics and the inexperience of the author with the nuances of the atmospheric theory, these sections will mostly be concerned with demonstrating that these simple techniques are not adequate for remote sensing in a supersonic flow. They do, however, serve the purposes of casting the atmospheric theory in terms much more applicable to wind tunnel modeling and pointing out the theoretical work necessary to develop an adequate remote sensing technique.

B. The Application of Yura's Formalism to the Case of Crossed Beam Correlation

Since the extended Huygens-Fresnel theory and the formalism

presented by Yura has been successful in modeling the case of single beam propagation through a turbulent supersonic flow, it may be applied to the case of dual beam propagation and correlation.³³ In order to provide point measurements in the flow, a crossed beam experiment will be considered where the measured quantities will consist of the position of the beam centroid as a function of time as shown in Figure 42. The detectors D_1 and D_2 are position-sensing photodiodes having a wide frequency bandwidth (~ 500 kHz) and are thus capable of resolving the so-called "short term" location of the beam centroid. This position is defined as:

$$\vec{P}_c \equiv \int d^2\vec{p} I(\vec{p}, z) / N_p \quad (1a)$$

where:

$$N_p \equiv \int d^2\vec{p} \langle I(\vec{p}, z) \rangle \quad (1b)$$

The beam centroid correlation function may be written in the form:²⁰

$$\langle \vec{P}_c(z_1) \vec{P}_c(z_2) \rangle = N_p^{-2} \int d^2\vec{p}_1 \int d^2\vec{p}_2 (\vec{p}_1 \cdot \vec{p}_2) \langle I(\vec{p}_1, z_1) I(\vec{p}_2, z_2) \rangle \quad (2)$$

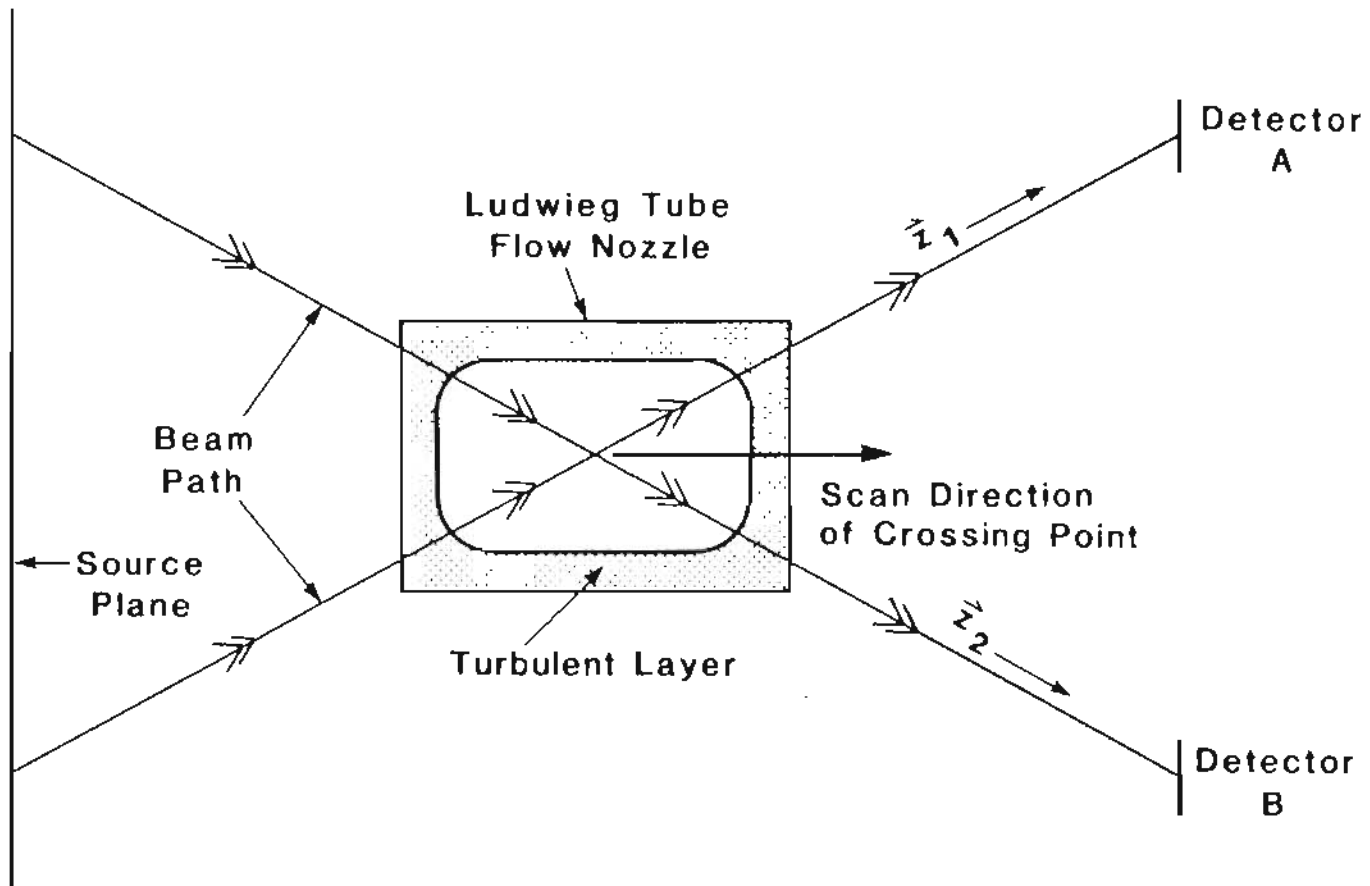


FIGURE 42. Proposed Crossed Beam Experiment

where the correlation $\langle I(p_1, z_1) I(p_2, z_2) \rangle$ is defined as the fourth order mutual coherence function (MCF) by Yura and given the designation Γ_4 .³³

The MCF may be written in terms of the optical field amplitudes:

$$\Gamma_4(\vec{p}_1, z_1; \vec{p}_2, z_2) = \langle U(\vec{p}_1, z_1) U^*(\vec{p}_1, z_1) U(\vec{p}_2, z_2) U^*(\vec{p}_2, z_2) \rangle \quad (3)$$

assuming that the beams are crossed at the waist and have identical confocal parameters. As shown in Chapter III:

$$U(\vec{p}, z) = -(ik/2\pi) \int d^2\vec{r}_1 \int d^2\vec{r}_2 \int d^2\vec{r}_3 \int d^2\vec{r}_4 U_a(\vec{r}_1) U_a^*(\vec{r}_2) U_a(\vec{r}_3) U_a^*(\vec{r}_4) \\ \cdot \langle G(\vec{p}_1, \vec{r}_1) G^*(\vec{p}_1, \vec{r}_2) G(\vec{p}_2, \vec{r}_3) G^*(\vec{p}_2, \vec{r}_4) \rangle \quad (4a)$$

where:

$$G(\vec{p}, \vec{r}) = \text{Exp}\{ik|\vec{p} - \vec{r}| + \psi(\vec{r}, \vec{p})\} / |\vec{p} - \vec{r}| \quad (4b)$$

where ψ is the phase perturbation of the spherical wave as introduced in Chapter III. The expectation value of the product of Green's functions in Eq. (4) may be written in the form:

$$\begin{aligned}
\langle GG^*GG^* \rangle &= \text{Exp}\{ik(|\vec{p}_1 - \vec{r}_1| - |\vec{p}_1 - \vec{r}_2| + |\vec{p}_2 - \vec{r}_3| - |\vec{p}_2 - \vec{r}_4|)\} \\
&\cdot (|\vec{p}_1 - \vec{r}_1| \cdot |\vec{p}_1 - \vec{r}_2| \cdot |\vec{p}_2 - \vec{r}_3| \cdot |\vec{p}_2 - \vec{r}_4|) \\
&\cdot F_4 \tag{5}
\end{aligned}$$

where:

$$F_4 \equiv \langle \text{Exp}\{\psi(\vec{r}_1, \vec{p}_1) + \psi^*(\vec{r}_2, \vec{p}_1) + \psi(\vec{r}_3, \vec{p}_2) + \psi^*(\vec{r}_4, \vec{p}_2)\} \rangle \tag{6}$$

The functions ψ may be expanded in terms of ψ_1 and ψ_2 where $\psi_1 \sim n_1$ and $\psi_2 \sim n_1^2$ (see Chapter III) and n_1 is the randomly fluctuating part of the refractive index of the working fluid.⁶ Thus the exponent in Eq. (6) may be written in the form:

$$\begin{aligned}
&\psi_1(\vec{r}_1, \vec{p}_1) + \psi_2(\vec{r}_1, \vec{p}_1) + \psi_1^*(\vec{r}_2, \vec{p}_1) + \psi_2^*(\vec{r}_2, \vec{p}_1) + \psi_1(\vec{r}_3, \vec{p}_2) + \psi_2(\vec{r}_3, \vec{p}_2) \\
&+ \psi_1^*(\vec{r}_4, \vec{p}_2) + \psi_2^*(\vec{r}_4, \vec{p}_2) \tag{7}
\end{aligned}$$

For an exponential function of the form $\text{Exp}\{f\}$, Yura has shown that:³³

$$\langle \text{Exp}\{f\} \rangle = \text{Exp}\{\langle f \rangle + \langle f^2 \rangle / 2 - \langle f \rangle^2 / 2\} \quad (8)$$

to second order. By substituting Eq. (7) into Eq. (8) and simplifying the result in the manner used in Chapter III, it may be shown that:

$$f = -2\langle |\psi_1|^2 \rangle + \langle \psi_1^{11} \psi_1^{*21} \rangle + \langle \psi_1^{11} \psi_1^{32} \rangle + \langle \psi_1^{11} \psi_1^{*42} \rangle + \langle \psi_1^{*21} \psi_1^{32} \rangle \\ + \langle \psi_1^{*21} \psi_1^{*42} \rangle + \langle \psi_1^{32} \psi_1^{*42} \rangle \quad (9)$$

to second order in n_1 , where:

$$\psi_1^{ij} \equiv \psi_1(\vec{r}_j, \vec{p}_k) \quad (10)$$

Terms of the form $\langle \psi_1^{ij} \psi_1^{kj} \rangle$ may be evaluated using the methods of Chapter III and pose no special problem as most of these terms will be eliminated by the normalization in Eqs. (1). A slightly different approach will be taken in evaluating the terms of the general form $\langle \psi_1^{jk} \psi_1^{lm} \rangle$. Yura has shown that:

$$\langle \psi_1^{jk} \psi_1^{lm} \rangle = (k^2 / 2\pi) [U_0(\vec{r}_j, \vec{p}_k) U_0(\vec{r}_l, \vec{p}_m)]^{-1} \cdot \int d^3\vec{x}_1 \int d^3\vec{x}_2 \\ \cdot [B_n(\vec{x}_1 - \vec{x}_2) U_0(\vec{r}_j, \vec{x}_1) U_0(\vec{r}_l, \vec{x}_2)] / (|\vec{x}_1 - \vec{p}_k| \cdot |\vec{x}_2 - \vec{p}_m|)$$

$$\cdot \text{Exp}\{ik\{|\vec{X}_1 - \vec{p}_k| + |\vec{X}_2 - \vec{p}_m|\}\} \quad (11)$$

where U_0 is the functional form of the optical field in the observation plane and B_n is the refractive index correlation function defined to be $\langle n_1^2 \rangle$. Tatarskii has shown that the refractive index correlation function may be related to the three-dimensional spectrum of the index fluctuations (see Chap. III) by the following (for isotropic turbulence):²⁴

$$B_n(\vec{X}_1 - \vec{X}_2) = B_n(|\vec{X}_1 - \vec{X}_2|) \equiv B_n(r) = \int d^3\vec{\kappa} \text{Exp}\{i\vec{\kappa} \cdot \vec{r}\} \phi_n(\kappa) \quad (12)$$

where κ is the spatial frequency coordinate defined as $2\pi/r$. The low frequency formulation of the modified von Karman spectrum from Chapter III will again be used to represent the statistical turbulent field in the flow nozzle.

$$\phi_n = C_n^2 / (\kappa^2 + \kappa_0^2)^{-11/6} \quad (13)$$

where C_n^2 is the structure constant and κ is defined as $2\pi/L_0$.

Substituting Eq. (13) into Eq. (12), the area integration over κ may be carried out using well known and tabulated formulae.⁶⁴

$$B_n(r) = C_0 C_n^2 (\kappa_0 r)^{1/3} \Gamma(1/6) \cdot K_{1/3}(\kappa_0 r) \quad (14a)$$

where $K_{1/3}$ is the modified Bessel function of the second kind and:⁵⁸

$$C_0 \equiv (6/5)(\pi^{1/2})(\kappa_0^{-2/3}) \quad (14b)$$

As shown in Figure 43, B_n may be closely approximated using the functional form $\text{Exp}\{-\alpha\kappa_0 r\}$ where α is a constant. This form is much more intuitive than the Bessel function and will be employed for clarity in the following discussion.

In order to evaluate Eq. (11) it will be necessary to select a reference system for the experiment. For the sake of simplicity, the geometry shown in Figure 44 will be used for this calculation. Even though this arrangement is not possible given the configuration of the test nozzle, it will serve to illustrate the fundamental limitations of this approach. The optical fields are assumed to be two spherical waves emitted from the points $(-L/2, 0, 0)$ and $(0, L/2, 0)$ and viewed at the points $(L/2, 0, 0)$ and $(0, -L/2, 0)$. The distance from the source to the observation plane is L in both axis.

Since the waves will both be observed near the respective propagation axis, the paraxial approximation (see Chap. III) may be employed and thus:

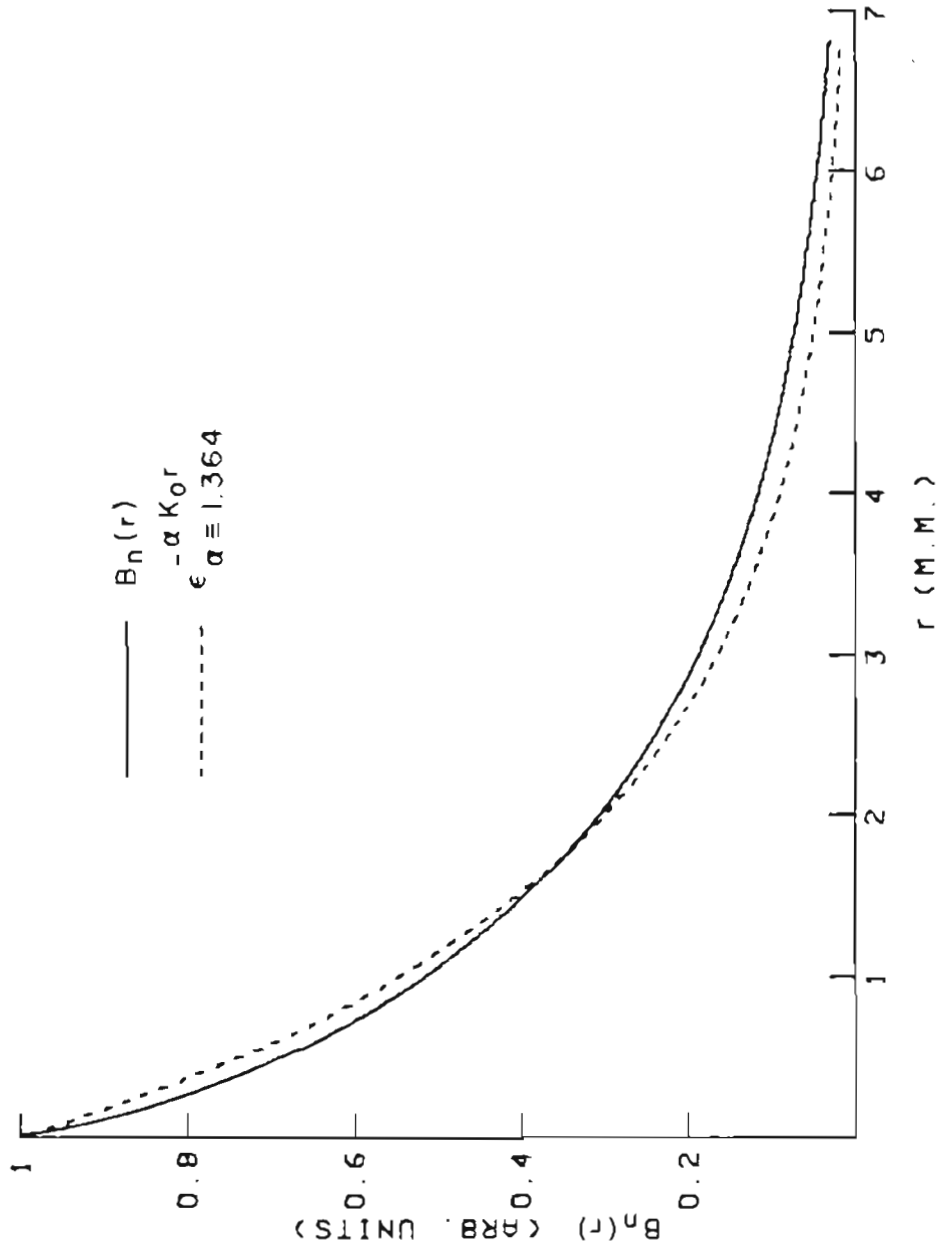


FIGURE 43. Exponential Approximation to $B_n(r)$

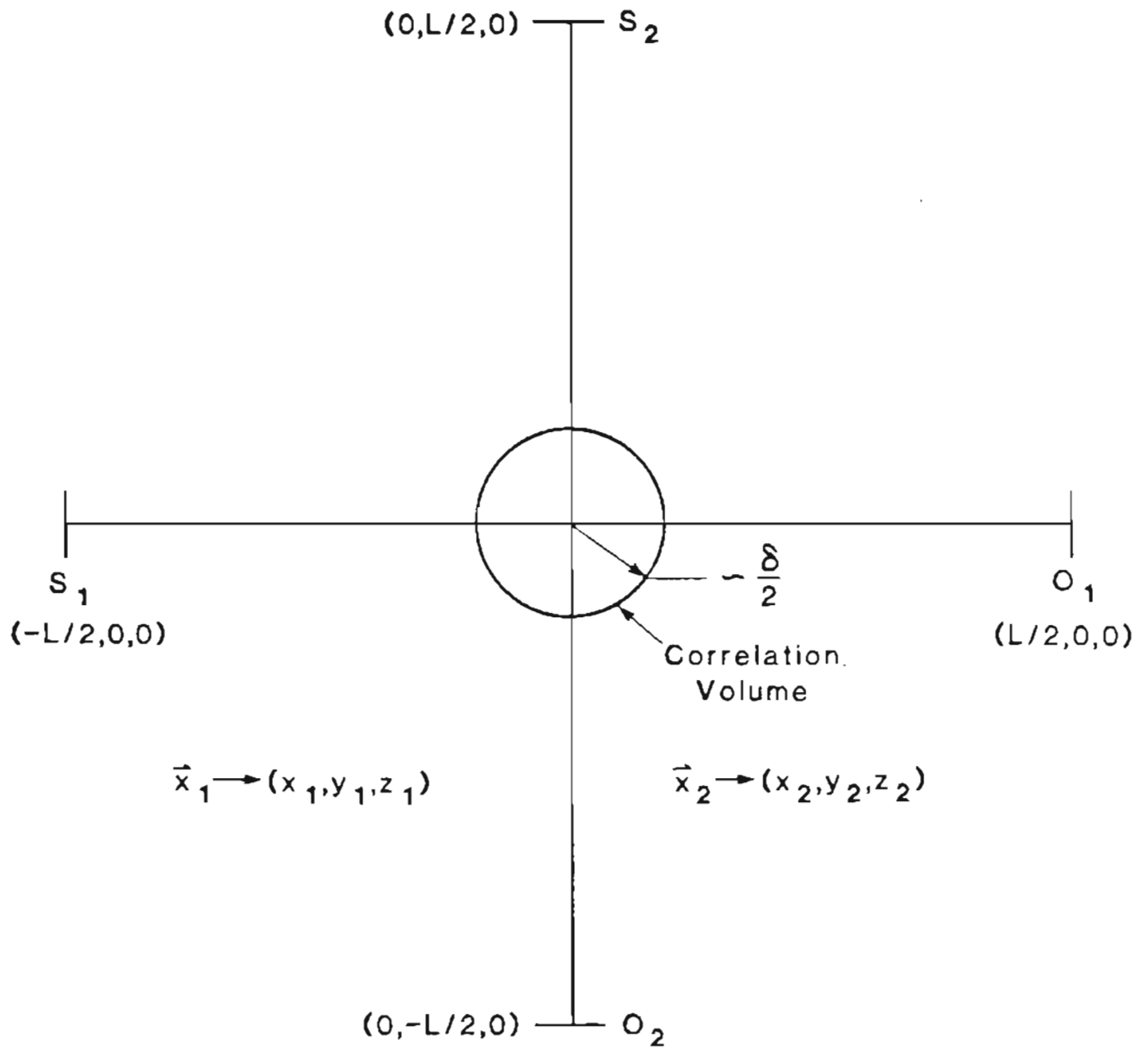


FIGURE 44. Beam Crossing Geometry

$$|\vec{r}_1 - \vec{x}_1| = (x_1 + L/2) + (y_1^2 + z_1^2)/[2(x_1 + L/2)] \quad (15)$$

If the other magnitude terms in Eq. (11) are evaluated in a similar manner, it is possible to show that calculations of the form $\langle \psi_1 \psi_1^* \rangle$ may be written in the form:

$$\begin{aligned} \langle \psi_1 \psi_1^* \rangle \propto & \int d^3\vec{x}_1 \int d^3\vec{x}_2 B_n(|\vec{x}_1 - \vec{x}_2| / [(L^2/4 - x_1^2)(L^2/4 - y_2^2)]) \\ & \cdot \text{Exp}\{(2ik/L)(y_1^2 + z_1^2 - x_2^2 - z_2^2)\} \end{aligned} \quad (16)$$

Since the only significant contribution to the result will come from points very near the origin, Eq. (16) may be simplified to the form:

$$\begin{aligned} \langle \psi_1 \psi_1^* \rangle = & (16/L^4) \int dy_1 \int dz_1 \int dx_2 \int dz_2 \text{Exp}\{(2ik/L)(y_1^2 + z_1^2 - x_2^2 - z_2^2)\} \\ & \cdot \int dy_2 \int dx_1 B_n(|\vec{x}_1 - \vec{x}_2|) \end{aligned} \quad (17)$$

It is evident from Eq. (17) that the correlation $\langle \psi_1 \psi_1^* \rangle$ will receive contributions over the nonzero range of B_n . It is also apparent

from Figure 43 that B_n will be negligibly small only for values of r greater than about half the boundary layer thickness ($\delta/2$). This will not provide a sufficiently small correlation volume to be of use in laboratory scale wind tunnels and thus this approach will not be applicable to the point-resolved remote sensing of turbulence in supersonic fields.

C. The Application of Log Amplitude Techniques to the Problem of Remote Sensing in a Wind Tunnel

An approach to point-resolved remote sensing in the atmosphere has been developed by Wang, Clifford and Ochs.³⁰ It follows the traditional formalism of atmospheric optics and requires the separation of the amplitude and phase of the optical wave after propagation through a random turbulent field.⁵⁶ It was the hope of the author that this technique could also be applied in the case of turbulence in a supersonic flow even though the amplitude/phase separation would require more complicated receiving instrumentation and analysis process than the method of the previous section.

In order to illustrate the techniques involved, consider the form of the wave equation applicable to propagation in a medium having a randomly fluctuating index of refraction.

$$[\nabla^2 + k^2(1 + n_1)^2]U(\vec{r}) = 0 \quad (18)$$

where U is the electric field of the optical radiation, $k (= 2\pi/\lambda)$ is the magnitude of the wave vector and n_1 is the randomly fluctuating part of the index of refraction.⁵⁶ It will be assumed that n_1 is small enough that $(1 + n_1)^2 \approx 1 + 2n_1$.

Using Ishimaru's notation, the first iteration solution using the Rytov method is given by:

$$U(\vec{r}) = U_0(\vec{r})\text{Exp}\{\psi_1(\vec{r})\} \quad (19a)$$

$$\psi_1(\vec{r}) = \int d^3\vec{r}' h(\vec{r}, \vec{r}')n_1(\vec{r}') \quad (19b)$$

$$h(\vec{r}, \vec{r}') = 2k^2G(\vec{r} - \vec{r}')U_0(\vec{r}')/U_0(\vec{r}) \quad (19c)$$

where G is the spherical wave Green's function defined in Eq. (5). ψ_1 , as in the previous calculations, represents the first order (in n_1) phase perturbation induced by the turbulent field and may be written in the form:

$$\psi_1 = \chi + iS \quad (20)$$

where χ is the log of the field amplitude and S is the phase fluctuation.

Wang et al. have modeled the crossed beam problem shown in Figure 45 where two spherical waves (Gaussian beams in the far field) are emitted from the points $(0, \rho_t/2, 0)$ and $(0, -\rho_t/2, 0)$ and are detected by receivers at the points $(0, y_0/2, L)$ and $(0, -y_0/2, L)$ respectively.³⁰ If the total propagation path is short (as is the case for the Ludwig tube) the detector R_a will see radiation only from T_a and the same will hold true for R_b and T_b . By modeling the turbulence as a sinusoidal phase perturbing slab of thickness ds (following the previous work done by Lee and Harp) and then integrating over ds , the authors have shown that the log amplitude correlation function for the two signals, C_{ab} , may be written in the following form:

$$C_{ab} \propto \int_0^L ds W_{ab} C_n^2(s) \quad (21a)$$

$$W_{ab} \propto \int_0^\infty dk k^{-8/3} \sin^2[k^2 s(1-s)/2kL] \cdot J_0\{k[\rho_t(1-s/L) - y_0 s/L]\} \quad (21b)$$

where k is the spatial frequency of the turbulent field, and J_0 is the zero'th order Bessel function. The Kolmogorov spectrum, given by:

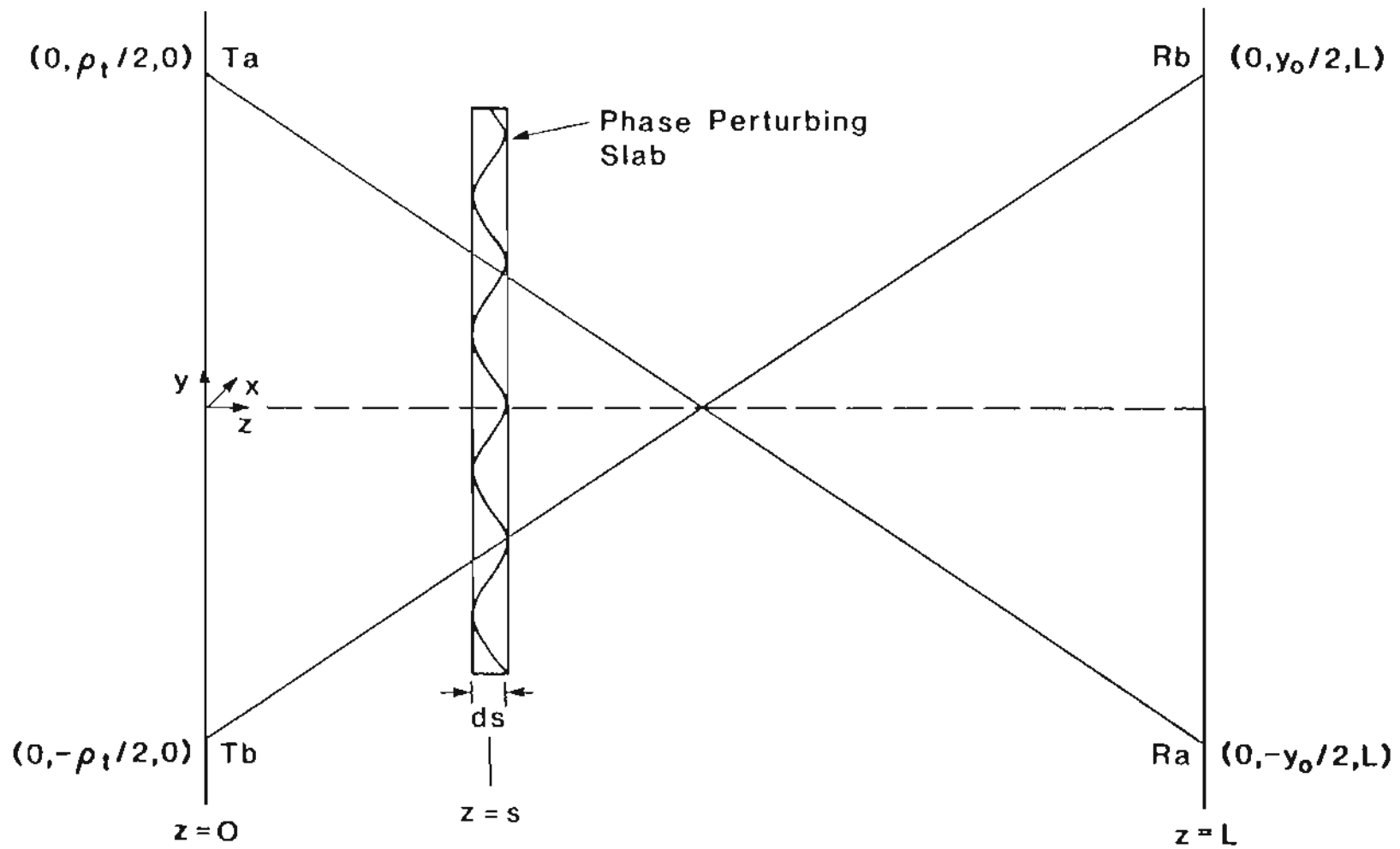


Figure 45. Beam Crossing Geometry Used by Wang et al

$$\phi_n(\kappa) = 0.033C_n^2(s)\kappa^{-11/3} \quad (22)$$

has been employed in this calculation.²⁴

While the relation for W_{ab} (the so-called "weighting function") cannot be evaluated in closed form, it represents a function peaked about the crossing point of the two beams ($s/L = 0.5$).³⁰ The width of the peak may be made almost arbitrarily small by varying the crossing angle (ρ_t and y_0) of the beams, thus providing a weighting function on the integration over the optical path s and giving very good spatial resolution.

While this formulation appears, at first glance, to provide an excellent theoretical base for a crossed beam remote sensing device, there it is severely limited in its application by the paraxial approximation used in its development.

When deriving the basic formulation of this approach, Lee and Harp employed the restriction that the beams be viewed at transverse distances that are small when compared to the propagation length L . They also showed that this condition may be expressed as the following function of the Fresnel zone ($[L\lambda]^{1/2}$):⁶²

$$y_0 \ll (4L^3\lambda)^{1/4} \quad (23)$$

Since L , in the case of the Ludweig tube flow nozzle, is only about 6

cm, this limits the separation distance of the receivers to no more than a few millimeters. In fact, the crossing angle of the successful atmospheric experiment conducted by Wang et al. was less than 10 urad.³⁰ This small crossing angle is not only impossible to achieve from an engineering viewpoint, it also results in a very broad path weighting function (W_{ab}) which is not capable of providing sufficient spatial resolution to permit point-resolved measurements in the turbulent boundary layer.

Since this method is capable of providing spatial resolution in the paraxial limit, it is natural to assume that it may be capable of providing such resolution outside this limit as well. The proof of this assumption will require a reformulation of the path weighting function (W_{ab}) and extensive computer analysis since it will not be possible to carry out any of the integration steps in closed form. This effort was beyond both the funding and the intent of this project.

D. Conclusions

It is clear from the previous analysis that a dual beam experiment based on a simple optical power measurement is not adequate for point-resolved remote sensing of the supersonic turbulent field in a laboratory scale wind tunnel. The log amplitude measurement must remain indeterminate until the ramifications of relaxing the paraxial approximation on the observation points are understood.

At this point, the best suggestion that can be made for the design

of a crossed beam experiment in the Ludwig tube would be to use the basic geometry of Figure 42, but employ a schlieren-based receiver system capable of providing log amplitude information.

CHAPTER VIII

THE RESULTS OF THE CROSSED BEAM EXPERIMENT

A. A Detailed Description of the Experiment

As discussed in Chapter VII, the logistics and timing of the laboratory work done at NASA Ames was such that it was necessary to carry out a crossed beam experiment before an adequate theoretical model could be developed. The basic decision was either make a "best guess" attempt at a dual beam experiment or give up the idea altogether. As a result of this, an experiment was devised to measure and correlate the deflections of two He-Ne laser beams crossed in the turbulent boundary layer at a point which could be easily scanned through the layer. It has been shown in Chapter VII that such an experiment was certain to fail from the start unless the longitudinal density correlation length was small compared to the boundary layer size, but this fact was not known at the time of the actual experimental work.

The basic concept of the experiment has been presented in Chapter VII (see, in particular, Figure 42). The general experimental layout is shown in Figure 46.

The beam from a Spectra Physics Model 133 He-Ne laser was expanded, using the same basic beam expander design employed in the single beam

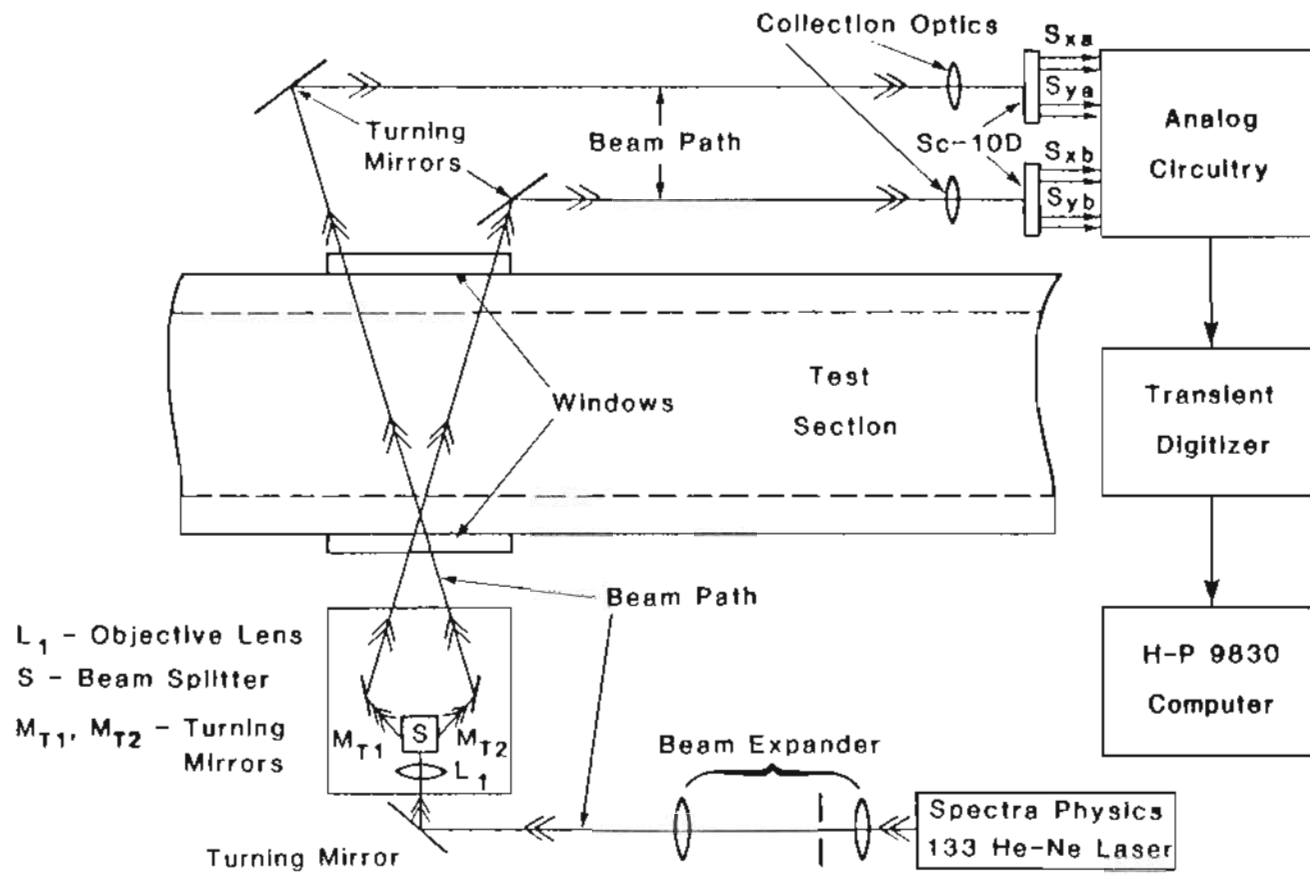


FIGURE 46. The Layout of the Crossed Beam Experiment

work (see Chapter VI). The collimating lens of the expander had a focal length of 310 mm and thus the output beam had a radius of 2.3 mm. This beam was focused by a 510 mm focal length objective lens and split into two identical beams using a 50/50 polarizing beam splitter as shown in Figure 46. This arrangement produced beams with a focused waist size of 46 μm and a Rayleigh range of about 1 cm.

The two beams were then directed using adjustable turning mirrors to a crossing point forming an angle of approximately 37° . This angle was fixed by the diameter (2 in) of the windows in the flow nozzle and the width of the test section (6.35 cm).

Two United Technology SC-10D position sensing photodiodes were chosen as the detectors. These detectors make use of the dependence of semiconductor photoelectron transport on the position at which the photoelectron is created to produce output signals which are a function of the position of the beam centroid. When operated in photoconductive mode, as was the case for this experiment, the devices have excellent high frequency response with rise times on the order of a few hundred nanoseconds easily obtainable. Each detector has five output leads corresponding to +x, -x, +y, and -y signals along with a case ground. These signals may be summed using the appropriate analog circuitry (see Figure 47) to produce signals which are of the following form:

$$S_x \propto I_x \quad (1a)$$

$$S_y \propto I_y \quad (1b)$$

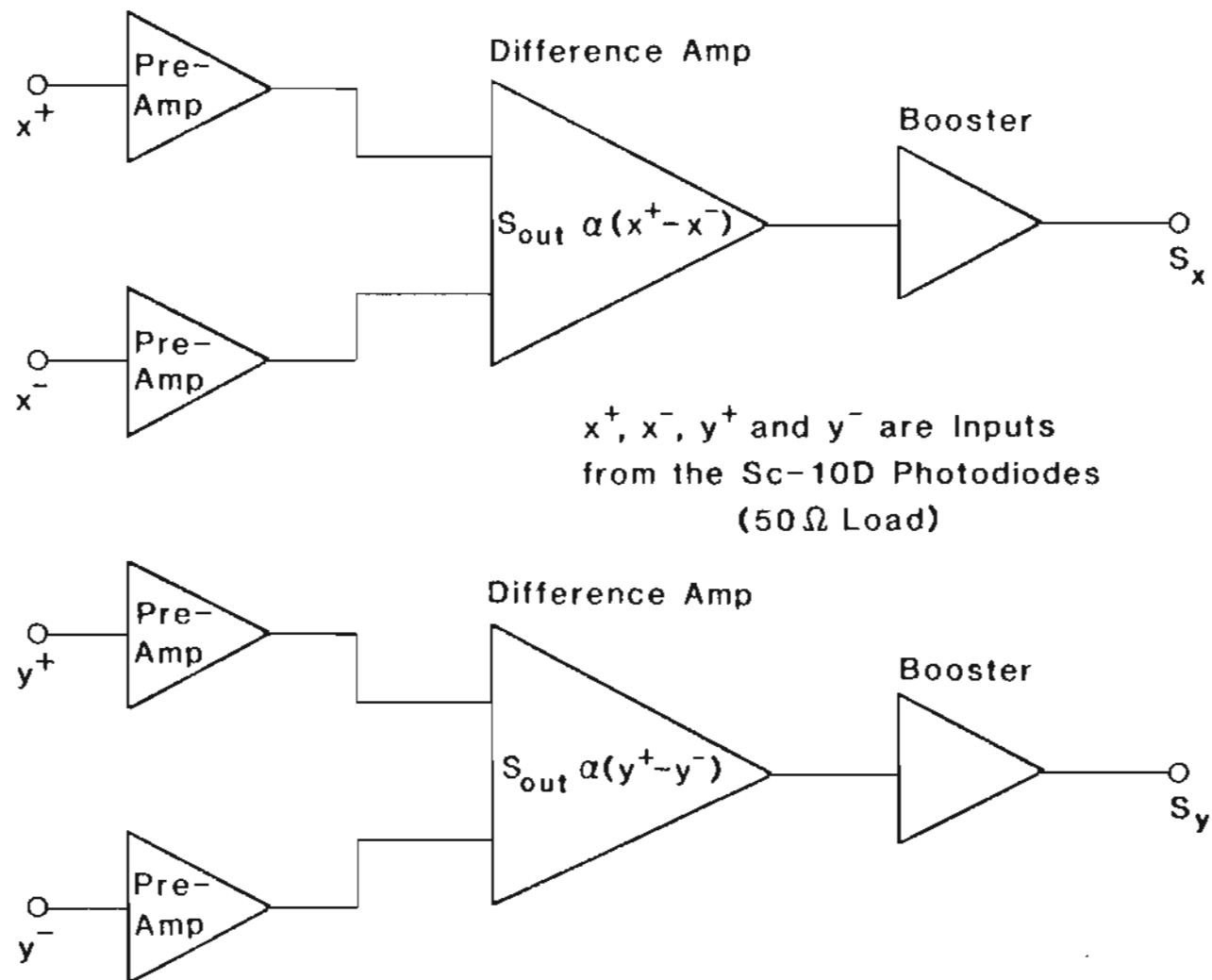


FIGURE 47. Detector Analysis Logic

where x and y are the Cartesian coordinates of the beam centroid and I is the output intensity of the laser beam. In order to produce output signals free from laser power effects, it is, strictly speaking, necessary to normalize out the intensity dependence. This operation would require two more reference signals carrying only intensity information and an analog divide section in the analysis circuitry. Not only would this add another level of complication to the instrumentation, it would also severely limit the frequency response of the system due to the fact that analog dividers intrinsically have a high frequency roll-off on the order of 30-50 kHz. Since the He-Ne laser is capable of providing an output power level which is highly stable over long time periods, I may be treated as a constant in this experiment and the analog division is not necessary.

The original design of the analysis circuitry provided a signal gain of about 10^6 which would have been adequate to measure the position fluctuations of each beam with a signal to noise in excess of 500:1. For reasons which are still unclear, the detection system in actual operation could only provide gain on the order of about 10^4 - 10^5 which limited the overall signal to noise ratio of the measurement to about 10-25:1. Even to achieve this reduced SNR, it was necessary to extend the optical lever arm of the measurement to over 10 m and add the collection and steering lenses shown in Figure 46.

The entire beam splitter/objective lens assembly was mounted on a jack-screw-driven translation stage so that the beam crossing point

could be accurately scanned through the boundary layer. This assembly was manufactured in a manner which allowed the crossing plane of the beams to be rotated through 90° so that the boundary could be scanned in a horizontal fashion, as shown in Figure 46, or in a vertical manner.

The x and y signals from the two detectors were digitized and stored in a Physical Data 515a transient digitizer and then transferred to an HP 9830 computer for storage and analysis. This was accomplished in a manner similar to the data collection in the single beam experiment (see Chapters V and VI).

The two beams were crossed at their waists by means of an aperture placed at the waist location having a radius of approximately half that of the beam spot. By maximizing the power transmitted by this aperture, the two beams could be overlapped to within 5% of the waist radius.

The entire apparatus was tested for vibrational noise levels in a manner similar to that employed in the single beam case (see Chap. VI). The overall signal-to-noise ratio of the detector system was measured by causing a known fixed deflection in the beams and measuring this deflection while the wind tunnel was in operation but with the beams being steered clear of the test section. The frequency response of the detector circuitry and data collection electronics was determined by driving the system with a simulated signal produced by an electronic function generator. The high frequency roll-off of the system was measured to be in excess of 500 kHz.

Data was collected for eight locations of the beam crossing point in the test nozzle over the range $0 \leq y/\delta \leq 1.05$. Both vertical and

horizontal scans were taken.

B. The Experimental Results

While a large volume of data was collected and analyzed, the results are adequately represented by the graph shown in Figure 48. This is a plot of the un-normalized correlation coefficient (in arbitrary units) versus y/δ calculated from the formula:

$$C_x = \left(\sum_1 Sx_i \right) / N \quad (2)$$

where Sx_i is the i -th data point stored in the transient digitizer memory and N is the total number of memory locations (4096 for this experiment). The curve shows the results of two identical scans plotted on the same axis.

The correlation results for the y axis showed no repeatability whatsoever from point to point or run to run. The reason for this is not known but it was probably due to an electrical component failure in the analog analysis circuitry which was not apparent from viewing the raw data.

While all the x scans showed the same coarse features as a function of y/δ , these results cannot be interpreted as having any logical relation to the turbulent field in the flow nozzle, in particular the strong negative value occurring near the $y/\delta = 0.5$ location. If this was an indication of a real artifact of the flow, it was probably

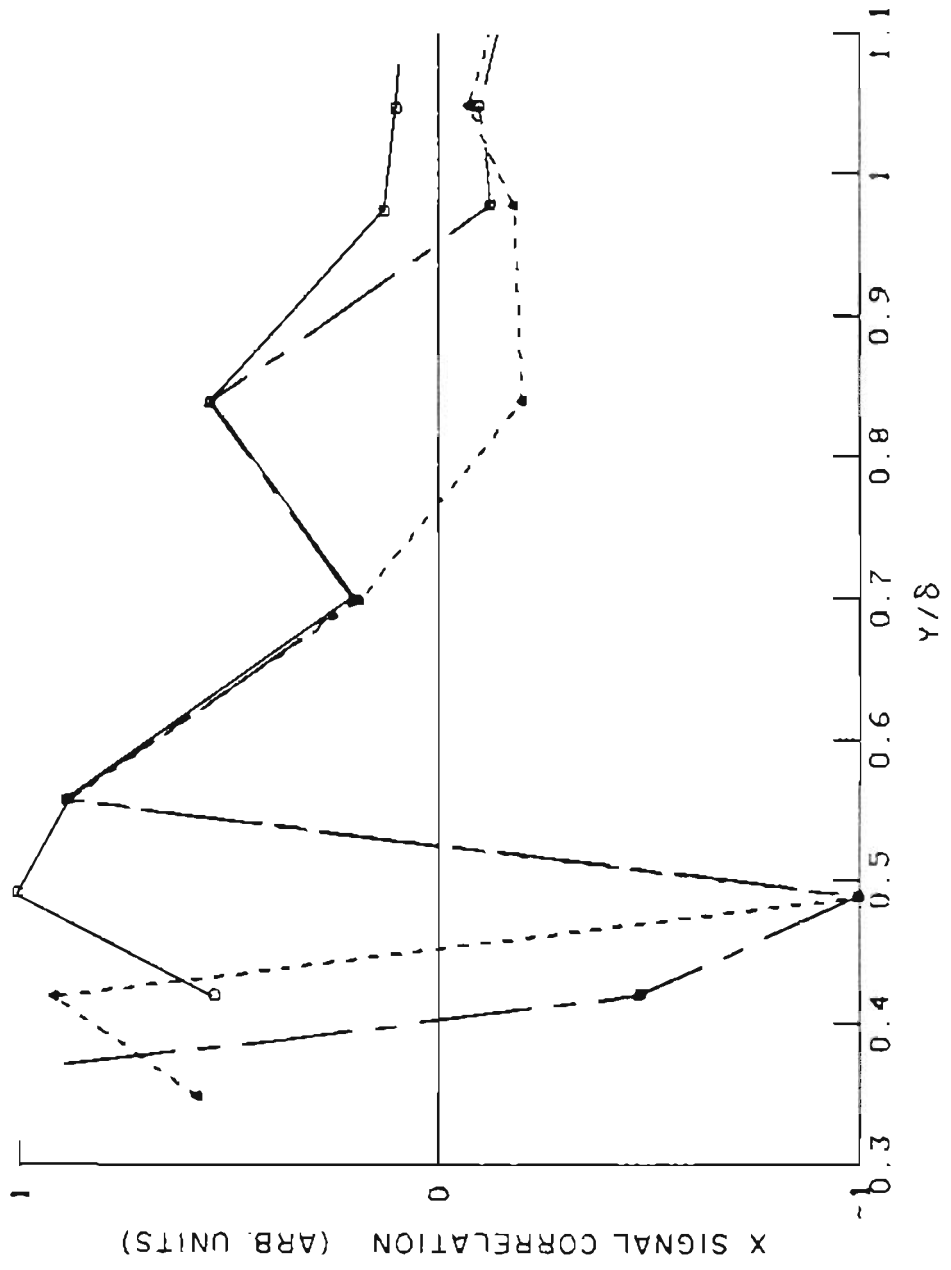


FIGURE 48. X Axis Cross Correlation Coefficient vs. y/δ

due to a weak shock wave being produced by the window/wall interface and extending downstream.

The solid line plot in Fig. 48 shows the absolute value of one of the correlation coefficients. The shape of this curve is similar in form to that of $C_n^2(z)$ and it is tempting to seek a justification for using the absolute value. Since it was not possible to find a theoretical approach capable of modeling the crossed beam correlation, several arguments may be advanced for doing just that.

It should be noted, however, that the experiment presented here was specifically designed so that the response of the two beams to turbulence localized about the crossing point would be positive. There should be no need to employ the absolute value of the correlation coefficient if the experiment had indeed provided spatially resolved measurements.

These results are very disappointing and are in stark contrast to the rather happy outcome of the single beam experiments. The failure of the data to provide any meaningful information about the flow still leaves the modest question of the scale of the longitudinal density correlation unanswered.

The overwhelming reason for the failure of this undertaking is due to the severe time constraints imposed on the work by the funding and logistics. There simply was not enough time to complete the experiment in a proper manner and the results are reflective of this.

From an engineering point of view, the major problems in this work were probably introduced by the analysis circuitry. This system never

did perform anywhere near its design parameters over the course of the entire experiment and was simply not adequate for the job at hand. The design of this system represented the first attempt at building a suitable measurement system, and the necessary rush to complete the experiment left no time for the development of a second generation system.

CHAPTER IX

CONCLUSIONS AND SUGGESTIONS FOR FURTHER WORK

A. Conclusions

The results of the single beam work described in this document show conclusively that the extended Huygens-Fresnel theory and the formalism developed by H. T. Yura are quite capable of quantitatively modeling the effects of turbulence in a three-dimensional supersonic boundary layer on propagating optical radiation. T. Grandke has recently verified these results for the less complicated case of a two-dimensional turbulent field with equally encouraging results.¹⁵ The theory presented here is of a more general nature and thus capable of modeling a much wider variety of situations than a strictly two-dimensional approach.

The basic elements of the single beam measurements described here have been applied, by the author, to the design of a laser based remote sensing device for the measurement of turbulent burst phenomena in a supersonic wind tunnel. This instrument is not only capable of detecting the presence and spatial extent of the burst, but can also estimate the statistical moments of the density fluctuations in the perturbed flow region with a high signal-to-noise ratio.

There are two basic limitations on the applicability of the models developed in Chapter III. The modified von Karman spectrum (particularly the low frequency formulation presented in this work) is not capable of describing the refractive index correlations in all flows of interest and it is not possible, at this point, to make an a priori determination of the turbulence characteristics for an arbitrary flow. While this is a significant problem for experimentalists, it is not insurmountable in even the most general case since it is possible to make at least a rough determination of the refractive index correlation spectrum using intrusive techniques similar to those described in Chapter IV. The intrusive devices, and their perturbing influences, may then be removed from the flow and the optical technique employed to remotely sense the flow unintrusively with much higher signal-to-noise and frequency response than can be achieved with physical probes. If the von Karman spectrum is known to apply in a given flow, and a growing volume of evidence indicates that this may generally be the case, then there is no need to use any intrusive sensing for statistical density measurements.

The approximations employed in Chapter III will not be generally applicable to a wide variety of real-world flow situations of interest. This means that it will not be possible to reduce the integral formulations inherent in the extended Huygens-Fresnel theory to closed form results. Since the analysis of the optical data cannot be carried out in real time in any case, the use of high speed computer integration algorithms are the solution to this problem.

Since the crossed beam work described here is a classic example of how not to carry out an experiment, very little can be concluded generally about the use of the extended Huygens-Fresnel theory in this application. Further theoretical and experimental work is necessary before the underlying questions can begin to be answered.

B. Suggestions for Further Work

As mentioned in the previous section, the formalism presented in Chapter III should be written in terms of computer analysis involving efficient integration algorithms. This will eliminate the need for several approximations introduced in the models developed here and provide a theory capable of modeling much more general flow situations than the one encountered in the NASA Ludwig tube.

As shown in Chapter V, the fundamental nature of laser beam/turbulent eddy interaction is dependent on the size of the beam relative to the eddy scale (see Figure 19). By using very small beams (waist spot sizes on the order of 5-10 μm) and relatively long wavelength optical radiation such as that produced by an infrared He-Ne laser (1.15 μm), it is possible to generate highly divergent beams which have an appreciable increase in spot size of the dimensions of even a small turbulent boundary layer such as the one in the Ludwig tube flow nozzle (~ 1.5 cm). This means that the beam response to a given turbulent scale will be a function of path length and thus this may be a method for carrying out single beam measurements with at least limited

spatial resolution. This scheme should be modeled using the extended Huygens-Fresnel theory so that the ramifications can be understood. It may also be possible to apply the general idea of highly divergent beams to the log amplitude filter functions as presented by Ishimaru with similar results.⁵⁶ This too should be investigated.

In the case of the crossed beam work, the theory developed by Lee and Harp should be examined with the goal of removing the paraxial restriction in the final result.⁶⁰ This will also require extensive computer work as the integrals critical to this formalism probably cannot be evaluated in closed form.

Once a sound theoretical foundation has been established, it will be possible to make an informed attempt at designing a suitable crossed beam experiment to test the resultant model. This experiment will probably be very similar to the layout presented in Chapter VIII but with a schlieren-based detection system providing log amplitude information as opposed to total power measurements.

REFERENCES

1. D. R. Chapman, "Computational Aerodynamics Development and Outlook," AIAA Jour. 24, 1293-1313 (1979).
2. B. Koch, "Laser Beam Probing for Aerodynamic Flow Fields," AGARD Lecture Series No. 49 (1971).
3. V. A. Sandborn, "A Review of Turbulence Measurements in Compressible Flow," NASA Report TM X-62, 337 (1974).
4. D. A. Johnson and W. C. Rose, "Laser Velocimeter and Hot-Wire Anemometer Comparison in a Supersonic Boundary Layer," AIAA Jour. 13, 512-515 (1975).
5. H. L. Seegmiller, "Application of Laser Velocimetry to an Unsteady Transonic Flow," 8th International Conference on Instrumentation in Aerospace Simulation Facilities (1979).
6. D. R. Crossley and G. P. Smith, "Vibrational Energy Transfer in Laser Excited $A^2\Sigma^+OH$ as a Flame Thermometer," Appl. Opt. 19, 517-520 (1980).
7. R. L. McKenzie and K. P. Gross, "Two-Photon Excitation of Nitric Oxide Fluorescence as a Temperature Indicator in Unsteady Gasdynamic Processes," Appl. Opt. 20, 2153-2165 (1981).
8. K. P. Gross, Private Communication, June (1985).
9. R. F. Begley, A. B. Harvey, and R. L. Byer, "Coherent Anti-Stokes Raman Spectroscopy," Appl. Phys. Lett. 25, 387-390 (1974).
10. R. Goulard, "Optical Measurements of Thermodynamic Properties in

- Flow Fields, a Review," AGARD Proceedings 193, Paper 13, AGARD-CP-193, (1976).
11. E. Hecht and A. Zajac, Optics, Addison-Wesley, Reading (1979)
 12. M. R. Davis, "Measurements in a Subsonic Turbulent Jet Using a Quantitative Schlieren Technique," J. Fluid. Mech. 46, 631-656 (1971).
 13. G. T. Kalghatgi and J. B. Moss, "Quantitative Schlieren Measurements in a Confined Turbulent Premixed Flame," Proceedings, 2nd International Symposium on Turbulent Shear Flows, London, (1979).
 14. L. Hesselink and B. White, "Digital Image Processing of Flow Visualization Photographs," Submitted to Appl. Opt., (1984).
 15. T. Granke, "Theory and Application of the Laser Shadow Technique." Exp. in Fluid. 3, 77-85 (1985).
 16. G. T. Kalghatgi and P. T. Roberts, "Measurements of Fluctuating Density and Temperature in an Axisymmetric Flame," AASU Report 342 (1979).
 17. G. T. Kalghatgi, J. M. Cousins and K. N. C. Bray, "Crossed Beam Correlation Measurements and Model Predictions in Rocket Exhaust Plumes," Comb. and Flame. 43, 51-67 (1981).
 18. J. E. Craig, J. D. Trolinger and W. C. Rose, "Propagation Diagnostic Technique for Turbulent Transonic Flow," AIAA-84-0104, AIAA 22nd Aerospace Sciences Meeting, (1984).
 19. R. S. Lawrence and J. W. Strohbehm, "A Survey of Clear-Air Propagation Effects Relevant to Optical Communications," Proc.

- IEEE. 58, 1523-1545 (1970).
20. R. L. Fante, "Electromagnetic Beam Propagation in Turbulent Media," Proc. IEEE. 63, 1669-1692 (1975).
 21. G. R. Ochs, S. F. Clifford and Ting-i-Wang, "Laser Wind Sensing: The Effects of Saturation of Scintillation," Appl. Opt. 15, 403-408 (1976).
 22. J. F. Holmes, J. R. Kerr M. E. Fossey, R. L. Jacob and M. H. Lee, "Experimental Pulsed Laser, Remote Crosswind Measurement System -- Feasibility Study and Design," U. S. Army Electronic Command, White Sands Missile Range ECOM 75-1 (1975).
 23. M. H. Lee, J. F. Holmes and R. J. Kerr, "Statistics of Speckle Propagation Through the Turbulent Atmosphere," J. Opt. Soc. Am. 66, 1164-1171 (1976).
 24. V. I. Tatarskii, Wave Propagation in a Turbulent Medium, McGraw-Hill, New York (1961).
 25. V. I. Tatarskii, The Effects of the Turbulent Atmosphere on Wave Propagation, National Science Foundation, Washington, D.C. (1971).
 26. R. F. Lutomirski and H. T. Yura, "Propagation of a Finite Optical Beam in an Inhomogeneous Medium," Appl. Opt. 10, 1652-1658 (1971).
 27. A. Ishimaru, "Fluctuations of a Focused Beam Wave for Atmospheric Turbulence Probing," Proc. IEEE 57, 407-413 (1969).
 28. A. Ishimaru, "Fluctuations of a Beam Wave Propagating Through a Locally Homogeneous Medium," Radio Science 4, 295-305 (1969).
 29. S. F. Clifford, C. R. Ochs and Ting-i-Wang, NOAA ERL 312-WPL 37

- (1971).
30. Ting-i-Wang, S. F. Clifford and G. R. Ochs, "Wind and Refractive Turbulence Sensing Using Crossed Laser Beams," *Appl. Opt.* 13, 2602-2608 (1974).
 31. J. A. Dowling and P. M. Livingston, "Behavior of Focused Beams in Atmospheric Turbulence: Measurements and Comments on the Theory," *J. Opt. Soc. Am.* 63, 846-858 (1973).
 32. J. W. Goodman, Introduction to Fourier Optics, McGraw-Hill, New York (1968), p. 45.
 33. H. T. Yura, "Mutual Coherence Function of a Finite Cross Section Optical Beam Propagating in a Turbulent Medium," *Appl. Opt.* 11, 1399-1406 (1972).
 34. I. S. Gradshteyn and I. M. Ryzhik, Table of Integrals, Series and Products, Academic Press, New York (1980), Formula 6.631 #6 p. 717.
 35. R. A. Elliott, "CARS in a Turbulent Medium," private communication (1981).
 36. R. L. Fante, "Multiple-Frequency Mutual Coherence Functions for Beams in a Random Medium," *IEEE Trans. Ant. and Prop.* AP-26, 621-623 (1978).
 37. J. C. Leader, "Atmospheric Propagation of Partially Coherent Radiation," *J. Opt. Soc. Am.* 68, 175-185 (1978).
 38. S. M. Wandzura, "Meaning of Quadratic Structure Functions," *J. Opt. Soc. Am.* 70, 745-747 (1980).
 39. See reference 34, formula 3.382 #4, p. 318.

40. A. Yariv, Introduction to Optical Electronics, Academic Press, New York (1980) p. 38.
41. A. L. Kistler, "Fluctuation Measurements in a Supersonic Turbulent Boundary Layer," *Physics of Fluids* 2, 290-296 (1959).
42. F. K. Owen and C. C. Horstman, "On the Structure of Hypersonic Turbulent Boundary Layers," *J. Fluid Mech.* 53, 611-636 (1972).
43. E. L. Doughman, "Development of a Hot-Wire Anemometer for Hypersonic Turbulent Flows," *Rev. of Sci. Inst.* 43, 1200-1202 (1972).
44. W. C. Rose, "Turbulence Measurements in a Compressible Boundary Layer," *AIAA J.* 12, 1060-1064 (1974).
45. S. K. Robinson, H. K. Seegmiller and M. I. Kussoy, "Hot-Wire and Laser Doppler Measurements in a Supersonic Boundary Layer," *AIAA 16th Fluid and Plasma Dynamics Conference* (1983).
46. J. D. Trolinger, Laser Instrumentation for Aerodynamics, AGARDograph 186, (1974).
47. A. E. Perry, Hot-wire Anemometry, Clarendon Press, Oxford (1982).
48. D. Monson, Data Reduction for Pitot Tube Measurements, private communication with the author (1983).
49. Ames Research Staff, NACA Report 1135, Equations Tables and Charts for Compressible Flow, Ames Aeronautical Laboratory, (1948).
50. D. A. Johnson and W. C. Rose, "Turbulence Measurements in a Transonic Boundary Layer and Free-Shear Flow Using Laser Velocimetry and Hot-Wire Anemometry Techniques," *AIAA 9th Fluid and Plasma Conference* (1976).

51. M. V. Morkorvin, "Fluctuations and Hot-Wire Anemometry in Compressible Fluids," AGARD AG-24, (1956).
52. M. V. Morkovin and R. E. Phinney, "Extended Applications of Hot-Wire anemometry to High Speed Turbulent Boundary Layers," ASTIA AD-158-279, (1958).
53. L. S. G. Kovasnay, "The Hot-Wire Anemometer in Supersonic Flow," J. Aero. Sci. 17, 565-572 (1950).
54. C. C. Horstman and W. C. Rose, "Hot-Wire Anemometry in Transonic Flow," AIAA J. 15, 395-399 (1977).
55. D. Monson and K. P. Gross, private communication (1983).
56. J. C. Owens, "Optical Refractive Index of Air: Dependence on Pressure, Temperature and Composition," Appl. Opt. 6, 51-59 (1967).
57. G. T. Kalghatgi, "The Crossed Beam Correlation Method," AASU Report No. 340, (1979).
58. A. Ishimaru, Wave Propagation and Scattering in Random Media, Vol. 2, Academic Press, New York (1978).
59. See reference 34, Formula 6.565 #4, p. 686.
60. M. Abramowitz and I. Stegun, Handbook of Mathematical Functions, National Bureau of Standards, AMS 55, Washington D. C. (1972).
61. H. Weichel and L. S. Pedrotti, "Laser Design Equations," Elect. Opt. Sys. Des., 124-137 (1976).
62. R. W. Lee and J. C. Harp, "Weak Scattering in Random Media, with Applications to Remote Probing," Proc. IEEE. 57, 375-406 (1969).
63. M. J. Fisher and F. R. Krause, "The Crossed-Beam Correlation

51. M. V. Morkorvin, "Fluctuations and Hot-Wire Anemometry in Compressible Fluids," AGARD AG-24, (1956).
52. M. V. Morkovin and R. E. Phinney, "Extended Applications of Hot-Wire anemometry to High Speed Turbulent Boundary Layers," ASTIA AD-158-279, (1958).
53. L. S. G. Kovasnay, "The Hot-Wire Anemometer in Supersonic Flow," J. Aero. Sci. 17, 565-572 (1950).
54. C. C. Horstman and W. C. Rose, "Hot-Wire Anemometry in Transonic Flow," AIAA J. 15, 395-399 (1977).
55. D. Monson and K. P. Gross, private communication (1983).
56. J. C. Owens, "Optical Refractive Index of Air: Dependence on Pressure, Temperature and Composition," Appl. Opt. 6, 51-59 (1967).
57. G. T. Kalghatgi, "The Crossed Beam Correlation Method," AASU Report No. 340, (1979).
58. A. Ishimaru, Wave Propagation and Scattering in Random Media, Vol. 2, Academic Press, New York (1978).
59. See reference 34, Formula 6.565 #4, p. 686.
60. M. Abramowitz and I. Stegun, Handbook of Mathematical Functions, National Bureau of Standards, AMS 55, Washington D. C. (1972).
61. H. Weichel and L. S. Pedrotti, "Laser Design Equations," Elect. Opt. Sys. Des., 124-137 (1976).
62. R. W. Lee and J. C. Harp, "Weak Scattering in Random Media, with Applications to Remote Probing," Proc. IEEE. 57, 375-406 (1969).
63. M. J. Fisher and F. R. Krause, "The Crossed-Beam Correlation

Technique," J. Fluid. Mech. 28, 705-717 (1967).

64. See reference 34, Formula 3.771, #5, p 427.

VITAE

Donald R. Emmons Jr. was born in Terre Haute, Indiana, on May 19, 1950. He received the B. S. degree in physics from Indiana State University in September 1972 and the M. A. degree in September 1975. Prior to pursuing his Doctorate degree, he spent five years in Physics education on the college and university level.

Mr. Emmons began his studies at the Oregon Graduate Center in September 1979. The research work described in this dissertation was funded by the National Aeronautics and Space Administration and performed at NASA Ames Research Center, Moffett Field, CA.

TECHNICAL PUBLICATIONS AND PAPERS

R. Grismore, A. Berry, A. Taboas, D. Emmons, "Multidimensional Gamma-Ray Spectrometer with a Grid Scintillation Counter Anticoincidence Ring," Rev. of Sci. Instrum., 46, 243 (1975).

D. Emmons, R. Elliott and R. McKenzie, "Laser Beam Propagation in a High Speed Bounded Flow," Annual Meeting of the OSA, Tucson, AZ, (1982).

D. Emmons, R. Elliott, R. McKenzie, "The Effect of Turbulence in a Supersonic Flow on a Gaussian Beam," Annual Meeting of the OSA, San Diego, CA, (1985).